TERAHERTZ IMAGING APPLICATIONS AND CHARACTERIZATION OF ITO THIN FILMS GROWN BY MAGNETRON SPUTTERING

A Thesis Submitted to
the Graduate School
İzmir Institute of Technology
in Partial Fulfillment of the Requirements for the Degree of

DOCTOR OF PHILOSOPHY

in Materials Science and Engineering

by
Hasan KÖSEOĞLU

December 2020
İZMİR

To my Family…

ACKNOWLEDGEMENTS

First of all, I would like to express my gratitude to Prof. Dr. Lütfi Özyüzer for giving me the possibility of carrying out this work under his supervision. I appreciate him, for his instructive guidance, inspiring suggestions, encouragement and understanding throughout the preparation of this thesis. I also would like to acknowledge Prof. Dr. Gülnur Aygün Özyüzer for her contribution to this thesis.

I wish to extend my thanks to İzmir Institute of Technology for providing Research Assistantship throughout my doctorate study and Applied and Research Center for Quantum Technologies (KUANTAM) of IZTECH for their facilities. This research is partially supported by SANTEZ project with number 1386.STZ.2012-1 in collaboration with ASELSAN REHİS group, TUBITAK (Scientific and Technical Research Council of Turkey) project number 114F091 and 2 IZTECH- BAP Projects. I'm also grateful for the Specialist position in İSTE from 2019 to present.

I am also very thankful to my colleagues from İzmir Institute of Technology and my group members, for their helps and creating a nice environment while studying together.

I am thankful to my family for their unconditional love, unending support and understanding during my whole life and providing me with more than I can ever repay them for. I would like to express my deepest thanks to my wife, Fulya Köseoğlu, for his love, support and encouragement over the past seventeen years, and for his unwavering belief in me even when I doubted myself. Last, but not least, I would like to thank to my little sunshine, Defne Köseoğlu, who make me happy with a kiss or smile even when I feel so desperate.

ABSTRACT

TERAHERTZ IMAGING APPLICATIONS AND CHARACTERIZATION OF ITO THIN FILMS GROWN BY MAGNETRON SPUTTERING

THz radiation (0.1-10 THz) has unique properties not found in other parts of the electromagnetic spectrum. THz technological applications need high-performance THz imaging and spectroscopy system components such as THz filters, modulators, reflectors. Transparent conducting oxides (TCOs) meet these needs in the THz field. Indium tin oxide (ITO) thin film is one of the most used materials among the TCOs. However, the research on the THz properties of ITO film is currently at an early stage.

In this thesis, ITO thin films were deposited on borosilicate (BS), fused silica (FS) and PET substrates using large area magnetron sputtering system. Optical, structural and electrical properties of the ITO films on different substrates were analyzed. Moreover, the effect of electro-annealing in vacuum and air on the properties of ITO films grown on BS and FS substrates were investigated. Furthermore, CW THz imaging system were designed to take THz images of some objects and to analyze THz properties of ITO films grown on FS and PET substrates. Our findings indicate that electrical, structural and optical properties of ITO films can be improved by electro-annealing in air and vacuum. We addressed that electro-annealing in vacuum is more appropriate technique for the applications in industry. We also addressed the importance of oxygen partial pressure and ITO film thickness to adopt them as a transparent electrode in flexible devices. Moreover, our analysis about the THz properties of ITO films on FS and PET substrates showed that fabricated ITO films have potential application in THz field such as THz filters, modulators and reflectors.

ÖZET

TERAHERTZ GÖRÜNTÜLEME UYGULAMALARI VE MIKNATISSAL SAÇTIRMA İLE BÜYÜTÜLEN ITO İNCE FİLMLERİN KARAKTERİZASYONU

THz radyasyonu (0.1-10 THz), elektromanyetik spektrumun diğer kısımlarında bulunmayan benzersiz özelliklere sahiptir. THz teknolojik uygulamaları, THz filtreleri, modülatörler, reflektörler gibi yüksek performanslı THz görüntüleme ve spektroskopi sistemi bileşenlerine ihtiyaç duyar. Şeffaf iletken oksitler (TCO'lar) THz alanında bu ihtiyaçları karşılar. İndiyum kalay oksit (ITO) ince filmi TCO'lar arasında en çok kullanılan malzemelerden biridir. Ancak, ITO filminin THz özellikleri üzerine yapılan araştırmalar şu anda erken bir aşamadadır.

Bu tezde, ITO ince filmler, geniş alanlı mıknatıssal saçtırma sistemi kullanılarak borosilikat (BS), kaynaşmış silikat (FS) ve PET alttaşları üzerine kaplanmıştır. Farklı alttaş üzerindeki ITO filmlerinin optik, yapısal ve elektriksel özellikleri analiz edildi. Ayrıca, vakum ve havadaki elektriksel-tavlamanın BS ve FS alttaşları üzerinde büyütülen ITO filmlerinin özellikleri üzerindeki etkisi araştırılmıştır. Ayrıca, CW THz görüntüleme sistemi, bazı nesnelerin THz görüntülerini almak, FS ve PET alttaşları üzerinde büyüyen ITO filmlerin THz özelliklerini analiz etmek için tasarlanmıştır. Bulgularımız, ITO filmlerinin elektriksel, yapısal ve optik özelliklerinin havada ve vakumda elektriksel-tavlama ile iyileştirilebileceğini göstermektedir. Vakumda elektriksel-tavlamanın endüstrideki uygulamalar için daha uygun bir teknik olduğunu gözlemledik. Esnek cihazlarda şeffaf bir elektrot olarak kullanılabilmesi için oksijen kısmi basıncının ve ITO film kalınlığının önemini de ele aldık. Ayrıca, FS ve PET alttaşları üzerindeki ITO filmlerinin THz özellikleri hakkındaki analizimiz, üretilen ITO filmlerinin THz filtreleri, modülatörler ve reflektörler gibi THz alanında potansiyel uygulamaya sahip olduğunu göstermiştir.

TABLE OF CONTENTS

LIST OF FIGURES

Figure **Page**

Figure **Page**

Figure **Page**

LIST OF TABLES

Table **Page**

CHAPTER 1

INTRODUCTION

Terahertz radiation is part of the electromagnetic spectrum (Figure 1.1.) lying between microwaves and the far-IR. This region has frequencies ranging from 0.1 – 10 THz and wavelengths from 3 mm to 0.03 mm. This spectral region is often referred to as the "THz gap" as these frequencies fall between electronic and optical means of generation. Terahertz radiation possesses unique characteristics not found in other portions of the spectrum. It matches in frequency the motion of an enormous range of chemical and biological molecules. Unlike far more energetic X-rays, T-rays do not have sufficient energy to "ionize" an atom by knocking loose one of its electrons. This ionization causes the cellular damage that can lead to radiation sickness or cancer. Since T-rays are non-ionizing radiation, like radio waves or visible light, people exposed to terahertz radiation will suffer no ill effects. Furthermore, although terahertz radiation does not penetrate through metals and water, it does penetrate through many common materials, such as leather, fabric, cardboard and paper (Ferguson and Zhang 2002).

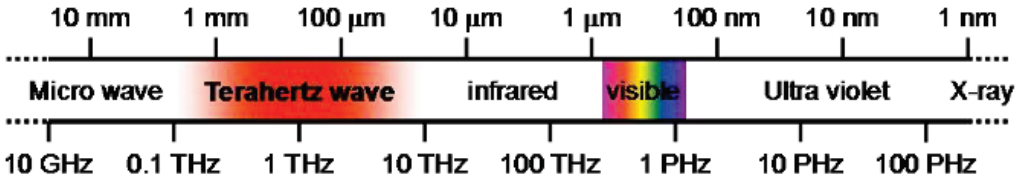

Figure 1.1. The electromagnetic spectrum with THz gap.

This gap of the spectrum is extremely important. It is the most scientifically rich band of frequencies in the entire spectrum. Researchers have discovered over the past 20 years that organic molecules resonate at frequencies in this range. This means that the presence and composition of organic matter can be detected by Terahertz radar sending out terahertz frequencies. This has many interesting applications. The military and other security organizations are requesting hand held Terahertz radar to remotely detect the presence of explosive materials, poison gases, ceramic weapons, and biological warfare

agents like viruses and bacteria. The medical community has shown that terahertz waves can detect the presence of cancer, viruses, bacteria, and other diseases instantly without surgery, biopsies, or other expensive procedures making this an important and urgent application of terahertz waves. Pharmaceutical and Agricultural companies are investigating the use of terahertz waves in quality control and research.

Figure 1.2. shows some of the applications of THz wave such as; fingerprint chemical and biological terror materials in package, find concealed weapons, widen frequency bands for wireless communication, control quality of pharmaceuticals and detect the human body diseases.

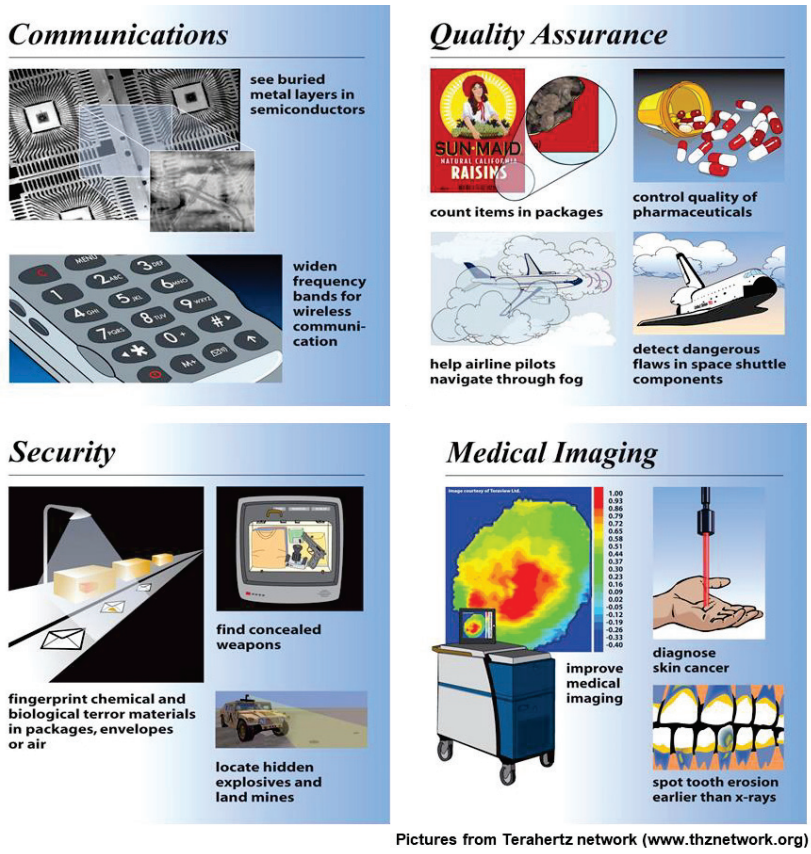

Figure 1.2. Some applications of THz wave.

Communication band for the THz have several benefits relative to the infrared and microwaves. Also, Better bandwidth compared to Microwave and fewer foggy weather compared with IR are the other benefits for the THz band. In addition, by using the broad THz bandwidth, protected communication band can be introduced in the THz frequency range.

Indium tin oxide (ITO) thin film is one of the most commonly used materials among the Transparent conducting oxides (TCOs) thin films due to its relatively low resistivity and high optical transmittance in the visible region of the em spectrum due to its large bandgap of about 3.70 eV (Tang and VanSlyke 1987, Tuna et al. 2010).

Transparent antennas to use in the solar panels, vehicle communication and ultra-high-speed networks like 5G have been continually built-in recent years. In order to get maximum efficiency from the solar cell by decreasing the shadowing area using transparent patch antenna operating at 28 GHz is discussed by using the TCO thin films by Ali et al. (Ali et al. 2017). Thampy et al. analyzed the ITO- and FTO-based transparent U-shape patch antennas, which is operated at 0.75 THz (Thampy, Dhamodharan, and Nanostructures 2015). Colombel et al. investigate the applicability of the Multilayer ITO/Metal/ITO thin films with low electrical properties and relatively moderate transparency in the Terahertz frequency band (Colombel et al. 2009). Moreover, Hong et al. investigate the applicability of transparent multilayer IZTO thin film patch antenna at 2.45 GHz frequency (Wi-Fi band) (Hong, Kim, and Jung 2016).

Due to the growing need for the high-speed data transmission, the working frequency of the wireless communication has been directed to the Terahertz frequency. Moreover, operating frequency needs higher frequencies, because commonly used GHz frequency has a low bandwidth (Federici and Moeller 2010). Moeller et al. have showed the usefulness of this THz frequency band by getting the 2.5 Gb/s high transmission rate at 0.625 THz (Moeller, Federici, and Su 2011). However, this high frequency band can be used for the relatively small distance (a few meters) due to the power limitations, even if this high-speed transmission rates are interesting (Sharma and Singh 2009, Koenig et al. 2013).

Today, THz technology is a hot topic (Dhillon et al. 2017). For the THz technological applications, the implementations of THz technologies need high-performance THz imaging and spectroscopy system components such as THz filters (Li 2010, Cai et al. 2018), modulators (Kai-hong and Jiu-sheng 2019, Shi et al. 2018), reflectors (Zhu et al. 2010, Zhao et al. 2017, Lai et al. 2013, Yang et al. 2020) etc.. Among these THz system components, the THz reflectors are very important for the THz measurements and paths between emitter and detector, and measurements (Yang et al. 2020, Lai et al. 2013, Hashimshony et al. 2001).

For the research on the THz properties of ITO thin film is currently at an early stage with relatively few studies on its application in the THz field (Brown et al. 2015,

Yang et al. 2020, Shi, Song, and Zhang 2018, Nebioğlu et al. 2017). High conductivity (low resistivity) properties of ITO thin films lead to high reflection (low transmission) of THz waves with high transparency in the VIS/NIR region of the electromagnetic spectrum. Transparent conducting thin films, not only ITO but also the other thin films have lots of applications possibilities in the THz field. The transparent thin film devices have critical feature to enhance the performance of the THz systems (Yang et al. 2020).

The aim of this work presented in this thesis can be classify as four sections. First one is to designing CW THz imaging system and take THz images of various samples (e.g., leaf). Second one is to understand the effects of high electrical currents annealing on the ITO thin films on Borosilicate substrate in air and vacuum ambient and improve the optical, electrical and structural properties of the films. Third one is to investigate the terahertz optical performance, UV/VIS/NIR transmittance, electrical and structural properties of ITO thin films on Fused Silica substrate by changing the thickness of ITO films and applying electro-annealing processes. Finally, forth one is to understand the effects of deposition parameters such as Oxygen gas flow and roll to roll (R2R) rotational speed on the grown ITO thin films on PET substrate and investigate the terahertz optical performance, UV/VIS/NIR transmittance and electrical properties of ITO thin films on PET substrate.

CHAPTER 2

BACKGROUND

The background information given in this chapter will be classified as Terahertz wave and Transparent conducting oxide (TCO). At first, a brief introduction about THz sources and detectors, and THz imaging will be discussed. Secondly, properties of ITO, which is the most used material within the Transparent conducting oxides, will be mentioned.

2.1. THz Sources and Detectors

Sources

In this part, some of THz sources such as free-electron sources, THz lasers, frequency conversion systems, photocurrent sources and superconducting IJJ THz sources will be briefly discussed.

In Free-electron lasers (FEL) (Brau 1988), which is the type of free-electron sources, work in the following manner. An electron population is stimulated using a short optical pulse. These excited electrons are then accelerated to relativistic speeds and passed through a magnetic array. This causes the electrons to oscillate in a sinusoidal pattern, thereby radiating narrowband THz radiation.

Backward wave oscillator (BWO) is the another type of free-electron sources (Lewen et al. 1997). Working principle of BWO based on projecting a beam of electrons into a counter-propagating and slowly oscillating electromagnetic field, which leads to compression and oscillation of the beam. This results in emission and magnification of THz radiation.

Quantum cascade laser (QCL) is another example of a THz laser. It works in the following manner. The material is designed to have the step potentials through periodic semiconductor material stacks (Köhler et al. 2002). An injected carrier tunnel through the array of potential barriers and emit THz photon each time it tunnels.

Photoconductive (PC) antennas work as follows (Darrow et al. 1990). A semiconductor, generally gallium arsenide (GaAs), has two parallel strip-line antennas held at some potential difference. In order to excite carriers in the gap between the two antennas, optical pulse is utilized. The subsequent movement of the electrons and holes causes a time-dependent current and emits THz radiation.

Compact, battery-operated T-rays source was discovered in 2007 by scientists at the U.S. Department of Energy's Argonne National Laboratory (Ozyuzer et al. 2007). This new type of terahertz source is based on high-temperature superconducting crystals which are composed of stacks of Josephson junctions. When a voltage is applied to the junction, an ac current generated and flows back and forth across the junction. This working principle of this terahertz source is known as the Josephson Effect. The frequency electromagnetic fields produced by alternating current can be tuned by the applied voltage. Frequencies in the terahertz range can be obtained by applying voltage around two millivolts per junction.

Detectors

Incoherent and coherent detection are the two categories of the detection of THz radiation.

Power measurements are performed by incoherent THz detectors. Initially bolometers were used to detect thermal (THz) radiation by measuring the change in resistance across a small thermal mass when the mass is heated (Richards 1994). One of the problems with bolometers is that they usually need temperatures of liquid helium to detect THz radiation. Golay cells, which are another method of thermal detection (Golay 1949), depend on the expansion of a small volume of gas to deform the flexible mirror and modulate a signal from an LED onto a photodetector. Lastly, pyroelectric detectors are another method of thermal detection (Beerman 1969). These detectors depend on the heating of a crystal to modify the polarization instantaneously.

To extract frequency dependence from a transmitted signal, coherent THz detectors are employed. Photo-conductive switches operate in similar manner as PC antenna. First, an optical pulse is used to excite carriers between two strip-line antennas when there is no voltage bias between them. The THz pulse would then strike the same spot as the optical pulse, inducing a current. In a similar manner to optical rectification, electro-optic sampling utilizes a nonlinear optical crystal. The THz pulse is incident on

the nonlinear optical crystal which induces a birefringence in the crystal. Physically, this means that the refraction index in the crystal varies based on the polarization of the event. The polarization of the reference optical beam will be rotated by this birefringence as it moves through the crystal. This rotation is proportional to the THz electric field.

2.2. THz Imaging

It is possible to roughly categorize imaging techniques into two major categories, passive THz imaging and active THz imaging techniques.

2.2.1. Passive THz Imaging

The contrast in the passive imaging is obtained from the generated thermal radiation from the sample or reflected from external thermal generator sending to the sample. For instance, passive imaging can be used in the astronomy in order to investigate the sky bodies (Mueller, Fontanella, and Henschke 2000). For this approach, there is no need of the THz sources. Use of the highly sensitive THz detectors (or detector arrays) is enough to get the image.

When a powerful local oscillator is available, heterodyne techniques are commonly used. For example, a bolometer combined with circuitry was developed by Rodriguez-Morales et al. (Rodriguez-Morales et al. 2006), which is operates at 1.6 THz frequency generate from the far-IR local oscillator. Moreover, Mann et al. have extensively investigated the THz CCD camera (Mann 2006). Some THz images (one of them shown in Figure 2.1.) obtained by the scanning a single pixel superconducting bolometer by Shen et al. (Shen et al. 2008).

Figure 2.1. A passive THz image of A handgun and a rectangular piece of standard RF anechoic material are concealed under the clothing (Shen et al. 2008).

Imaging technology up to 100 GHz is much more advanced and devices from several vendors are commercially available. Moreover, few commercial passive imaging systems are available, operating at 250 GHz (Thruvision Ltd.).

2.2.2. Active THz Imaging

Generated radiation goes towards to the object and the sending signal is transmitted, reflected, or scattered form the object and then detected by a detector. This approach is named as active imaging. The low contrast of passive detection can be overcome by strong scene illumination in an active imager, particularly at high frequencies where spatial resolution is strongest. By increasing the transmitted power, penetration through thick samples can also be achieved (Younus 2011).

2.2.2.1. Continuous Wave THz Imaging

In the standard CW THz system, fixed or adjustable THz sources is used. Since the first designed CW THz systems, there have been many developments in this field.

In the CW THz imaging system, there is no phase information usually, because the source is not synchronized to an optical source employed for sampling, so the source and detector are separate devices rather than two components of connected devices. However, an up-conversion of THz radiation accompanied by homodyne-detection was used in the work performed by Nahata and colleagues (Nahata, Yardley, and Heinz 1999).

In order to evaluate the phase and amplitude of the generated 0.6 THz signal from oscillator, electro-optical sensing with a femtosecond laser was also used (Löffler et al. 2007). Jun yang et al. show simultaneously CW imaging using a pyroelectric detector for non-destructive examination of samples concealed in package (Yang et al. 2008). In the CW THz imaging system, in order to the detect the incoming THz signals, a bolometer, golay cell or pyroelectric detector is generally used. For direct detection, array detectors are also accessible, including pyroelectric cameras, germanium detector arrays (Fujiwara et al. 2003) and micro-bolometer arrays (Lee et al. 2006).

CW THz imaging is beneficial for certain applications due to the large fix frequency range and narrow bandwidth. One significant benefit of imaging with a single frequency source is the adjustment of the frequency of the THz source in order to compare the THz imaging at different THz frequencies. That is important, because in the stand-off THz imaging, it is difficult to get fine THz images due to the air absorption caused by the water vapor. However, atmospheric attenuation is reduced at some frequencies in the THz range, where the setting frequency has nearly no air absorption. A significant benefit is the ability to set the THz source to a water window.

Using a CW THz imaging system, photo-mixing and parametric oscillators can be used to acquire the spectral information by adjusting the THz wave in the broad bandwidth. To image powders within an envelope, a spectrum is obtained for each pixel by adjusting the source between 1 and 2 THz by using the adjustable THz parametric oscillator and a pyroelectric detector by Kawase et al. (Kawase et al. 2003). In this range, even in powdered form at room temperature, these crystalline materials have considerable THz absorption which can be employed for material identification with a multispectral analysis (Kawase et al. 2003).

Figure 2.2. gives an example of THz images taken using a CW imaging system. It displays a picture of a concealed plastic explosive Semtex sample (plastic explosive containing RDX and PETN) surrounded by two confusing materials at different frequencies of identical density and temper. Semtex can be identified by taking various images using 200 GHz to 900 GHz frequency components.

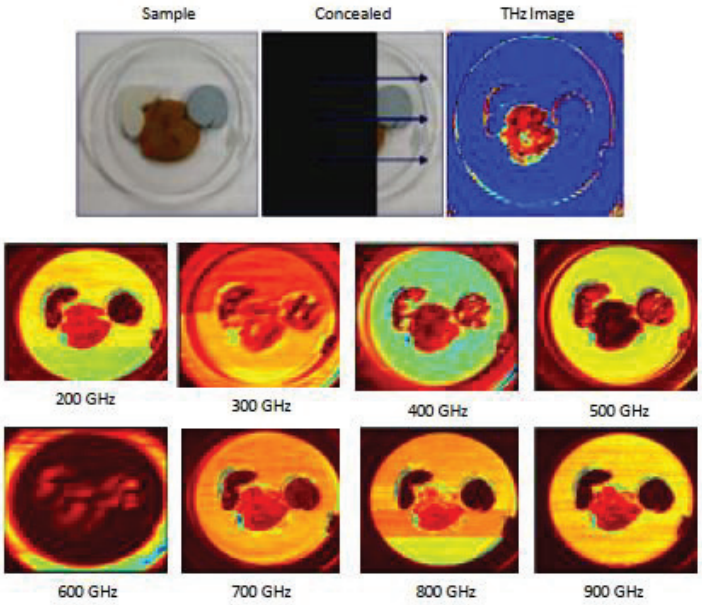

Figure 2.2. Reflective CW THz image of a concealed sample composed of Semtex and two other confusing materials (Source: TeraView).

A particular method for associating the radiation obtained with its position in space involves imaging with a CW system. There are two widely used methods which are a raster scan of a focused incident beam, or the formation of an image on an array of detectors.

A single detector is used in the former to detect the maximum power of the beam, such as a Schottky diode, Golay cell or pyroelectric detector. This has the advantage of high dynamic range. However, the disadvantage is that the image must be formed point by point using a scanning system which is time consuming and cannot be applied to moving targets. An active field of research is still the development of a sensitive THz detector array (Ortolani, Di Gaspare, and Casini 2011).

There are commercially available pyroelectric arrays, however their sensitivity in the THz range is low and they are too low to provide large targets with high-resolution images. Detector arrays often have the drawback of being seriously affected in the focusing system by distortions and aberrations, while the beam can be oriented to a diffraction-limited location for a raster scanning system.

2.2.2.2. Pulsed THz Imaging

In general, a THz pulsed imaging system relies on pulses of electromagnetic waves in the picosecond duration range. Broadband THz radiation are produced using these optical pulses. The THz pulses are based on the sample and the time-domain coherently records the resulting temporal waveform. THz pulses are focused on the sample and the resulting temporal waveform is recorded consistently in the time domain. In the 1980s, Lucent Bell Laboratories and other researchers developed the fundamental technology and method of pulsed THz imaging (Auston and Smith 1983, Fattinger and Grischkowsky 1988). Early THz-TDS instrumentation, however, was large and restricted to an optical table. Currently, the most advanced commercial THz-TDS instruments are compact, with remote scanning sensors coupled with interchangeable fiber-optics. For a wide range of pulsed THz measurements, these instrumentation platforms provide an efficient, compact, robust and highly flexible system (Picometrix and Teraview).

Most information about the sample and the highest SNR is given by this active imaging process. Broadband character and coherent detection are the key benefits, so that the amplitude and phase of the THz electric field can be achieved at once. In order to give the spectra, the temporal waveforms can also be Fourier Transformed. This enables the refractive index and absorption coefficient of samples to be reliably determined without restoring the Kramers-Kronig relationship. Raster scanning of the sample with a focused THz beam was the earliest pulsed THz imaging experiment (Hu and Nuss 1995). In this process, the change in the refractive index is seen in the time delay and pulse phase, while the difference in density modulates the amplitude of the pulse peak. Various imaging configurations have been shown since this ground breaking work, and even produced commercially, with great examples of THz imaging. This technique is commonly used in sensing and spectroscopic imaging as many typical packaging materials are almost transparent to THz radiation and many chemical compounds in the THz region exhibit characteristic fingerprints of absorption.

By measuring the time-of-flight of the THz pulses, pulsed THz reflection imaging offers extra capability to examine the structure of a layered sample. Mittleman et al. first showed the resulting 3D images in 1997 (Mittleman et al. 1997). Parts of the THz pulse will return from any structural interface which has a change in its refractive index in reflection mode (Wang and Zhang 2004). A series of interfaces will lead to a series of

pulses within the THz waveform that have spacing proportional to the distance between the interfaces, as the speed of light within the sample is finite.

One of the essential considerations is depth resolution in a time-of-flight imaging system. To enhance this depth resolution, there are many different techniques that can be used. Interferometry in a mode that is the time-domain analog of optical coherence tomography is one technique (Johnson, Dorney, and Mittleman 2001). Optical coherence tomography uses an interferometer to temporarily resolve a broadband light pulse by interfering it with a reference pulse, and thus determining time-of-flight in reflection geometry. A very high depth resolution of 1μm has been shown (Kitahara, Tani, and Hangyo 2010).

Spatial resolution is one of the obvious drawbacks of all of the THz imaging techniques mentioned so far. The spot size of a focused beam is approximately equal to the wavelength multiplied by the f-number of the focusing optics, with a diffraction-limited optical system. As a consequence, the smallest features in an image that can be resolved are normally in the order of the illumination wavelength. One considers a spatial resolution (~ 0.5 mm) for radiation at 1 THz that is close to the resolution of the human eye. The applicability of THz imaging is obviously constrained by this resolution. The study of near-field techniques has been one of the most active research areas in the THz community, since the first demonstration of THz sub-wavelength imaging in 1998 (Hunsche et al. 1998). Dynamic aperture (Chen and Zhang 2001) and aperture less near-field THz imaging have been established and commonly used among these methods (Van der Valk and Planken 2002, Chen, Kersting, and Cho 2003). A spatial resolution as low as 7 μm at 0.2 THz could be obtained in near field imaging with sub-wavelength aperture (Mitrofanov et al. 2001). Imaging with a 12 μm resolution (λ/17) was shown with a CW THz source at λ=207 μm (Ishihara et al. 2006). The limit of each of these techniques can be determined by the amount of light transmitted through the aperture. More details can be found in the article by Chan et al. (Chan, Deibel, and Mittleman 2007).

2.3. Transparent Conducting Oxides

Transparent conducting oxides (TCOs) are materials that exhibit superior electrical and optical properties. TCOs frequently consist of one or two metallic elements and oxygen. Their properties depend on the elements they contain. The quality of the

material, which depends on the method of deposition, affects the features of the material. TCO films with a transmission above 90% and resistivity around 10^{-5} Ω.cm were fabricated using pulsed laser deposition and magnetron sputtering (Suzuki et al. 2001, Ray et al. 1983).

Badeker firstly reported TCOs in 1907. In his primary work, it was shown that by oxidizing cadmium thin film, it can be made transparent and it can still conduct electricity. Since then, it has been demonstrated that many other materials possess superior electrical and optical properties. Tin doped indium oxide (ITO), aluminum doped zinc oxide (AZO), antimony doped tin oxide (ATO), and fluorine doped tin oxide (FTO) are some of the most commonly used TCOs today (Ginley, Hosono, and Paine 2010).

2.3.1 Indium Tin Oxide

ITO is one of the most employed material among the TCOs. Therefore, it is used in many applications such as flat panel displays (Lee et al. 1997), solar cells (Chopra, Major, and Pandya 1983), heat mirrors, anti-static coatings, solar cells (Chopra, Major, and Pandya 1983), and OLEDs (Kim et al. 1998). ITO films have attracted great attention due to its excellent properties, including perfect adhesion to the substrates, good conductivity, high transmission in the visible region, easy patterning performance, stable chemical properties. These specific properties are heavily based on the nature of impurities in ITO thin films, their microstructure, stoichiometry, and the deposition method.

ITO thin films can be fabricated using several methods, including magnetron sputtering (Koseoglu et al. 2015, Tuna et al. 2010, Zhang et al. 1999), thermal evaporation deposition (Salehi 1998), electron beam evaporation (Sheu et al. 1998), spray pyrolysis (Major and Chopra 1988), pulsed laser deposition methods (Kwok, Sun, and Kim 1998), chemical vapor deposition (Hu and Gordon 1992) and dip-coating (Nishio, Sei, and Tsuchiya 1996). Among these techniques, the direct current (DC) and radio frequency (RF) magnetron sputtering methods are the most are commonly used methods. A variety of factors, including optical transparency, homogeneity of the film, electrical conductivity and surface morphology, determine the ITO film quality. Furthermore, the structure and doping concentration are also influenced by the deposition methods and the process conditions.

The crystal structure of ITO is body centered cubic bixbyite, as for In_2O_3, when not heavily tin doped (Figure 2.3.). If the material is fabricated under high pressure and high temperature, a corundum structure can be obtained (De Wit 1977). There are 80-unit cell atoms of the cubic bixbyite structure (Marezio 1966). The lattice constant can be tuned by changes in the partial pressure of oxygen during deposition. Fan et al. recorded different values depending on the partial pressure of the oxygen (Fan, Bachner, and Foley 1977). The space group is Ia3 (Mason et al. 2003, Janowitz et al. 2011), and either b-sites or d-sites are located in the indium atoms. While the b-sites have oxygen vacancies in the body diagonal, the d-sites have vacancies in the face diagonal. Unit cell includes 8 b- and 24 d-sites. The bixbyite structure of In_2O_3 can be seen in Figure 2.3. Tin is located at substitutional In sites in the Sn^{+4} form (Hamberg and Granqvist 1986). The Sn atom contributes to the concentration of the carriers with one electron. Oxygen vacancies are thought to contribute carrier concentration with two electrons (De Wit 1977, Okada et al. 2011, De Wit 1973).

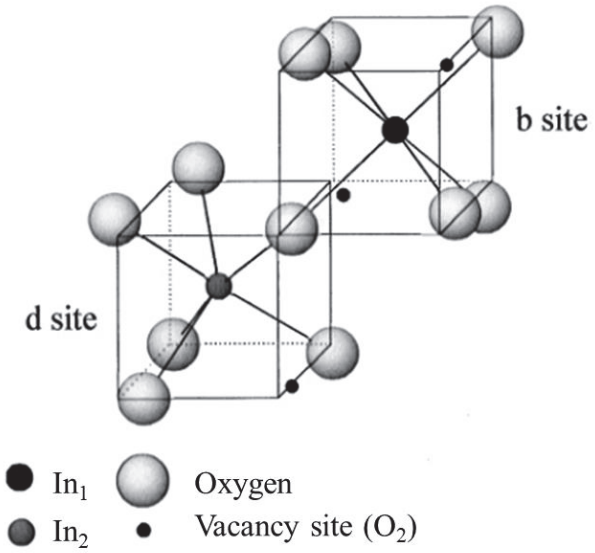

Figure 2.3. The cubic bixbyite structure of In_2O_3 (In_2=d-site and In_1=b-site.) (Quaas, Eggs, and Wulff 1998).

2.3.1.1. Band Structure of ITO Films

Substitutional doping of In_2O_3 with tin forms ITO (Fan and Goodenough 1977). Tin substitutes indium atoms in the cubic bixbyite structure of In_2O_3. In ITO, Sn is

assumed to create an interstitial oxygen bond. It comes into being as SnO or SnO_2 with +2 and +4 valences, respectively. Sn^{+2} reduce to carrier concentration, since hole is formed, which act as a trap and decrease conductivity. Replacement of the In^{+3} by Sn^{+4} generate a donor level and release electrons to conduction band. However, In_2O_3 is normally deficient in oxygen. The oxygen vacancies lead to shallow donor just below the conduction band. They give two electrons at most behaving as doubly ionized donors. Consequently, the conductivity of the ITO relies on both oxygen vacancy donors and substitutional tin dopants.

In 1984, Hamberg et al. was suggested a basic band structure to describe the conduction mechanism in In2O3 (Hamberg et al. 1984). Figure 2.4. shows parabolic conduction and valance bands structure of both undoped and doped In_2O_3 schematically.

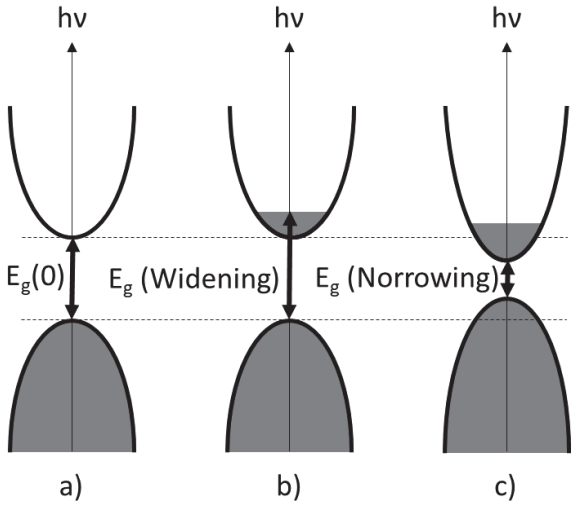

Figure 2.4. Schematic parabolic conduction and valance bands structure of a) undoped-Indium Oxide bands separated by the band gap $E_g(0)$, b) after heavy doping there is a bandgap widening due to filling lowest energy state of conduction band by carriers, c) band gap narrowing is occur due to further increase of carrier concentration.

In 1977, it is proposed that the conduction band is predominantly from In:5s electrons and the valence band is from O^{-2}:2p (Fan and Goodenough 1977). The Fermi energy is on the halfway between the energy bands in the case of stoichiometric In_2O_3. In_2O_3 is usually reduced a bit and these oxygen vacancies lead to shallow donor states just below the conduction band. E_f is between the donor level and the conduction band minimum in oxygen deficient In_2O_3 samples. The conduction band is curved upwards,

the valence band is curved downwards and the Fermi level is situated in the center of the band gap for un-doped In_2O_3. When Sn dopants are added, donor states form just below the conduction band. An impurity band is formed as the donor concentration rises, creating a degenerate semiconductor. In the conduction band, the lowest states are typically occupied as a result of heavy doping in material, which results in E_g widening (Figure 2.4. b)). Conversely, electron-impurity and electron-electron scatterings lead to reduction of band gap (Figure 2.4. c)).

The Sn:5s level is stabilized just below E_c in the case of ITO. Unlike oxygen vacancies (VO), which is a two-electron donor level, the Sn:5s level is considered as single electron donor level. Sn enters substitutionally in the cation sublattice as small amount of Sn is put into In_2O_3 lattice. Accordingly, Sn^{+4} substitutes In^{+3} and serves as a n type donor. When In_2O_3 is doped with Sn, it can be shown as $In_{2-y}Sn_yO_3e_y$. Therefore, donor levels of V_o and Sn:5s coexist and both of them give free electrons.

2.3.1.2. Electrical Properties of ITO Films

Electrical conductivity (σ) is based on the mobility (μ) and concentration (N) of the free carrier as follows:

$$\sigma = \mu N e \tag{2.1}$$

where e is the electron charge. To get highly conductive thin films, both high mobility and high carrier concentration are necessary. The electrical properties of oxide semiconductors are dependent on the oxidation state of the metal ingredient and on the nature and quantity of impurities in the films.

In ITO films, Sn, which behaves in the lattice as a cationic dopant, substitutes In. In has three valences. Hence, Sn doping causes n type doping of the lattice by supplying an electron. The neutrality of the charge is thus maintained. Thus, due to only Sn doping, the theoretical maximum carrier density is $3.0 \times 10^{20} \times C_{Sn}$ (at. %). In reality, however, the concentration of the carrier does not rise accordingly as expected (JIANQIAO 2006).

In order to increase the conductivity of the TCO material, a lot of work has been made to increase the number of free charge carriers through doping. While various successful doping techniques have been introduced, some restrictions exist till now. Since

the dopant atoms located in the random positions of the host, as the number of carriers increases, the doping process definitely disrupts mobility. Therefore, to achieve lowest resistance, mobility and carrier concentration should be optimized.

A study of tin doping in ITO using X-ray photoelectron spectroscopy (XPS) was proposed by Meng et al. (Meng, Macarico, and Martins 1995). Their findings showed that the rise in the carrier concentration induced by annealing is not due to the transition from SnO to SnO_2. It is verified that at any tin concentrations, divalent Sn anions do not coexist. The key explanation that restricts efficient Sn doping in the ITO is creation of the Sn_2O_4 neutral complex. In addition to the tin dopant, the oxygen deficiency plays a key role in defining the conductivity of ITO.

One efficient way to boost the film properties is effective post deposition annealing. Much work has been performed to examine the annealing effect on the quality of the ITO film (Hamdi et al. 1991, Shigesato, Takaki, and Haranoh 1992, Harding and Window 1990). In ITO films, while a low content of oxygen leads to the more metallic films, a high concentration of oxygen lowers the electrical conductivity. Hence, to achieve highly conductive and transparent ITO films, optimization of oxygen concentration is important. Upon post-annealing, optimum conductivity and transmission in the visible region can be achieved. Since the reduction in sheet resistance in thicker films was slower, the rise in conductivity because of vacuum annealing was ascribed to out diffusion of the excess oxygen atoms from interstitial positions (Bárdoš and Libra 1989).

Considering the major scattering mechanism common in polycrystalline semiconductors, the mobility of ITO films has been examined. There are several electron scattering sources that can affect the electrical and optical characteristics of ITO films. Since the carrier's mean free path is much smaller than the observed crystallite size, the contribution of the grain boundary scattering mechanism has no importance.

The temperature behavior of mobility shows the presence of other significant sources of resistivity, especially at low temperatures. Scattering of conduction electrons by ionized and neutral impurity centers has been shown to have a dramatic effect on the conductivity of oxide semiconductors. Erginsoy examine the influence of neutral impurities on the conductivity of oxide semiconductors with small degrees of ionization (Erginsoy 1950). Conwell and Weisskopf have calculated the relation between ionized impurities and film resistivity (Conwell and Weisskopf 1950). Using this method, Dingle 1955 tried to reproduce more clarified definition of the scattering effect (Dingle 1955).

With an increase in the dopant amount, the contribution of ionized impurity scattering raises. In 1981, Noguchi and Sakata investigate the data on carrier concentration and mobility to examine the scattering mechanism in ITO films (Noguchi and Sakata 1981). Their findings indicated that ionized impurity scattering is the main scattering mechanism for ITO films with (Sn)/(In) ratio below 0.1. In 1981, it is proposed that neutral impurities and other centers associated with poor crystallinity could restrict the conductivity of ITO thin films with a (Sn)/(In) ratio above 0.1 (Noguchi and Sakata 1981).

Bellingham et al. stated that because of the presence of ionized impurities, the conductivity of oxide indium tin oxide and amorphous indium films was primarily dominated by electron scattering (Bellingham, Phillips, and Adkins 1990, 1991, 1992). Their findings are in accordance well with Moore's ionized impurity scattering model (Moore 1967).

Also, variations of the film resistivity with carrier concentration are in line with the trend expected by the calculations of ionized impurity scattering. It has been verified that it is not necessary to invoke scattering by structural disorder, even in the case of an amorphous structure. Scattering in ionized centers thus tends to be an effective mechanism which clarifies the mobility behavior in ITO films. The measured lower mobilities, especially for films with high doping concentrations, are ascribed to the interaction of carriers with the scattering centers and/or the formation of neutral scattering defects that cause low carrier mobility due to the scattering.

2.3.1.3. Optical Properties of ITO films

In the visible and near-infrared region, ITO films show superior optical transparency. However, they are reflective to thermal infrared radiation. The absorption coefficient of ITO films is very low between the two absorption edges. For many applications, this special feature of ITO films has been utilized as a selective transmission layer.

The Sn doping of In_2O_3 can increase its direct and indirect band gaps. The increment in the carrier concentration results in a shift in the absorption edge of the ITO thin film towards the high energy side (Hamberg et al. 1985). The connection between the alteration in carrier concentration and the band gap shift was further clarified in 1979

by Ohhata et al. (Ohhata, Shinoki, and Yoshida 1979). They demonstrated that the widening of the band gap is proportional to carrier concentration as $N^{2/3}$. Bellingham et al. have also documented a similar change of the band gap with carrier concentration (Bellingham, Phillips, and Adkins 1990).

Basically, it is possible to understand the band gap widening in the film by Burstein-Moss (BM) shift (Burstein 1954). It can be noticed when film's electron density exceeds the Mott critical density (Mott 1974). In cases where the carrier concentration in the film passes over the Mott critical density too much, the conduction band is partially filled, the lowest states are blocked causing a widening of the band gap. On the other hand, electron-impurity and electron-electron scattering results in bandgap narrowing. In ITO, since these effects are very important, they have been researched (Roth, Webb, and Williams 1982, Stern and Talley 1955, Hamberg and Granqvist 1986).

CHAPTER 3

EXPERIMENTAL

3.1. THz Imaging System

The schematic view of the Terahertz (THz) imaging system is shown in Figure 3.1. THz imaging system consist of the THz Source operating in the frequency range 0.500-0.750 THz which has a RF Generator, frequency counter and VDI WR1.5 AMC (Amplified / Multiplier Chain (Amplified / Multiplier Chain), 90° off axis parabolic mirror (4 pieces), x-y motion mechanism (x axis: homemade linear motorized stage with step motor, which is controlled by Lab-View program using Lead-Shine step driver and MC USB201 controller / y axis: Newport linear motorized stage, which is controlled by Lab-View program using Newport ESP 301 controller) with sample holder and Golay Cell as a detector.

The THz wave, emitted from WR1.5 AMC, was first modulated by a function generator (Stanford Research Systems-DS335 Synthesized Function Generator) with 15 Hz frequency and 2.5 V peak to peak voltage using the TTL modulation option of the WR1.5 AMC, and then collimated by a pair of 90° off-axis parabolic mirrors and focused into the sample holder origin. After the interaction of the THz waves and sample the transmitted THz wave was collimated by a second pair of 90° off-axis parabolic mirrors and focused into the Golay Cell. Finally, the collected signals by the Golay Cell were analyzed by a lock-in amplifier (Stanford Research Systems 830 Lock-in Amplifier). In order to get THz image of the sample, direct 2D (x-y) scanning of the sample were performed and the collected signals give us the THz image.

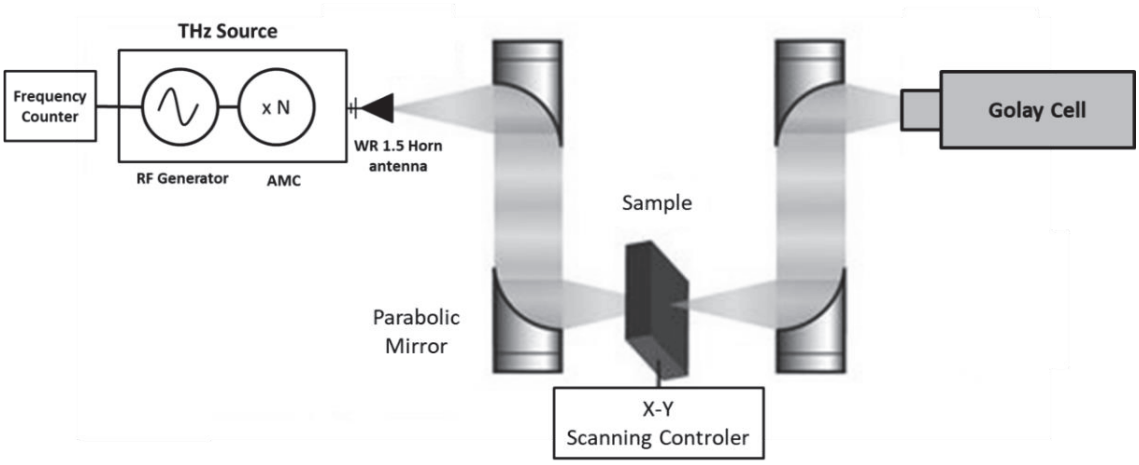

Figure 3.1. Schematic view of the THz Imaging System

3.1.1. THz Source

In the first part of the THz Source there is a simple frequency synthesizer that works alone and is used to pump AMC in the 8-20 GHz range. Since this frequency synthesizer is locked to the high-quality crystal reference, the synthesizer gives excellent frequency stability. In addition, the synthesizer can be digitally controlled by a computer. The second part of the THz Source also has a simple frequency counter where we can observe the frequency. At the last part is WR1.5 AMC which is the main part of THz source. The WR1.5 AMC generates THz wave with varistor-mode frequency multipliers based on planar GaAs Schottky diode technology.

3.1.2. Frequency Counter

Frequency counter is an electronic instrument used to measure frequency. Frequency is defined as the number of events of a particular type that occur in a given time period. Frequency counters usually measure the number of oscillations or pulses per second in a recurrent electronic signal.

3.1.2.1. Operating Principle

Most of the frequency counters operate using a counter that accumulates the number of events that have occurred over a specific time period. After a predetermined time known as gate time (e.g., 1 second), the value of the counter is transmitted to a display and the counter is reset to zero. If the measured event repeats itself with enough stability and the frequency is significantly lower than that of the clock oscillator used, the resolution of the measurement can be greatly improved by measuring the time required for an entire number of cycles, rather than counting the number of entire cycles observed for a pre-set duration (often referred to as the reciprocal technique). The internal oscillator that supplies the time signals is called the time-base and needs to be calibrated precisely. Frequency counters, which operate on the same principles as lower frequency counters, are also common. Frequently, they have greater range before they overflow. Many designs for very high frequencies use a high-speed pre-scaler to reduce the signal frequency to a point where normal digital circuitry can work. By taking this into account, displays on such instruments continue to show the correct value. Microwave frequency counters can measure frequencies up to nearly 100 GHz. Above these frequencies, the signal to be measured is combined with the signal from a local oscillator in a mixer to produce a signal with a difference frequency low enough to be measured directly.

3.1.2.2. VDI 0.5-20 GHz Frequency Counter

VDI frequency counters were designed to measure the frequencies generated from the signal generators. VDI frequency counter works in the 0.5-20 GHz frequency ranges with an input power of 0-10 dBm. The display resolution is 7 digits, but 32 bits of resolution can be read through a USB cable to a computer. The measurement time can be set to perform fast measurements, such as 4 kHz within 100 ms. The dimension of the counter is relatively small (3.75’ x 3.75’ x 2’) and is powered by a USB cable connected to a computer (Figure 3.2.).

Figure 3.2. VDI 0.5-20 GHz Frequency Counter

In our system, we use a 10 dB Coupler (ATM C126H-10) to multiply the reference RF signal from the VDI Synthesizer into two at the same frequency and send one to the frequency counter and the other to the WR1.5 AMC. In this way, we can measure the value of the generated signal by the frequency counter.

3.1.3. Frequency Synthesizer (FS)

A frequency synthesizer generates many precise frequencies from a single reference frequency. A frequency synthesizer can substitute the expensive crystal resonator array in a multi-channel radio receiver. A reference frequency is supplied by a single crystal oscillator and other frequencies are generated by the frequency synthesizer. Frequency synthesizers are used in many devices such as mobile telephones, radio receivers, GPS systems and satellite receivers, since they can be easily controlled by digital circuitry and are relatively inexpensive. To produce the desired output signal, frequency synthesizer can combine frequency multiplication, frequency division, and frequency mixing operations.

3.1.3.1. VDI Synthesizer

VDI synthesizers (Figure 3.3.), which operates as PLL working principle, are specially designed for VDI sources and receivers with targeted properties for Terahertz

applications. The 8-20 GHz frequency range and 17 dBm power are compatible with most VDI multiplier chains. Using a PC via a USB connection with the software, frequency can be controlled. Stepping the continuous wave frequency can be performed at 1mS for step sizes of 40 MHz using USB commands. To provide frequency modulation, the frequency can be continuously scanned linearly across any part of the band, with step times as low as 4 ns and resolution better than 20 Hz. Similarly, the phase can be controlled within 0.5 degrees. Frequency step size and step time can be changed to frequency modulate over +/- 25 MHz at a rate of 3 kHz and sweep from 8-20 GHz in 170 ms with minimal frequency error. In order to synchronize other instruments at the start of a scan, trigger output signal is provided. The synthesizer can be phase locked to 10 or 100 MHz reference, mounted in a single slot with the VDI multiplier chain, or supplied separately.

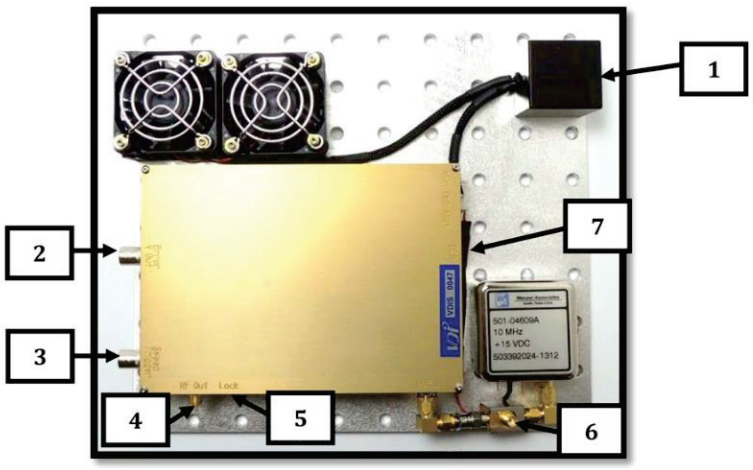

No.	Part Description	Specification
1	DC Power Connection	10-pin 2B Series LEMO
2	Error V Out	BNC(f)
3	Sweep Trigger	BNC(f)
4	RF Output	8-20GHz; ~16dBm [SMA(f)]
5	Phase Lock Light	LED ON = LOCKED
6	10MHz Output	SMA(f)
7	USB Synthesizer Control	USB Type B

Figure 3.3. Picture of theVDI Synthesizer and specifications

3.1.4. VDI WR1.5 AMC

High performance frequency expansion is provided by VDI's AMCs to microwave sources in the THz range. In order to get tailored performance, low phase noise is combined with high test port power by these modules. Standard features include TTL controlled on / off mode up to ~ 2 kHz and voltage-controlled RF attenuator (UCA). Performance options are included in Micrometer driven variable RF attenuator such as increased amplitude modulation ratio to combine free space, test ports, funnel antenna, and waveguide torsion. VDI AMCs offer full waveguide band frequency generation and switching operation, which are arranged in a size of 8'x5'x3' for use in independent studies. Some parameters of WR1.5 AMC (Figure 3.4.) THz source can be seen in the table. THz source provides much higher and more useful power than any full band solid state source. The output power graph of WR1.5 AMC versus frequency can be seen from Figure 3.5.

Figure 3.4. VDI WR1.5 AMC

Table 3.1. Specifications of VDI WR1.5 AMC

VDI part	Band (GHz)	RF Input Mode	Input Frequency (GHz)	Multiplication Factor	Output Power (dBm)	
					Typical	Minimum
WR1.5 AMC	500-750	Standard	9.3 - 13.9	54	-21	-30
		High	27.8 - 41.7	18		

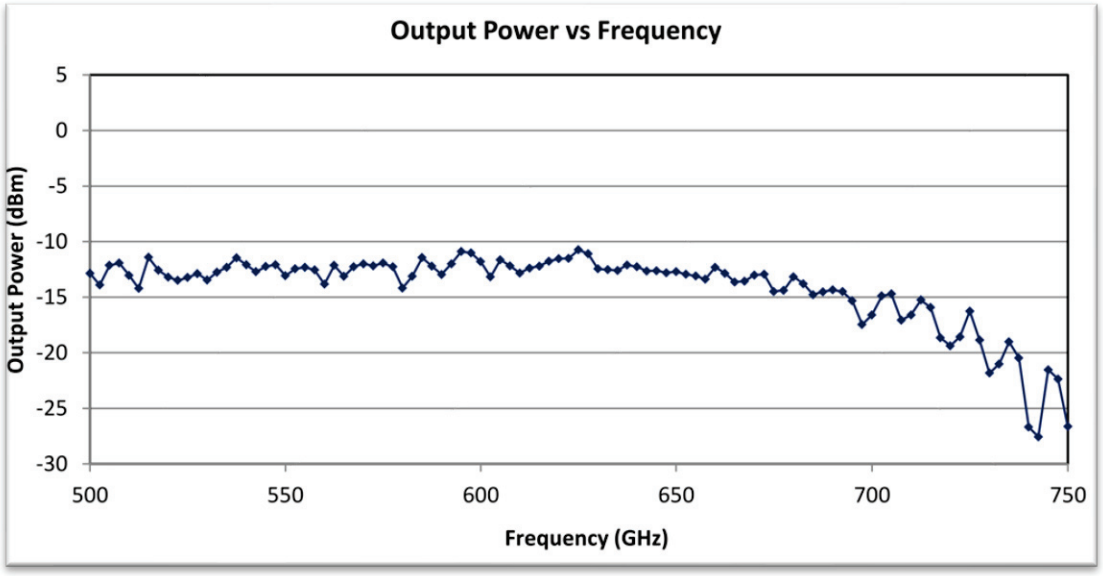

Figure 3.5. Output power of the WR1.5 AMC vs. frequency graph

By mounting the diagonal horn antenna received on the WR1.5 AMC, we minimized the extra power loss. The schematic view of the diagonal horn antenna is shown in Figure 3.6. a). In addition, in the Figure 3.6. b) the picture of WR1.5 AMC with mounted Horn antenna.

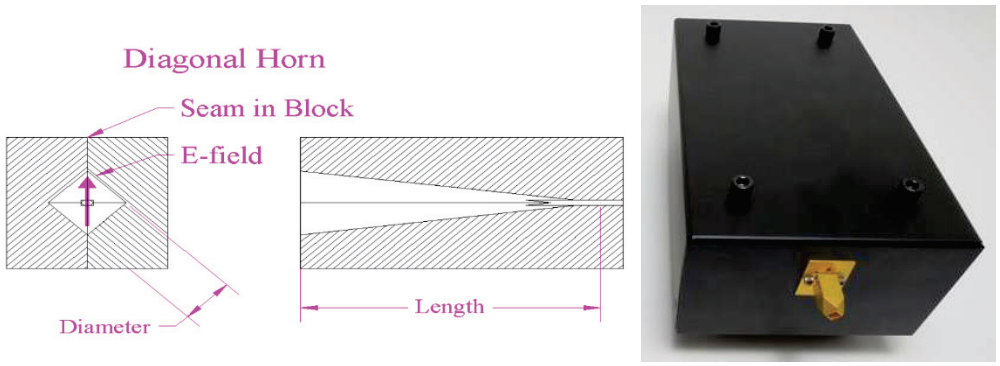

Figure 3.6. a) Schematic view of the diagonal horn antenna for the WR1.5 AMC and b) the picture of WR1.5 AMC with mounted Horn antenna.

Table 3.2. Specifications of diagonal horn antenna for the WR1.5 AMC.

Waveguide Band	Frequency (GHz)	Horn Type	Horn Length (mm)	Aperture Diameter (mm)	Taper Half-Angle (deg)	Full 3 dB Beamwidth (deg)	Gain (dB)	Beam Waist Radius (mm)
WR1.5	500-750	Diagonal	11.8	2.4	5.8	12	25	0.89

3.1.5. Golay Cell

The type of the golay cell used in this THz imaging system is Tydex GC-1P opto-acoustic detector, which consists of a front chamber, an optical microphone, and a preamplifier. The optical arrangement of the detector is schematized in Figure 3.7.

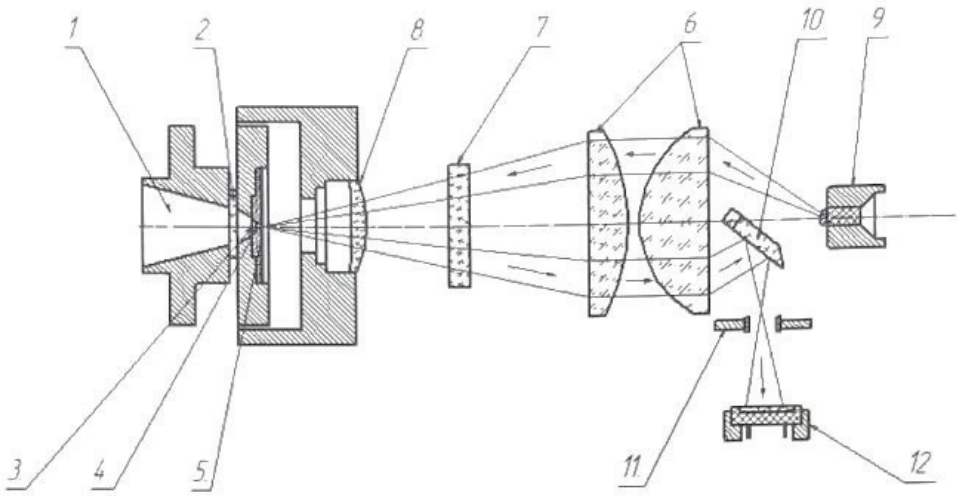

Figure 3.7. Optical schematic of GC-1P Golay Cell (Source: Golay Cell-User Manual)

A modulated beam of radiation passes entrance cone (1) and entrance window (2) to reach translucent film (3) in the middle of the chamber. The energy absorbed in the film heats the gas in the chamber, causing the pressure to oscillate at the modulation frequency. These oscillations go through channel (4) to mirrored membrane (5), which serves as a wall of the chamber and, simultaneously, as the mirror of the optical microphone.

The image of light emitting diode (9), which serves as an optical microphone, is projected by condenser (6) through optical raster (7) located in the focal plane of lens (8)

onto the mirrored membrane. This radiation is reflected back through the lower half of the raster and refocused by mirror (10) and diaphragm (11) onto photodiode (12).

Because of the variations in the gas pressure, the membrane oscillates, periodically displacing the image of the transparent lines of the upper half of the raster from the opaque lines of its lower half, which is directed toward the photodiode.

A preamplifier, based on an operational amplifier and a dual FET, converts the oscillating photocurrent into an alternating electric signal, “the photodiode load resistor being connected into the negative feedback circuit of the amplifier. The signal voltage is supplied via a connecting cable to the input of an external recording and/or displaying device.

3.2. Thin Film Deposition Using DC Magnetron Sputtering

Sputtering is one of the most preferred deposition techniques for the deposition of transparent conductor oxides in order to get high quality thin films. Thin films with higher purity and better controlled composition can be achieved by the sputtering process, which provides thin films with fine adhesion to the substrate and uniformity and better control of the thin film thickness (Wasa and Hayakawa 1992, Ohring 2001, Steckelmacher 1991).

In dc magnetron sputtering the cathode (to which the target material is attached) is held at a large negative voltage relative to the substrate and walls of the chamber. By field emission of electrons from the cathode, Argon plasma is occurred in the chamber. Magnetron, which is a configuration of magnets located under the target, serves to keep electrons close to the target surface, thus increasing ionization in this region (Figure 3.8). Then, the positively charged Ar ions are then accelerated towards the cathode, remove the atoms from the target and cause a thin film to form on the substrate (Figure 3.9.).

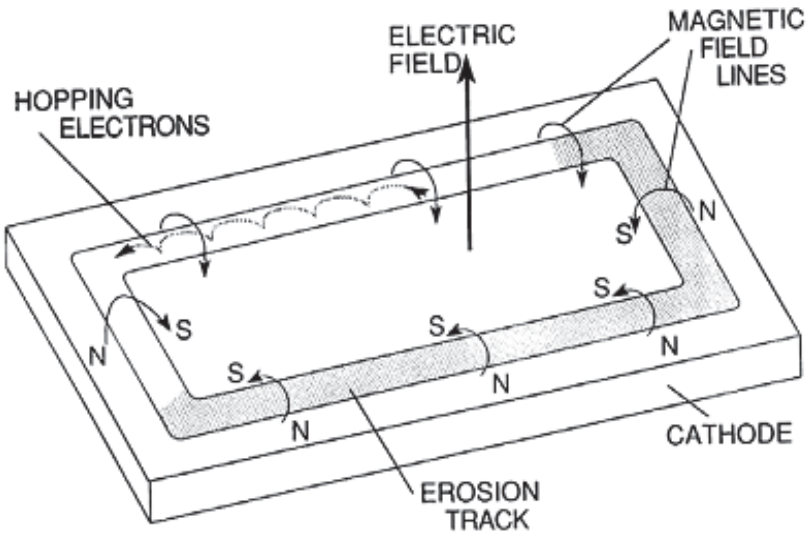

Figure 3.8. Applied field and electron motion in the planar magnetron (Ohring 2001).

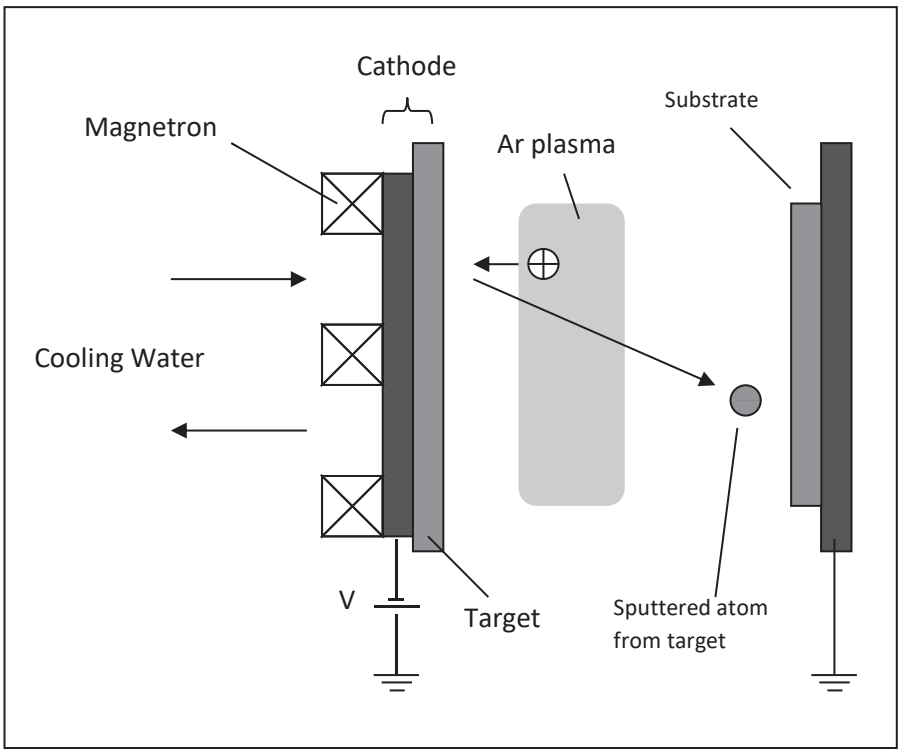

Figure 3.9. Schematics of the DC magnetron sputtering process

3.2.1. Deposition of ITO Thin Films

3.2.1.1. Borosilicate/ITO

Large area magnetron sputtering coating system was used for the deposition of ITO thin films (Tuna et al. 2010). The schematic representation of the large area magnetron sputtering coating system can be seen in Figure 3.10. In this system, movable sample holder is slowly moved under target with feedthrough system and film thickness depends on the applied power and angular velocity of the feedthrough mechanism. 3 mm thick and 50 mm x 60 mm width and length borosilicate glasses (BS) were used as a substrate to deposit ITO films on it. They were cleaned in an ultrasonic bath in the order of acetone, alcohol and de-ionized water for ten minutes in each and then the final cleaning was done by plasma etching for 10 minutes to remove organic residue. After the cleaning of the substrates, they were placed onto the sample holder (50 x 90 cm^2). To evacuate the system pressure below $3.33x10^{-6}$ mbar, we used a rough pump and a turbo molecular pump, respectively. After chamber pressure was evacuated, 26 sccm Ar and 1 sccm O_2 gases were sent into the chamber using mass flow controller, maintaining the working gas pressure of about $5.6x10^{-3}$ mbar. Then, 350 W DC power (ADL Maris, 10 kW) was applied to generate the plasma on the 50 x 20 cm^2 ITO target (purity of 99.99 % and a weight per cent of 10 to 90 for SnO_2 and In_2O_3). During the ITO thin film deposition, we moved the sample holder with 3.0 cm/min, and 256 nm thick ITO thin films were grown at the 250°C substrate temperature which was measured by a thermocouple on the sample holder. The deposition parameters can be seen in the Table 3.3.

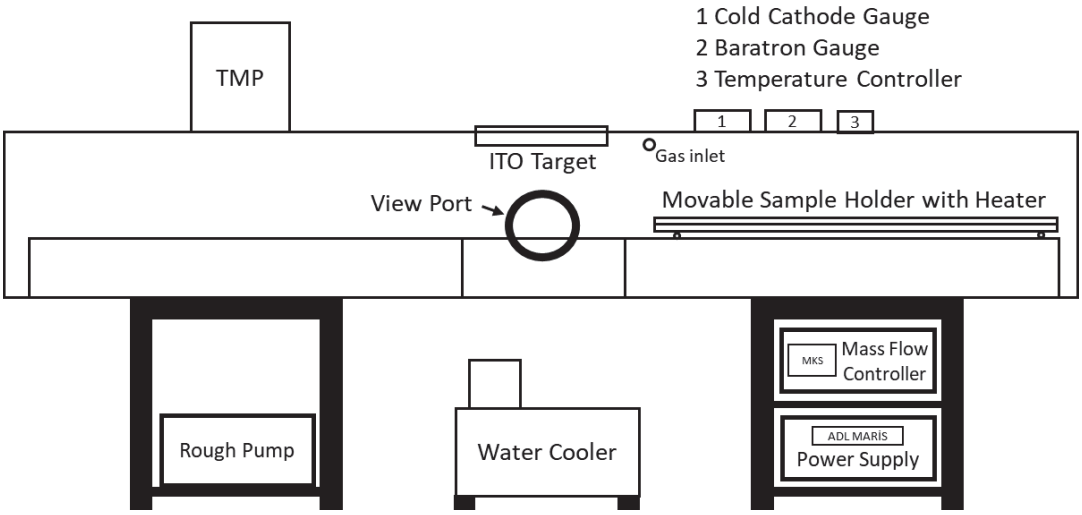

Figure 3.10. Schematic representation of large area magnetron sputtering coating system.

Table 3.3. ITO deposition parameters for the BS substrates.

Substrate	Sample	DC Power (kW)	Ar/O_2 Flow (sccm)	Holder feed through speed (cm/min)	Substrate Temperature (°C)	Thickness (nm)
BS	ITO	0.35	40/1,0	3.0	250	256

3.2.1.2. Fused Silica/ITO

Large area magnetron sputtering coating system was used for the deposition of ITO thin films on to the 2 mm thick and 27 mm x 756 mm width and length Fused Silica (FS) substrate similar with for the Borosilicate substrate, which details of the deposition given in the previous section. Some deposition parameters for the FS substrate are different compare with the BS substrate (Table 3.4.). For the FS substrate, 4 different ITO thin films were deposited. Three of them have the same deposition parameters except sample holder speed (or Thickness). Thickness of ITO A, ITO B and ITO C samples are 60 nm, 120 nm and 240 nm, respectively. For the ITO D sample with 60 nm thickness, sample holder was not heated during the deposition.

Table 3.4. ITO deposition parameters for the FS substrates.

	ITO A	ITO B	ITO C	ITO D
DC Power (kW)	1.66			
Ar/O_2 Flow (sccm)	40/2.5			
Holder feed through speed (rpm)	12000	6000	3000	12000
Substrate Temperature (°C)	250			25 (RT)
Thickness (nm)	60	120	240	60

3.2.1.3. PET/ITO

In the deposition of the ITO thin films large area roll to roll magnetron sputtering system was used. In Figure 3.11. a), the schematic representation of the large area magnetron sputtering coating system is presented. The large area magnetron sputtering system was modified with unwind and rewind rollers and a rotational feedthrough mechanism instead of linear movable sample holder with feedthrough system (Demirhan et al. 2020). By the movement of unwind and rewind rollers in the system the flexible substrate is gently moved under the target with the help of the feedthrough mechanism. The film thickness depends on the applied power and angular velocity of the feedthrough and the ITO film can be continuously deposited on large area flexible substrates. The PET substrate with the dimensions of 400 mm width, 0.075 mm thickness were installed on unwind and rewind roller thereafter put into the vacuum chamber. A rough pump backing a turbo-molecular pump is employed in order to evacuate the large area system to below 3.30×10^{-6} mbar.

Subsequently, the vacuum chamber was evacuated, high purity Ar and O_2 were introduced through independent mass flow controllers. With the purpose of investigating the influence of oxygen partial pressure, the oxygen flow rate was varied from 1.5 to 4.5 sccm while keeping the argon flow rate at 40 sccm. Afterwards, in order to generate the plasma on the 50 x 20 cm^2 ITO target (purity of 99.99% and a weight percent of 10-90 for SnO_2 and In_2O_3) 1.66 kW DC power (ADL Maris, 10 kW) was introduced. Using the rotational feedthrough, the loaded PET substrate was rolled one end to the other, ITO large area films were deposited with different Ar/O_2 ratio and roll to roll speed (18, 22, 27, 29 cm/min) for every ten meters of substrate. ITO thin films in different thicknesses were obtained by the variation of the roll-to-roll speed. The total number of samples produced is 16 (4 for each 4 set of roll-to-roll speed) and in Table 3.5, detailed sample

descriptions and the sputtering parameters employed in this investigation are presented. Using the cross-sectional SEM images, the films thicknesses were measured (Figure 3.12.).

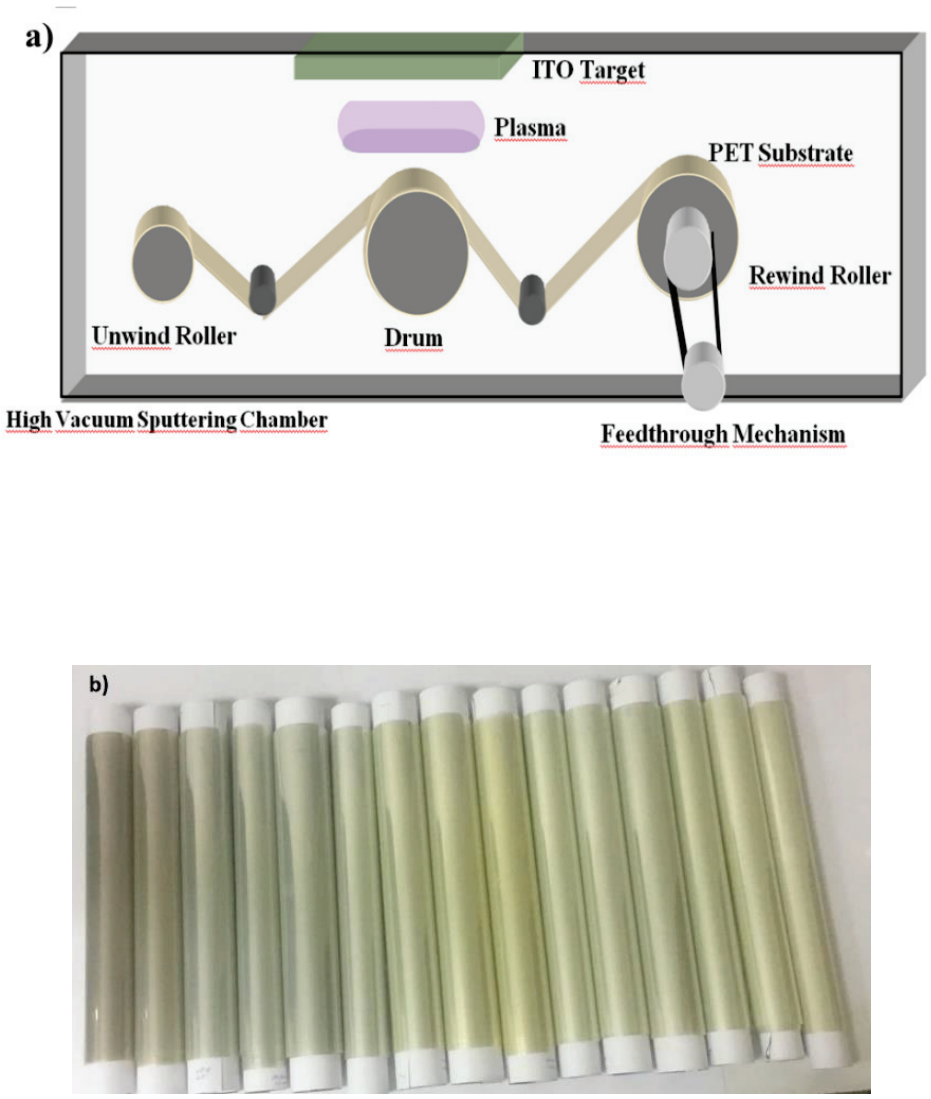

Figure 3.11. a) Schematic representation of our large area magnetron sputtering coating system, b) ITO deposited flexible Polyethylene terephthalate (PET) films (7 cm rolled, 40 cm width, 10 m long for each process parameter).

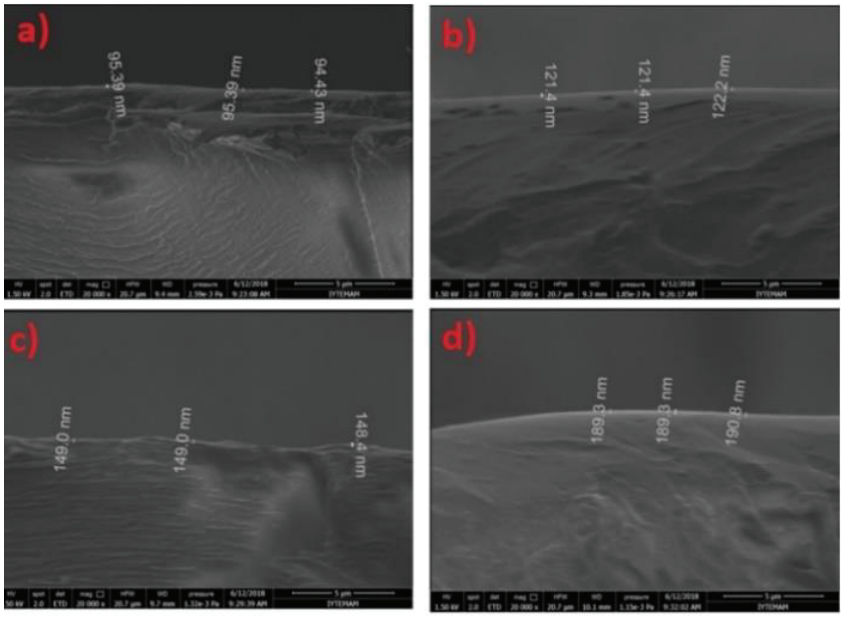

Figure 3.12. The cross-sectional SEM images of the ITO films with (a) 29 cm/min (b) 27 cm/min (c) 22 cm/min and (d) 18 cm/min roll to roll speeds (40 sccm Argon flow, 2.5 sccm oxygen flow).

Table 3.5. ITO roll to roll deposition parameters for the PET substrates.

Roll to roll speed (cm/min)	Roll to roll speed (RPM)	Argon/Oxygen Flow (sccm)	DC Power (kW)	Thickness (nm)
18	250	40/1.5	1.66	190
18	250	40/2.5	1.66	190
18	250	40/3.5	1.66	190
18	250	40/4.5	1.66	190
22	300	40/1.5	1.66	150
22	300	40/2.5	1.66	150
22	300	40/3.5	1.66	150
22	300	40/4.5	1.66	150
27	350	40/1.5	1.66	120
27	350	40/2.5	1.66	120
27	350	40/3.5	1.66	120
27	350	40/4.5	1.66	120
29	400	40/1.5	1.66	90
29	400	40/2.5	1.66	90
29	400	40/3.5	1.66	90
29	400	40/4.5	1.66	90

3.3. Electro Annealing Process

Annealing of ITO thin films produced by magnetron sputtering is to achieve the desired structure and properties of the films for practical applications (Tuna et al. 2010). The most common method for the annealing of transparent conductive oxides is thermal annealing (Kerkache et al. 2005). As an alternative, the recent studies have reported that the performance of deposited ITO films can be improved by electro-annealing which is a process of self-heating by electric current (Rogozin et al. 2006, Pei et al. 2009, Lee et al. 2008). Electro-annealing offers many advantages, i.e. no external heater is required during annealing and the direct Joule heat generated by applying an electric field to the film leads to a decrement both in impurity generation and the heat overloading by the surrounding components (Rogozin et al. 2006). Moreover, electro-annealing is suitable for thermally sensitive substrates (Rogozin et al. 2006), because, in the case of electro-annealing, the crystallization sets on and proceeds faster at lower power levels in contrast to thermal annealing due to efficient energy coupling results from Joule heating. In order to develop a clear understanding about the characteristics of ITO thin films under electrical current is crucial to eliminate the life-time effects of electronic devices. However, there is little research concerned with the investigation of the influence of electro-annealing on the properties of ITO films by passing electric current flow through them in air and vacuum (Rogozin et al. 2006, Pei et al. 2009, Lee et al. 2008). In previous studies, Rogozin et al. 2006 (Rogozin et al. 2006) proposed a method which provides constant power at variable film resistance and pointed out that electro-annealing in vacuum provides reduction in thermal budget and decrease in the kinetic exponent of crystallization in comparison with the thermal annealing. Lee et al. 2008 (Lee et al. 2008) observed that optical and electrical properties of ITO films on polyimide substrate improve by electro-annealing in air. In a recent study, Pei et al. 2009 (Pei et al. 2009) investigated the effect of electro-annealing in air on the optical and electrical properties of ITO films, and they concluded that the electric power is a decisive factor that determines performance of the films. We investigate here a study of the effect of electro-annealing in both air and vacuum on structural, optical and electrical properties of ITO thin films grown by DC magnetron sputtering using borosilicate glass substrate (Koseoglu et al. 2015). In contrast the previous researches, large area substrates were used to investigate the effect of high electrical current on ITO thin films in large scale

applications. Moreover, in the view of the results of the electro-annealing of BS/ITO samples (Koseoglu et al. 2015), at low temperature electro-annealing of ITO films in the air ambient decrease the R_s values of ITO thin films. Therefore, for the FS/ITO samples, electro-annealing was performed in the air ambient at 100°C during 20 minutes. The details of the electro-annealing of the FS/ITO thin films will be given in the further sections.

3.3.1. Electro-Annealing of Borosilicate/ITO

The schematic representation of the electro-annealing process on ITO thin films can be seen in Figure 3.13. 1 μm thick, 5 mm wide and 60 mm length of copper plates were attached to the two opposite edges of the substrates in order to apply constant current. After the deposition of the ITO thin films onto the borosilicate glasses, electro-annealing was performed by applying 0.75, 1.00, 1.25 and 1.50 A constant ac currents to the ITO thin films in vacuum (< 6.6 $x10^{-6}$ mbar) and air for 10 minutes. ITO thin film temperature increased during electro-annealing for 10 minutes and then naturally decreased to the room temperature within between 20 and 40 minutes without annealing currents.

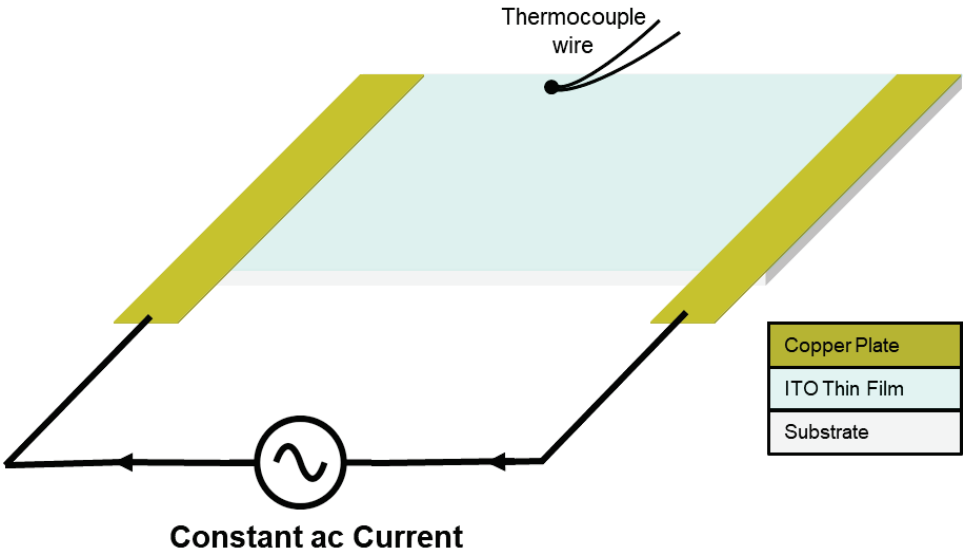

Figure 3.13. Schematic representation of Electro-annealing process on ITO thin films

Due to the Joule heating, the temperature of the ITO thin films increases as the electrical current passes through the films. The variation of the temperature versus time of electro-annealed thin films in air and vacuum are shown in Figure 3.14. Sample temperature increased during 10 min and then slowly decreased to the room temperature within 20 and 40 min. The highest temperatures for electro-annealed ITO thin films at the end of the 10 minutes in air and vacuum were about 98, 124, 229, 327°C and 160, 218, 292, 319°C when currents were 0.75, 1.00, 1.25, 1.50 A, respectively. Due to the heat balance between heat input and heat loss, the temperature of the films during electro-annealing in vacuum was higher as compared to electro-annealing in air for the same current input. In our set up, heat input, radiation and conductance terms of heat loss were approximately the same for electro-annealing in vacuum and in air. However, only the convection term of heat loss was noticeably higher for electro-annealing in air, and this loss caused lower temperature of the films during electro-annealing in air.

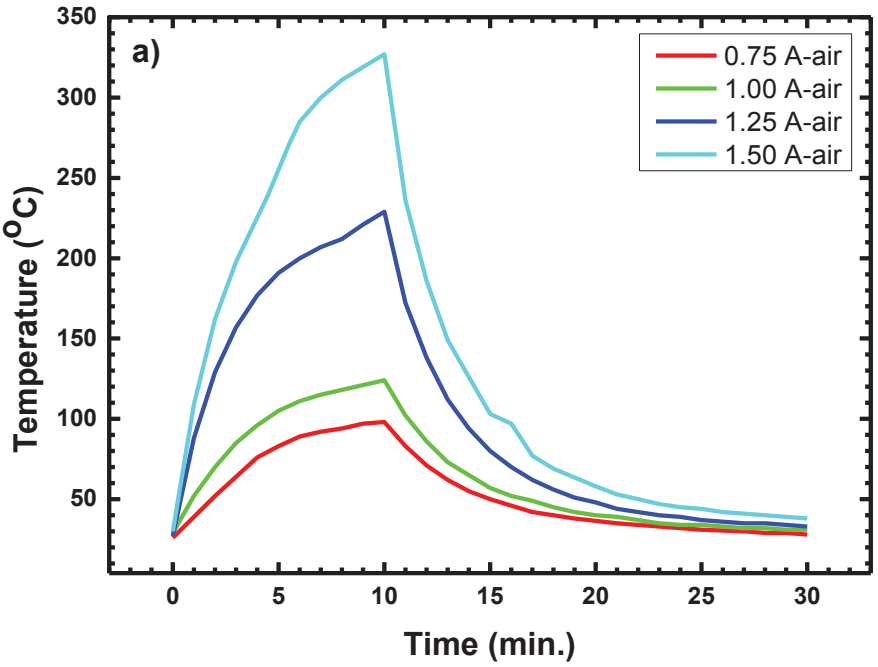

Figure 3.14. The variation of temperature versus time of electro-annealed ITO thin films in a) air and b) vacuum

(cont. on next page)

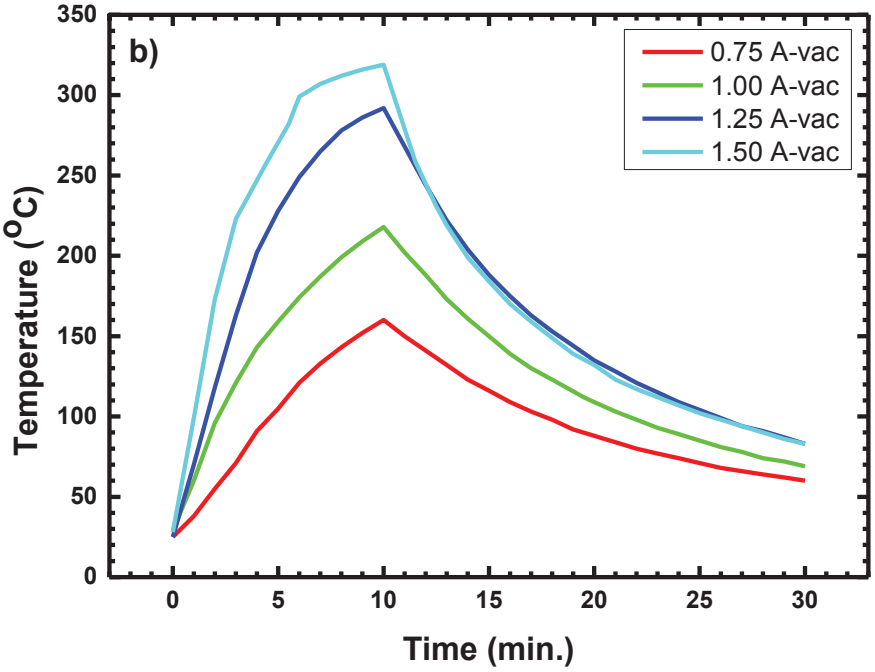

Figure 4.10. (cont.)

3.3.2. Electro-Annealing of Fused Silica/ITO

The schematic representation of the electro-annealing process on FS/ITO thin films is similar with BS/ITO thin films as it can be seen in Figure. 3.13. After the deposition of the ITO thin films onto the Fused Silica, FS/ITO thin films were cut in the 20 x 15 mm^2 dimension and 1 μm thick, 2.5 mm wide and 30 mm length of copper plates were attached to the two opposite edges of the substrates in order to apply current. Electro-annealing was performed by applying ac voltage (applied voltages are varying between 20-30 V for the samples) to the ITO thin films in air for 20 minutes at the 100°C.

For the electro-annealing of FS/ITO samples we performed 3 types of process;

- In the first one, named EA1, Thin films were heated up to 100°C and kept the temperature at 100°C for 20 minutes by temperature controller. During EA1, the applied voltage was disconnected by the switch in the Temperature controller. The temperature variation during the on-off of the voltage are 100 ± 2°C.
- In the second one, named EA2, thin films were heated up to 100°C and kept the temperature at 100°C for 20 minutes by increase/decrease the applied voltage

manually. During EA2, the applied voltage continuously flows and the applied voltage variation are between 20 - 25 ± 1 V.

- In the third one, named EA3, the electro-annealing process is the same with the electro-annealing process of EA2. However, there is only one difference, which is that, thin films were heated up to 200°C for 20 minutes.

3.4. Characterization Techniques for the Growth Thin Films

This section gives an overview of the techniques used to characterize the ITO thin films grown by magnetron sputtering. In the beginning of the characterization of the thin films, the thickness of the thin films was measured by profilometer. After that, electrical and optical properties were investigated for the growth thin films. Then, Structural properties were determined using XRD techniques. Finally, THz transmission spectrum analysis of the films were performed using the THz imaging system.

3.4.1. Surface Profilometer

Thin film thicknesses were determined using A Veeco DEKTAK 150 profilometer. A stylus tip moves on the surface and thickness of the samples are determined by measuring the vertical movements of stylus and fitting with respect to starting level of the stylus.

3.4.2. Electrical Properties

Electrical characteristics of ITO thin films were investigated to determine sheet resistance (R_s) of the films by four-point probe technique using Keithley 2224 source meter.

3.4.3. Structural Properties

The X-Ray Diffraction method (XRD) is based on the diffraction of X-rays in a characteristic order, depending on the atomic sequences of each crystal phase. These

diffraction profiles for each crystal phase define that crystal like a fingerprint. The X-Ray Diffraction analysis method does not destroy the sample during analysis and enables the analysis of even small amounts of samples. A beam of incident X-rays diffract into many specific directions, and constructive interference occurs when Bragg's Law is satisfied and structure of the materials can be determined by analyzing the 2θ angles and intensities of these diffracted beams.

XRD was performed in order to determine the crystal structures of the thin films. The XRD was operated in the Bragg-Brentano focusing geometry on a Philips X'Pert Pro X-Ray diffractometry, with Cu Kα radiation (λ=1.5406 Å). XRD patterns were recorded from 2θ = 10-70° with step size of 0.013° within 25 minutes for all samples.

3.4.4. Optical Properties

Spectrophotometry is widely used for the measurements of reflection or transmission properties of a materials as a function of wavelength. Optical properties of all thin films were investigated by measuring the transmission from 2600 to 200 nm wavelength, using a Perkin Elmer Lambda 950 UV/VIS/NIR spectrophotometer.

3.4.5. THz Characterization of Thin Films

The THz wave, emitted from WR1.5 AMC, was first modulated by a function generator with 15 Hz frequency and 2.5 V peak to peak voltage using the TTL modulation option of the WR1.5 AMC, and then collimated by a pair of 90° off-axis parabolic mirrors and focused into the sample holder origin. After the interaction of the THz waves and sample the transmitted THz wave was collimated by a second pair of 90° off-axis parabolic mirrors and focused into the Golay Cell. Finally, the collected signals by the Golay Cell were analyzed by a lock-in amplifier.

In order to get, THz transmission spectrum of the samples in the 0.500 to 0.750 THz frequency range, the sample (background (air or free space), substrate, thin film deposited on the substrate and metal) was fixed to the focal point of the sample holder and then the transmitted THz wave collected by the lock-in amplifier in the 0.500 to 0.750 THz frequency range with the 0,0025 THz (2.5 GHz) resolution. After that, THz transmittance (% T_{THz}) of thin films can be calculated by the following formula;

$$\%T_{THz}(\nu) = \frac{(S(\nu)-N(\nu))}{(B(\nu)-N(\nu))} \quad (3.1)$$

here, S(ν), B(ν) and N(ν) is the THz transmission spectrum collected by the lock-in amplifier in the 0.500 to 0.750 THz frequency range of the thin film deposited on the substrate, background (air or free space) and metal, respectively. THz transmission spectrum of the substrate were taken to normalize the thin film THz spectrum with respect to the background.

CHAPTER 4

RESULTS AND DISCUSSION

4.1. CW THz Images

Figure 4.1. shows the THz image of the copper sample holder rod and the hole in the sample holder. Where there is metal, the transmission drops to zero. The reason why there is no sharp increase at the edges of copper, that is, during the transition of THz from metal to air, is due to the spot size of the THz wave. If we increase the THz frequency, the spot size will grow, and this transition will grow. The Terahertz image in Figure 4.1. a) shows the hole on the copper bar. Figure 4.1. b) shows the Terahertz image of the copper bar. It is also seen in the transition in the signal.

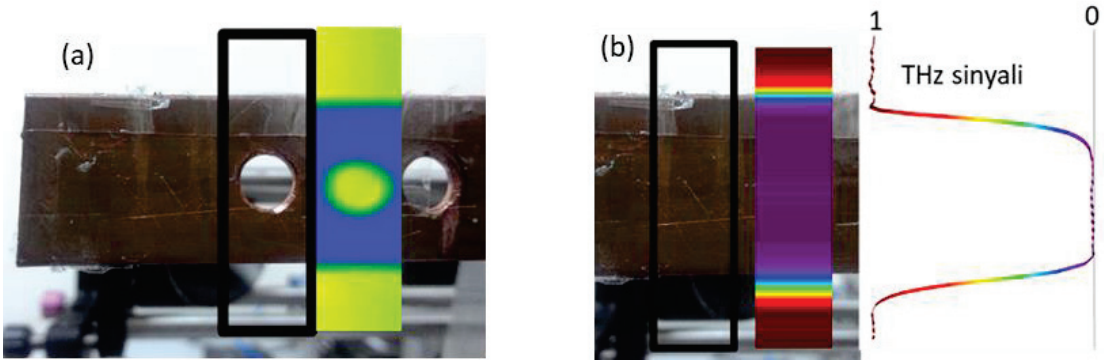

Figure 4.1. THz image of a) hole in copper sample holder and b) sample holder

In Figure 4.2., two different samples were prepared for THz scanning. Both have a scalpel blade and paper clip tip. One has an extra screw and plastic piece (Figure 4.2. a)) on the thin cardboard paper, while the other has a star-shaped pendant and capacitor (Figure 4.2. b)) on the hard plastic. The frequency of the imaging is 0,537 and 0,600 THz for the Figure 4.2. a) and Figure 4.2. b), respectively. In Figure 4.2., the boundaries of the parts are well determined and the increase in the size of the spot can be seen in the image taken in Figure 4.2. b).

Figure 4.2. Terahertz images taken at a) 0.537 THz b) 0.600 THz.

Figure 4.3. shows a THz transmission and visible image of a leaf at 0.537 THz frequency. An area 60 mm × 40 mm was scanned at 1 mm resolution. The leaf image demonstrates one of the key THz features, its sensitivity to water, with higher water content leaf veins showing higher attenuation.

Figure 4.3. a) THz transmission at 0,537 THz and b) visible image of a leaf.

4.2. Characterization of ITO Thin Films

4.2.1. Borosilicate/ITO

4.2.1.1. Electrical Properties

Sheet resistance (R_s) of as grown and electro-annealed ITO films in air and vacuum are shown in Figure 4.4. The sheet resistance of the ITO thin films strongly related to the amount of oxygen vacancies and microstructure (Hsu et al. 2009). The

oxygen vacancies create maximum two free electrons per vacancy to the donor level through ionization, leading to an increase in conductivity. For the electro-annealing in vacuum, the R_s of the films decreased with increasing currents due to an increase of the temperature by electro-annealing. The decrease in R_s can be attributed to the improvement in the crystallinity and enhancement of oxygen vacancies which results from releasing of some oxygen atoms from the surface of ITO thin films and the absence of free oxygen in vacuum. In comparison with the electro-annealed ITO films in vacuum, the sheet resistances of the electro-annealed ITO films in air are higher due to the reaction of free oxygen in ambient with the ITO films and less crystallization. For the electro-annealing in air, the R_s of the films decreased up to 1.00 A since the lower temperature of the film increases the interaction of oxygen atoms with In atoms and In_2O_{3-x} phase is formed (Pei et al. 2009). This formation results in the intensification of the oxygen vacancy concentration and decrease of the R_s. For the higher current values, high temperature results in interaction of the residual oxygen atoms inside the film or on the top surface with In atoms and In_2O_{3-x} phase, after that In_2O_3 phase is formed. This formation reduces oxygen vacancy concentration and increases R_s (Pei et al. 2009).

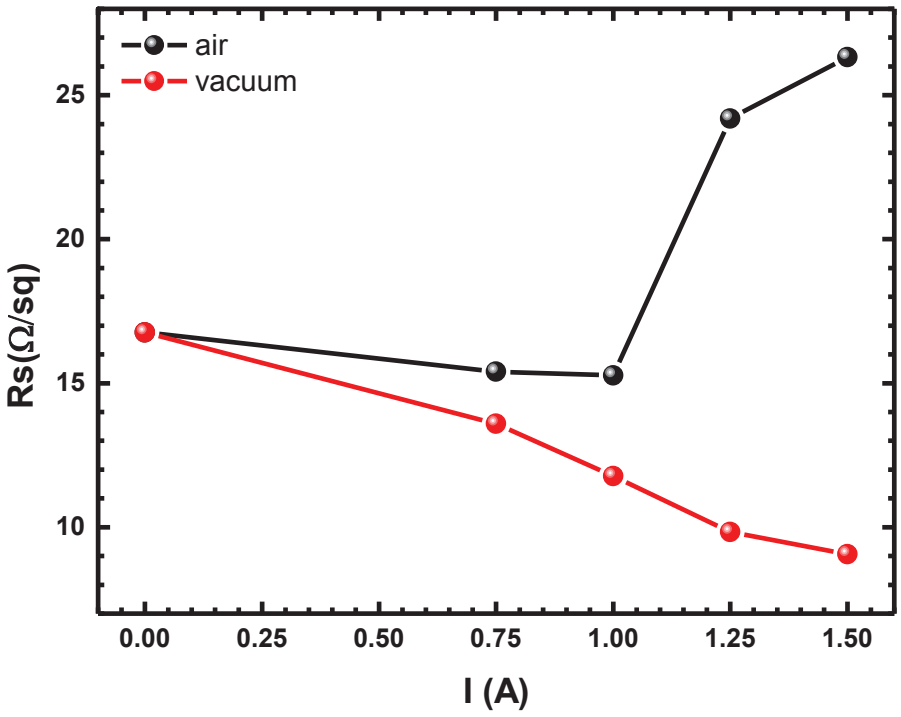

Figure 4.4. Sheet resistance of electro-annealed ITO thin films in air and vacuum with applied currents.

4.2.1.2. Structural Analysis

X-ray diffractometer (XRD) is used to analyze the effect of electro-annealing on the crystal structure of ITO thin films. Figure 4.5. shows XRD patterns of the as grown (deposited at 250°C) and ITO thin films electro-annealed at 0.75, 1.00, 1.25 and 1.50 A in air and vacuum. It should be noted that the broad hump between 20 and 30° (2θ), which occurs due to background from the borosilicate glass substrate, was extracted from the XRD graphs. The XRD patterns, which consist of the (211), (222), (400), (411), (431), (440) and (622) peaks, of all the films indicate a cubic In_2O_3 phase. None of the spectra revealed any characteristic peaks of Sn, SnO, or SnO_2 due to complete miscibility of tin atoms into the In_2O_3 lattice. It was observed that all ITO thin films are crystalline and have strong (222) and (400) peaks showing preferred orientations. Appearing the strong (222) and (400) peaks prominently indicate the coexistence of <100> and <111> textures. For all of the electro-annealed ITO thin films, it can be clearly seen that the crystallinity of the films improves by increasing electro-annealing currents. Moreover, crystalline structures become more perfect for the ITO thin films electro-annealed in vacuum. This improvement can be clearly seen in Figure 4.6. which shows (222) and (400) reflections in detail for the sample electro-annealed in vacuum and in air at 1.5 A. (222) preferred plane is a close-packed plane in the In_2O_3 body-centered cubic structure and does not accommodate vacancies very well. Unlike (222) preferred plane, (400) plane accommodates the oxygen vacancies on the planes. Therefore, the sheet resistance of the ITO films depends upon the orientation of (400) plane rather than that of (222) plane. As it can be seen in Figure 4.5. and Figure 4.6., ITO thin films electro-annealed in vacuum are more oriented along (400) plane at the same current. This orientation also explains why the sheet resistance of the ITO thin films electro-annealed in vacuum is lower than that of the electro-annealed in air ones.

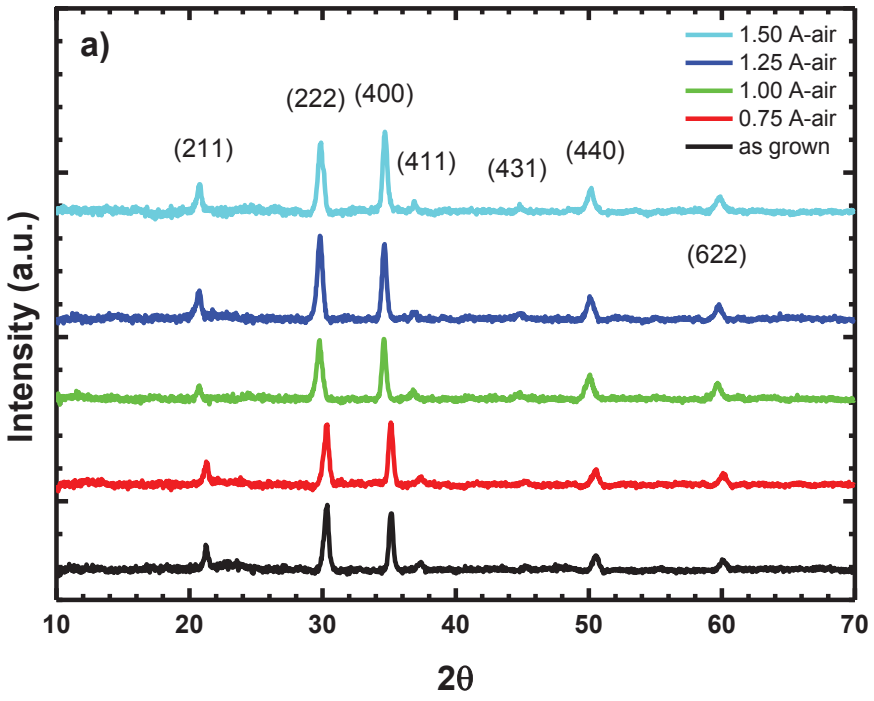

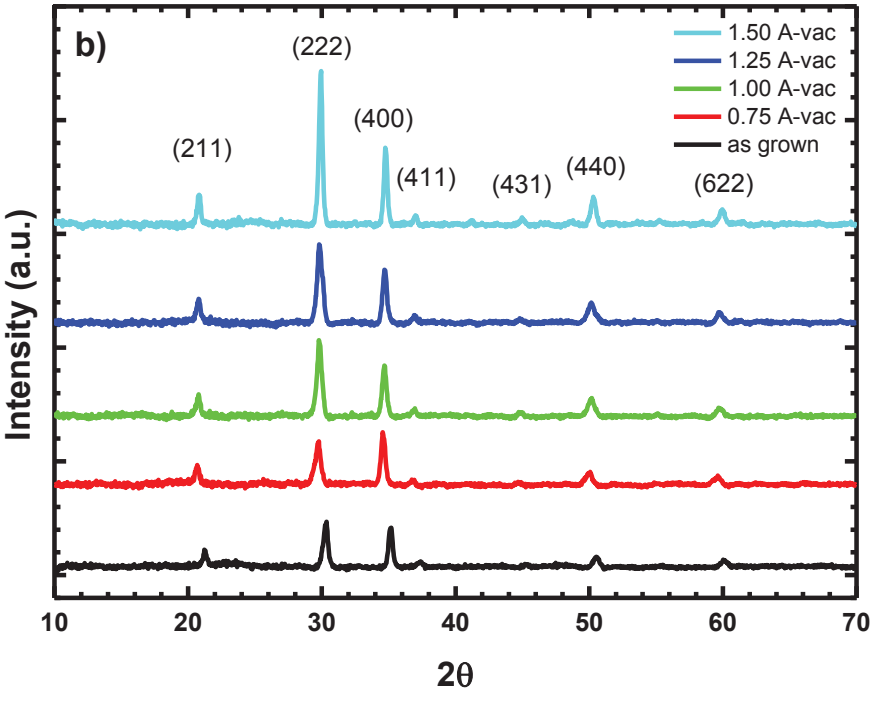

Figure 4.5. XRD patterns of the as grown ITO thin films and electro-annealed ITO thin films in a) air and b) vacuum.

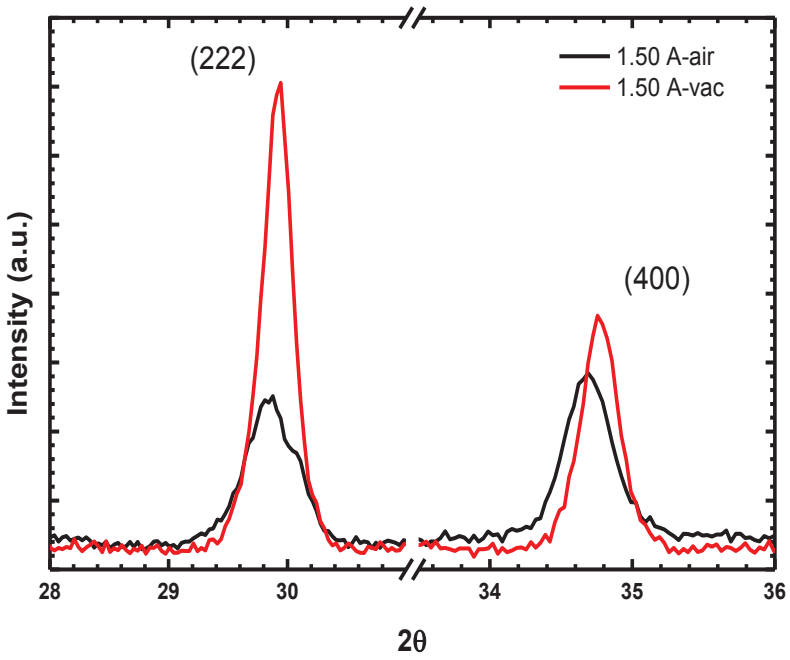

Figure 4.6. Detail view of (222) and (400) reflections for the sample electro-annealed in vacuum and air at 1.5 A.

4.2.1.3. Transmission Analysis

Figure 4.7. shows the transmittance spectra as a function of wavelength in the range of 200-2600 nm for the as grown and the electro-annealed ITO thin films at different currents in air and vacuum, respectively. It clearly shows that the electro-annealing process enhances the transmittance of films in the visible region. In the visible light region, the average transmittance between 400 nm and 800 nm (including borosilicate glass substrate) is about 73% for the as grown ITO thin films and it increases up to 82% both for electro-annealing in vacuum and air (Table 4.1.). Moreover, average transmittance increases by increasing currents values. Such an increase implies that the optical properties of the films improve due to the improvement of structural homogeneity of the films and the decrease of light reflection. In the near infrared region, the concentration of free carriers becomes important for the optical transmittance of the ITO films (Hu et al. 2004). From Figure 4.4., we observed that there exists a correlation between the NIR transmittance and R_s of the films for both electro-annealing in air and vacuum. Lower resistivity values result from higher concentration of free carriers that cause higher reflection or lower transmission of the infrared region.

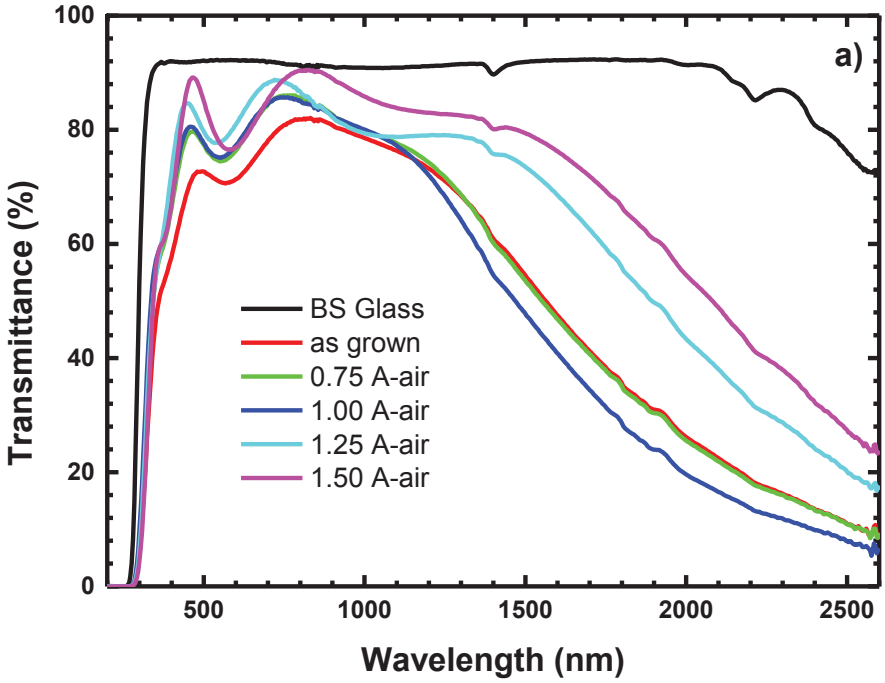

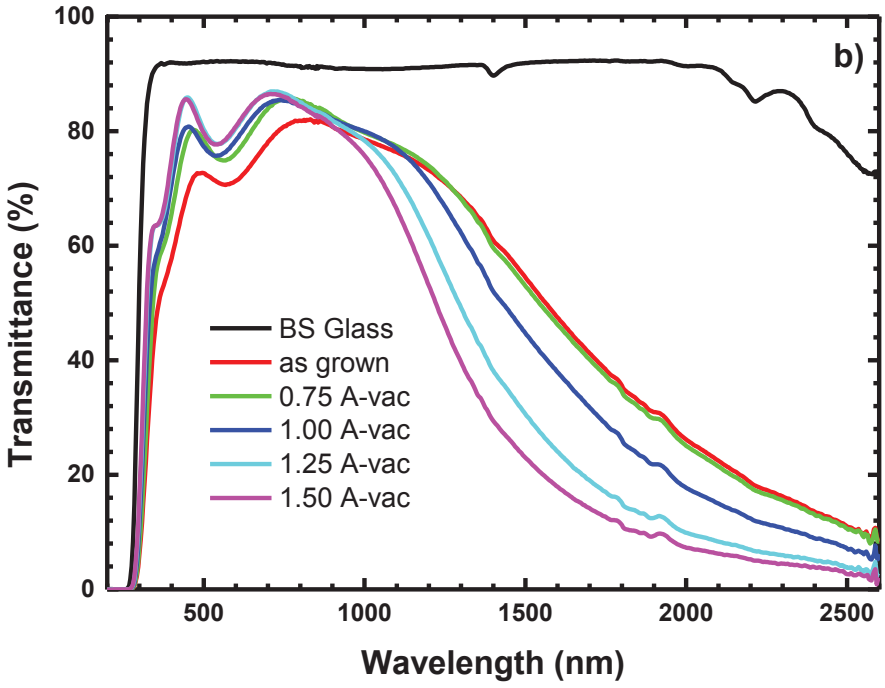

Figure 4.7. Transmittance spectra as a function of wavelength in the range of 200-2600 nm for the as grown and electro-annealed ITO films in a) air and b) vacuum.

In the present study, the absorption coefficient, α^2 versus photon energy (hν) plot was used to estimate the bandgap energy of the ITO thin films (Figure 4.8.). Absorption was calculated by the following equation (Lee and Park 2004, Sanon, Rup, and Mansingh 1991)

$$T - R = e^{-\alpha t} \tag{4.1}$$

where T and R denote the transmittance and reflectance, respectively, and t is the thickness of the film. The reflectance of the films was neglected due to its relatively low value (Lee and Park 2004, Zhang et al. 2000), and then the absorption coefficient was simplified as

$$\alpha^2 = \frac{(InT)^2}{t^2} \tag{4.2}$$

Since indium oxide has a direct transition, i.e. $\alpha h\nu = A(h\nu - E_g)^{1/2}$, the bandgaps of the films are deduced from the extrapolation of the linear plots of α^2 versus photon energy (hν).

The direct optical band gap values of the electro annealed ITO thin films in air and vacuum can be seen in Table 4.1. The electronic gap values obtained from the fit of the curves is slightly higher for the samples annealed in vacuum compared to the samples annealed in air for the same current inputs. This difference may be due to the higher carrier concentrations in vacuum electro-annealed samples. We observed that there is a correlation between the bandgap and Rs for all of the electro-annealed thin films, i.e., while the resistivity decreases, the bandgap increases with respect to the increased annealing current. The increase in the bandgap may be due to an increase in the carrier concentrations. This bandgap widening can be explained on the basis of the Burstein-Moss shift. However, at very high carrier concentrations, there may be band gap narrowing due to the electron-electron and electron-impurity scattering.

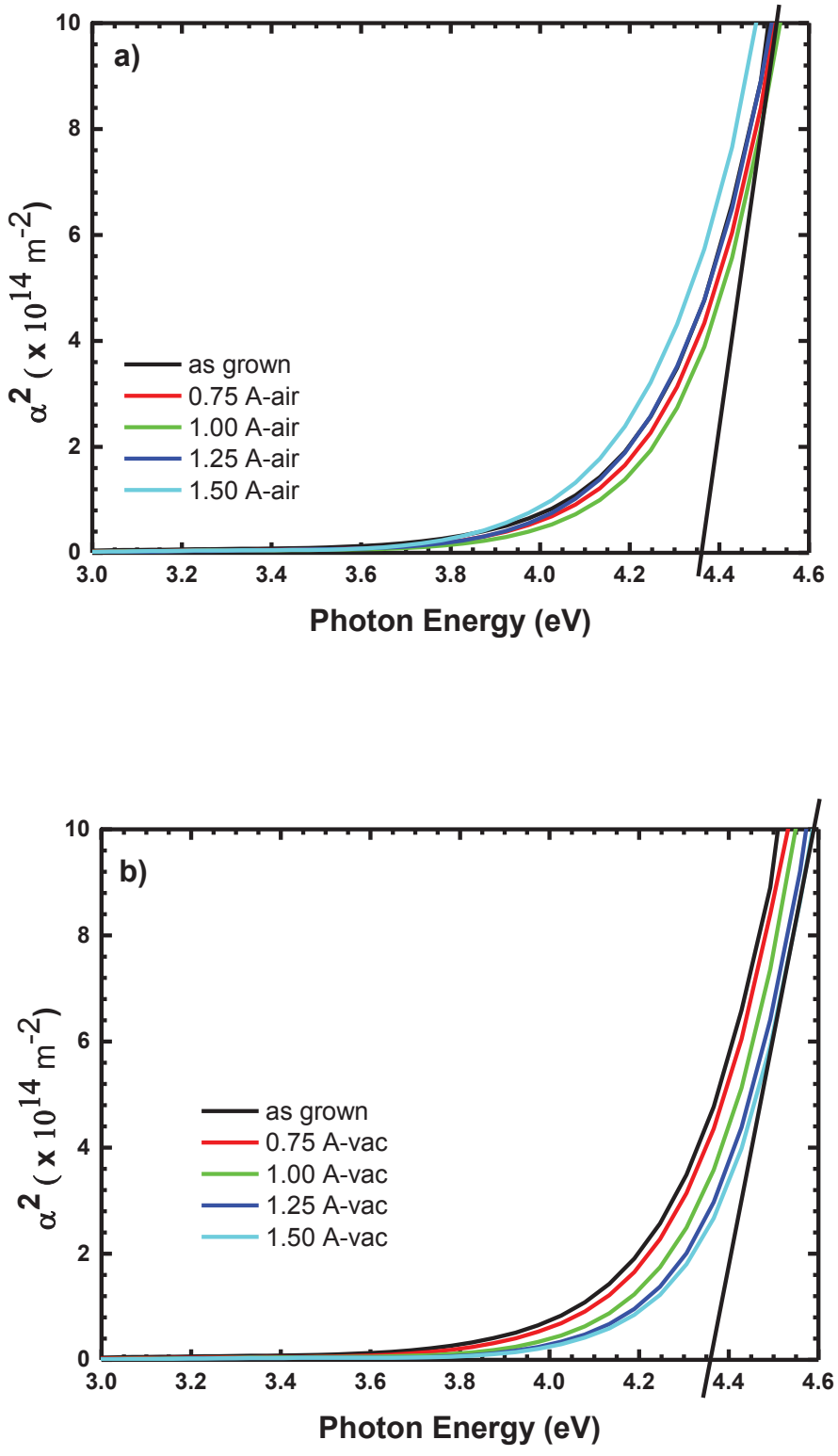

Figure 4.8. α^2 versus Photon Energy (hν) curve for the as grown and electro-annealed ITO films in a) air and b) vacuum.

Table 4.1. Transmission, R_s and E_g results of the electro-annealed ITO thin films.

	Transmission (%)		R_s (Ω/□)		E_g (eV)	
I (A)	**air**	**vacuum**	**air**	**vacuum**	**air**	**vacuum**
0.00	73.497	73.497	16.761	16.761	4.280 (± 0.027)	4.280 (± 0.027)
0.75	79.471	79.355	15.402	13.590	4.288 (± 0.019)	4.293 (± 0.018)
1.00	79.976	80.486	15.266	11.778	4.293 (± 0.023)	4.333 (± 0.015)
1.25	83.350	82.931	24.190	09.830	4.262 (± 0.021)	4.351 (± 0.031)
1.50	82.744	82.799	26.319	09.060	4.235 (± 0.022)	4.373 (± 0.013)

4.2.2. Fused Silica/ITO

4.2.2.1. Electrical Properties

Figure 4.9. shows the variation graph of R_s values of the as grown and electro-annealed ITO thin films. Moreover, exact values of the R_s values can be seen in the Table 4.2. The electro-annealing process for the FS/ITO thin films is described in the experimental section. Due to the decrease in the R_s at low temperature electro-annealing in the BS/ITO samples in the air (up to 1.00 A electro-annealing), we prefer to perform the electro-annealing of FS/ITO thin films at 100°C with 20 min duration at that temperature (except EA3, which performed at 200°C with 20 min duration for cooperation.).

For the ITO samples, when we compare the electro-annealing process of the films, R_s values decrease in the order of as-grown, EA1 and EA2, respectively. However, for the ITO B samples, R_s values of EA2 higher than EA1 with small difference. For the EA3 process of ITO A, the R_s value of the films increase compare with the other samples due to the high temperature (200°C) with respect to 100°C. ITO D thin films were grown at room temperature during the deposition and they have amorphous crystal structure (note: it can be seen in the next section). Therefore, the difference between the R_s values of the as grown and electro annealing processes has bigger than others. Moreover, if we compare the EA1 and EA2 process, EA2 has the lower R_s value, Because, there exist applied voltage during the whole 20 minutes EA2 electro-annealing process.

Due to the low temperature (100°C) during the electro-annealing process, the interaction of oxygen atoms with In atoms increase and In_2O_{3-x} phase is formed. This formation results in the intensification of the oxygen vacancy concentration and decrease

of the R_s. However, High temperature (200°C) with respect to 100°C results in interaction of the residual oxygen atoms inside the film or on the top surface with In atoms and In_2O_{3-x} phase, after that In_2O_3 phase is formed. This formation reduces oxygen vacancy concentration and increases R_s.

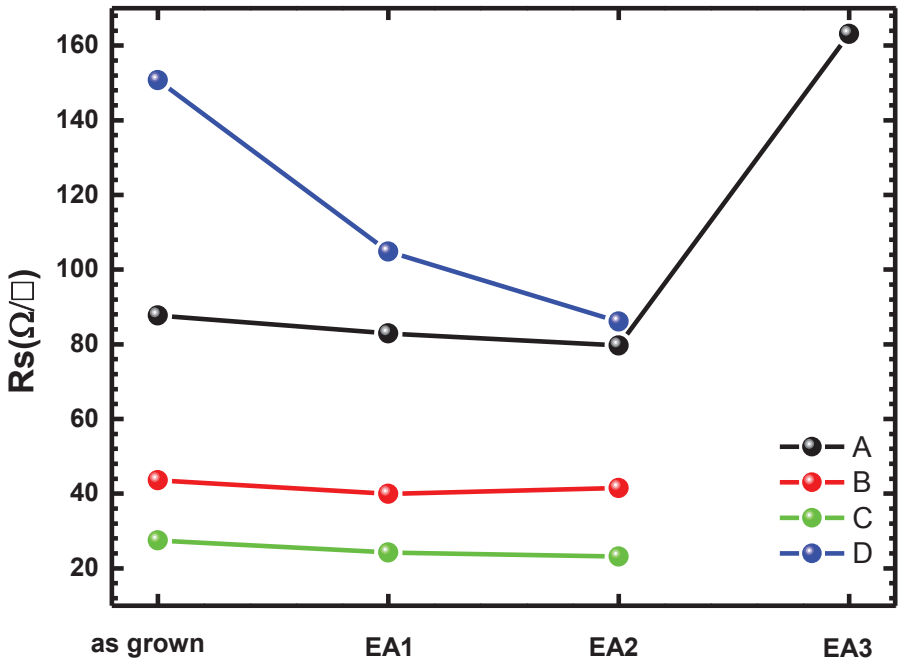

Figure 4.9. Variation graph of R_s values of the as grown and electro-annealed ITO thin films.

Table 4.2. R_s values of the as grown and electro-annealed ITO thin films.

	ITO A	ITO B	ITO C	ITO D
Rs (as grown) (Ω/□)	87.7	43.6	27.5	150.8
Rs (EA1) (Ω/□)	82.9	40.0	24.3	104.9
Rs (EA2) (Ω/□)	79.7	41.5	23.2	86.1
Rs (EA3) (Ω/□)	163.1	-	-	

4.2.2.2. Structural Analysis

Figure 4.10. shows XRD patterns of the as grown and electro-annealed ITO thin films. We observed Cubic In_2O_3, Sn and SnO peaks. (hkl) of the peaks are labeled in the

XRD graph from the analysis of XRD patterns of the thin films by the High Score Plus program.

If we look at the as grown thin films from ITO A to ITO C, we can see that intensity of the (400), (411) and (440) peaks increase with increase of the thin film thicknesses. For the ITO D thin film, the deposition was performed without heating during the magnetron sputtering different from the others. Therefore, it has amorphous structure.

If we compare the as grown and electro-annealing processes (EA1, EA2 and EA3), for the ITO A, intensity of (411) peak increase more in the EA2 process than the others. Moreover, if we look at the EA3 process, extra peaks appear especially around 68° (2θ) and the intensity of the Sn (111) peak can be seen clearly around 21.2° (2θ). This can be the reason of the increase in the R_s of the ITO A thin film in the EA3 process that is also stated in the previous section this increment results from the reduction in the oxygen vacancy concentration.

For the ITO B thin films there is a small increase in the intensity of the peaks as a result from the electro-annealing. Intensity of (400) peak of the ITO B-EA2 is higher than ITO B-EA1 and Intensity of (222) peak of the ITO B-EA1 is higher than ITO B-EA2. This can be the reason of the a little higher R_s values of the ITO B-EA2 than ITO B-EA1.

For the ITO C thin films, there is no distinct difference in the XRD patterns.

For the ITO D thin films, due to the amorphous structure of the as grown films, crystallinity of the thin films enhanced with EA1 and EA2 electro-annealing processes. However, it can be understood by looking at the (400) peak, the crystallinity of the films much more increase by the EA2 process than EA1 process. That's the reason of the decrements in the Rs values by the enhancing the crystallinity of the thin films.

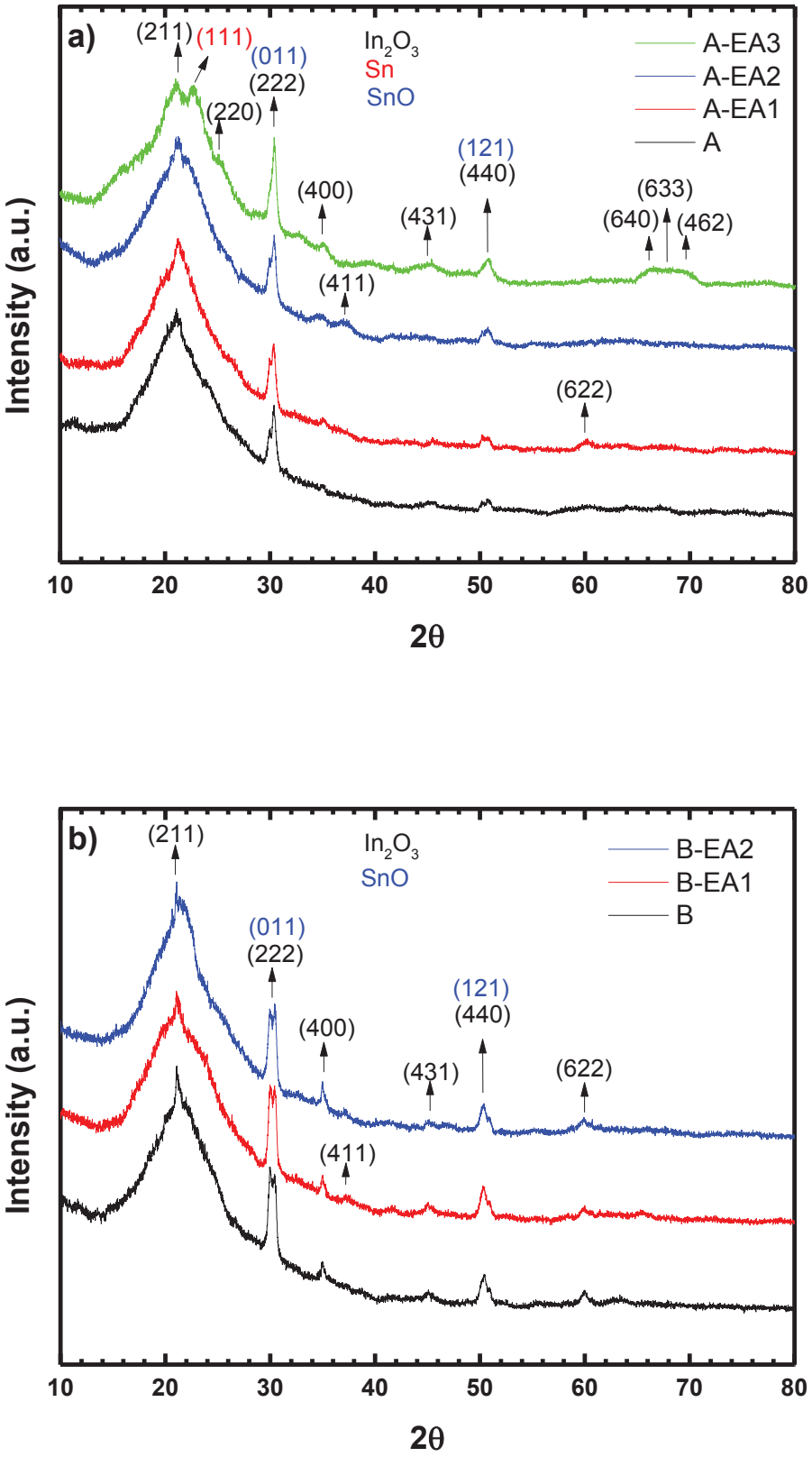

Figure 4.10. XRD patterns of the as grown and electro-annealed ITO thin films.

(cont. on next page)

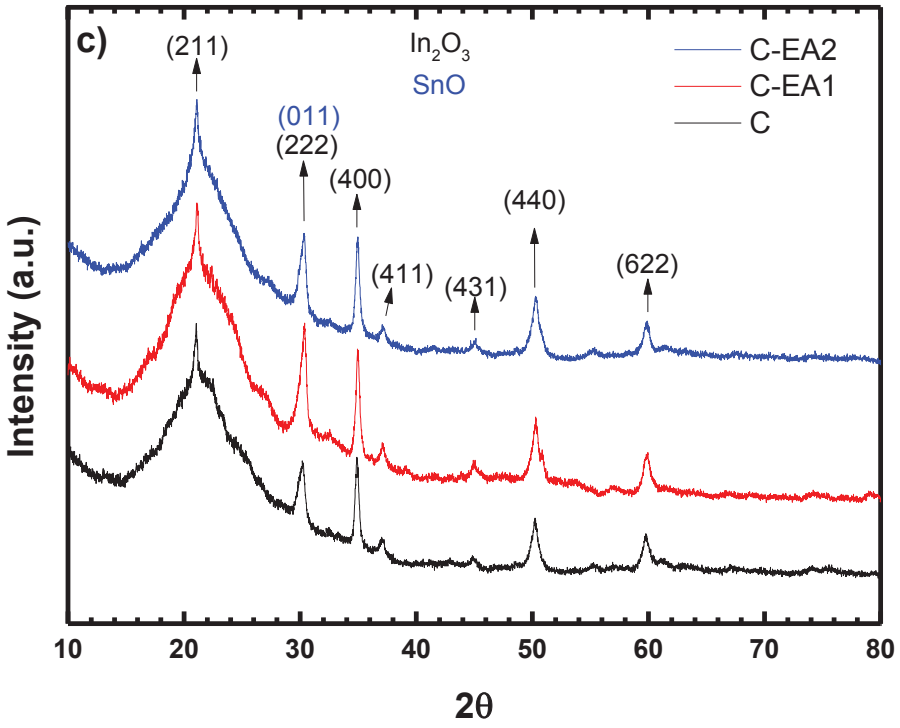

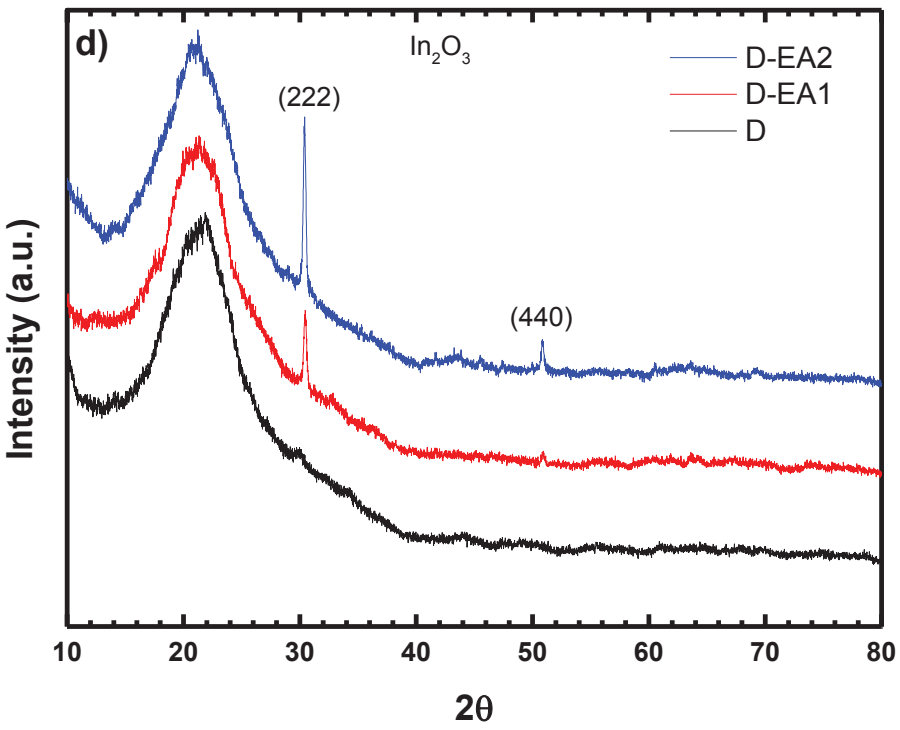

Figure 4.10. (cont.)

(cont. on next page)

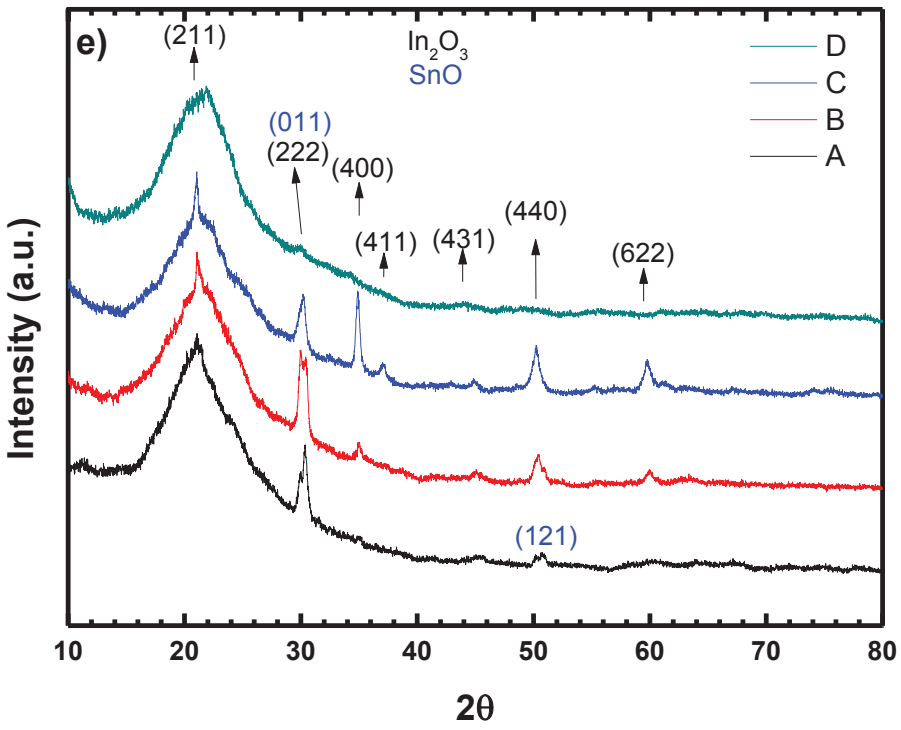

Figure 4.10. (cont.)

4.2.2.3. Transmission Analysis

Figure 4.11. shows the transmittance spectra as a function of wavelength in the range of 200-2600 nm for the as grown and the electro-annealed ITO thin films grown on the fused silica substrate. It shows that the electro-annealing process enhances the transmittance of films in the visible region.

For the ITO A, ITO C and ITO D thin films, In the visible light region, the transmittance at 550 nm (including fused silica substrate) increases for the EA1 and EA2 electro-annealing process and decreased for the EA3 electro-annealing process (Table 4.3.). The change in the transmission is very small similar with R_s and the variation of transmittance vs EA processes is shown in Figure 4.12. Such an increase implies that the optical properties of the films improve due to the improvement of structural homogeneity of the films and the decrease of light reflection.

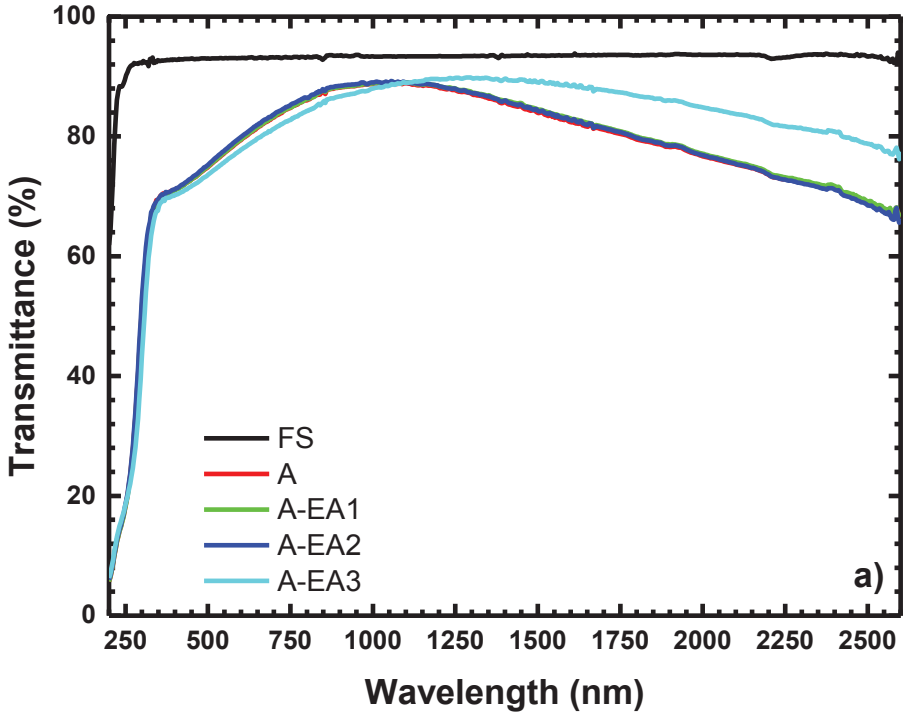

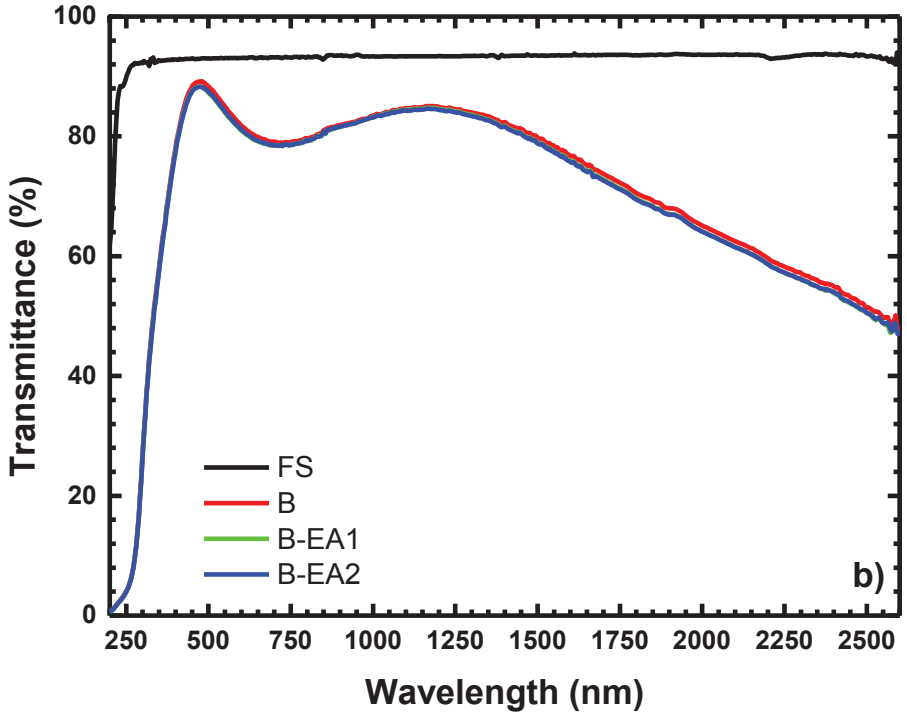

Figure 4.11. Transmittance spectra as a function of wavelength in the range of 200-2600 nm for the as grown and the electro-annealed ITO thin films grown on the fused silica substrate.

(cont. on next page)

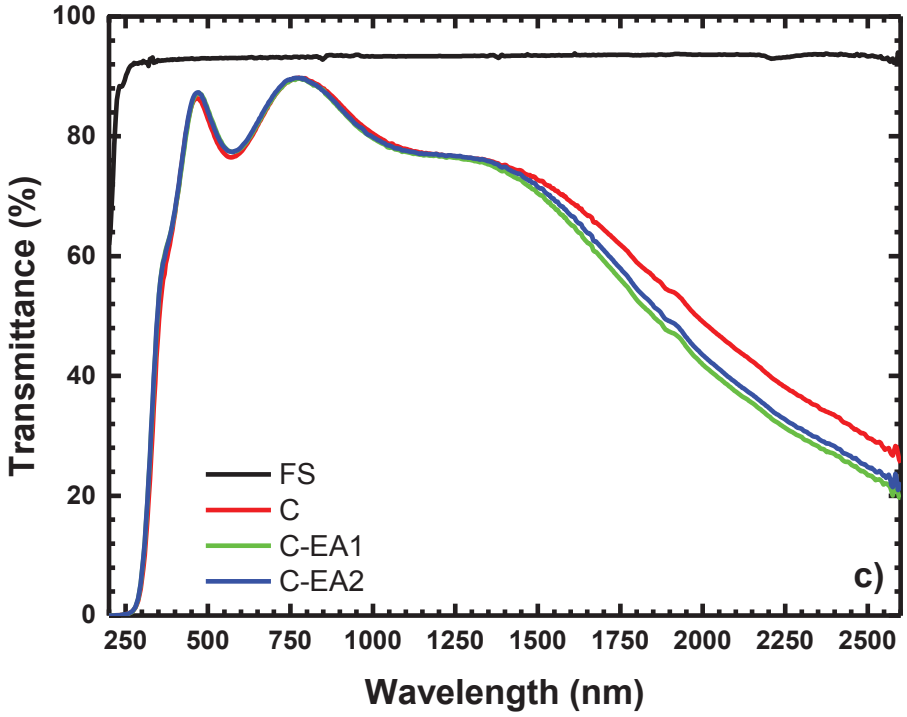

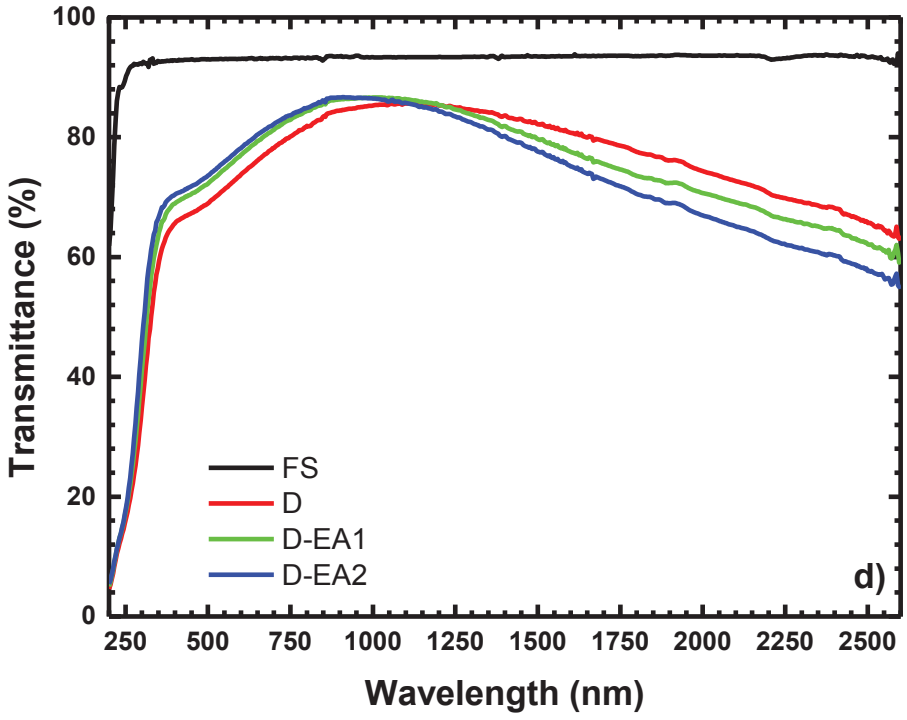

Figure 4.11. (cont.)

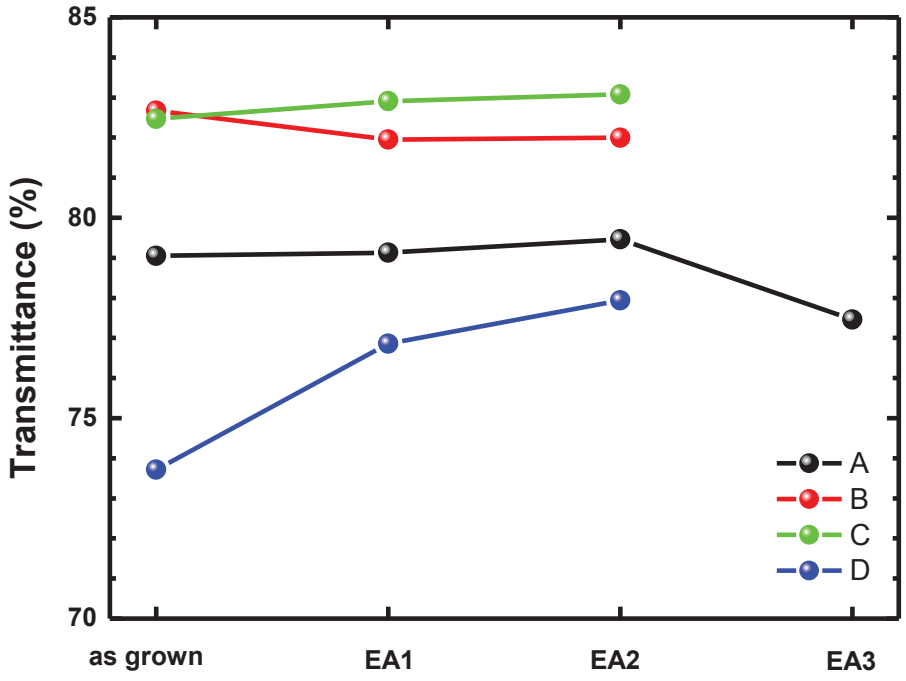

Figure 4.12. Variation of Transmittance (%) vs EA processes of as grown and electro-annealed ITO thin films grown on the fused silica substrate.

Table 4.3. Transmittance (%) of the as grown and electro-annealed ITO films at 550 nm.

	FS	ITO A	ITO B	ITO C	ITOD
as grown	93.07	77.31	84.85	77	71.41
EA1	-	77.43	83.84	78.13	74.75
EA2	-	77.76	84.01	78.02	75.98
EA3	-	75.82	-	-	-

In Figure 4.13., the absorption coefficient, α^2 versus photon energy ($h\nu$) plot was used to estimate the bandgap energy of the ITO thin films grown on the fused silica substrate. Since indium oxide has a direct transition, i.e. $\alpha h\nu = A(h\nu - E_g)^{1/2}$, the bandgaps of the films are deduced from the extrapolation of the linear plots of α^2 versus photon energy.

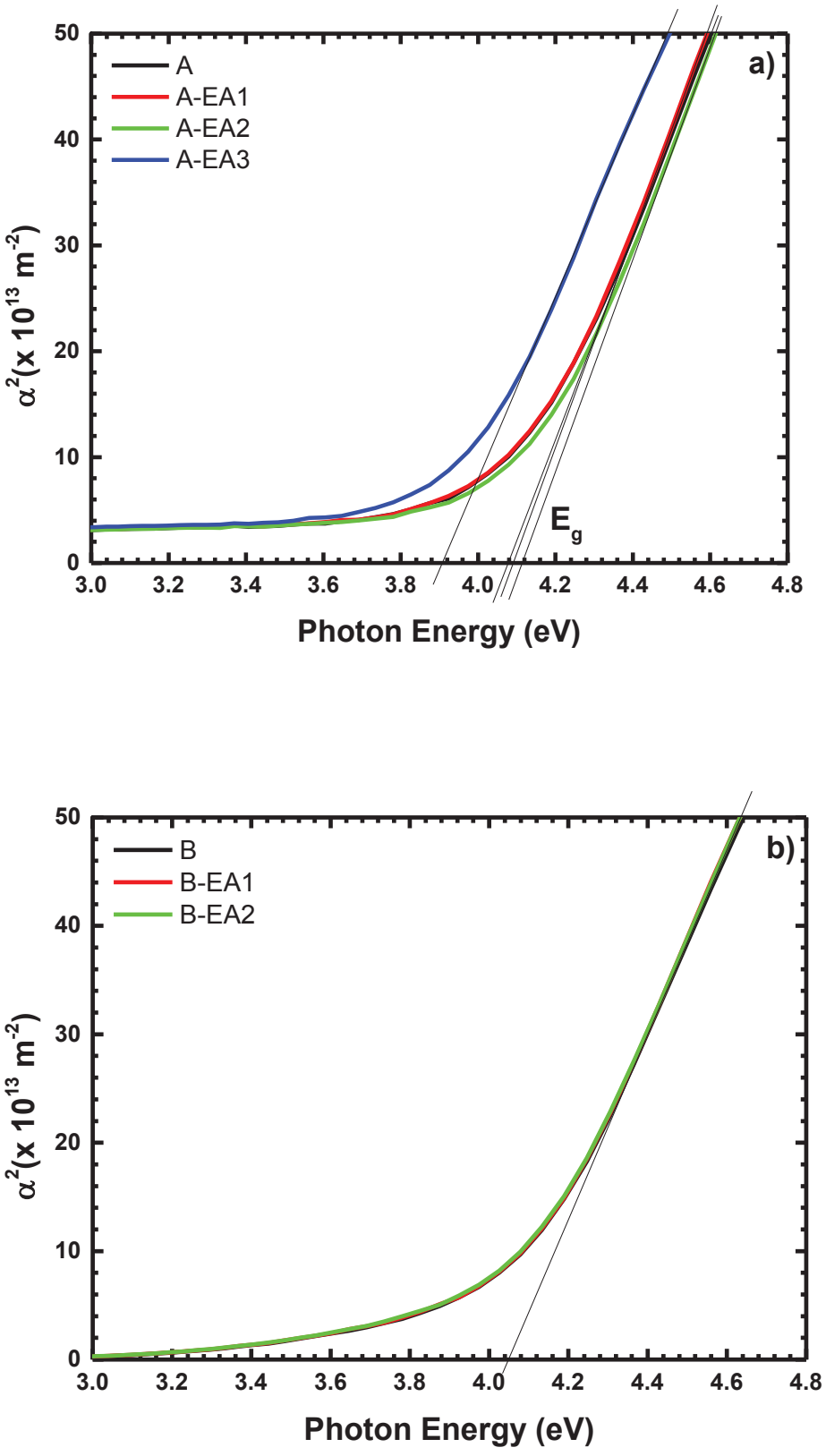

Figure 4.13. α^2 versus Photon Energy (hv) curve for the as grown and electro-annealed ITO films in a) air and b) vacuum.

(cont. on next page)

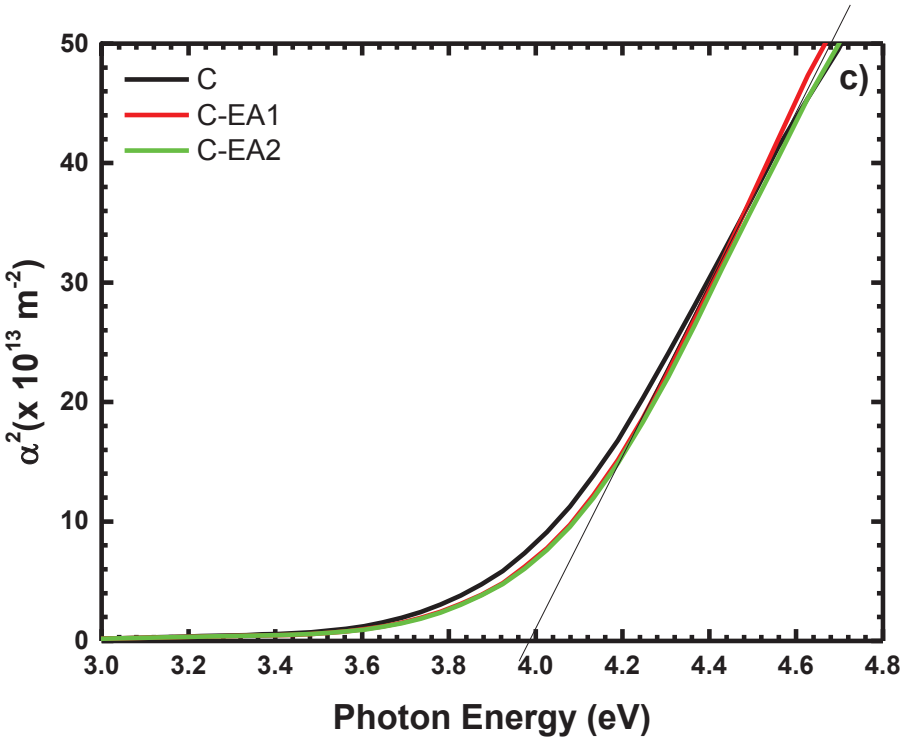

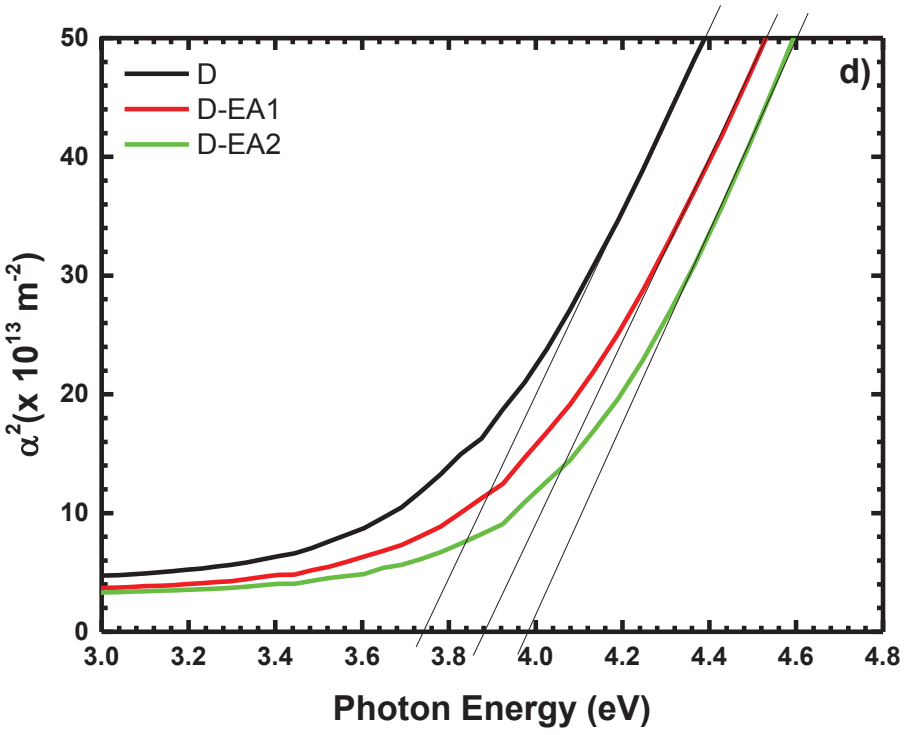

Figure 4.13. (cont.)

We observed that there is a correlation between the bandgap and R_s for the electro-annealing processes of the ITO thin films, i.e., while the resistivity decreases, the bandgap increases with respect to electro-annealing processes (Figure 4.14.). For the ITO A, ITO C and ITO D thin films, energy gap values increase from EA1 to EA2 electro-annealing process and decreased for the EA3 electro-annealing process for the ITO D thin film (Table 4.4.). The increase in the bandgap may be due to an increase in the carrier concentrations. This bandgap widening can be explained on the basis of the Burstein-Moss shift. However, at very high carrier concentrations, there may be band gap narrowing due to the electron-electron and electron-impurity scattering.

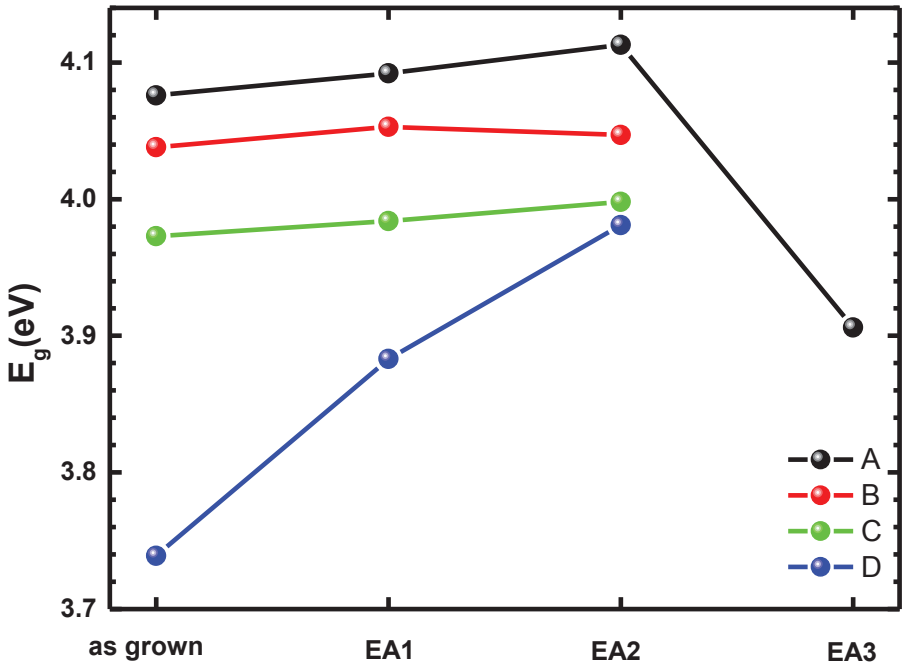

Figure 4.14. Variation of Energy gap (eV) vs EA processes of as grown and electro-annealed ITO thin films grown on the fused silica substrate.

Table 4.4. Energy gap (eV) of the as grown and electro-annealed ITO films.

	ITO A (eV)	ITO B (eV)	ITO C (eV)	ITO D (eV)
as grown	4.076	4.038	3.973	3.739
EA1	4.092	4.053	3.984	3.883
EA2	4.113	4.047	3.998	3.981
EA3	3.906	-	-	-

Refractive index (n) of the ITO thin films were calculated from the optical spectrum using the following equation (Chauhan, Anand, and Kumar 2014, Sofi, Shah, and Asokan 2018).

$$\frac{n^2+2}{2} = \sqrt{\frac{5}{E_g}} \tag{4.3}$$

where E_g is the optical band gap. The values of the refractive index (Table 4.5.) show a decreasing trend from as grown thin films to EA2 and increase for the EA3 thin film (Figure 4.15.). The change in the refractive index is related to the change of the energy band gap (E_g) (Chauhan, Anand, and Kumar 2014, Sofi, Shah, and Asokan 2018).

Table 4.5. Refractive index of the as grown and electro-annealed ITO films.

	ITO A (eV)	**ITO B (eV)**	**ITO C (eV)**	**ITO D (eV)**
as grown	0.464	0.475	0.494	0.559
EA1	0.459	0.471	0.490	0.519
EA2	0.453	0.472	0.486	0.491
EA3	0.513	-	-	-

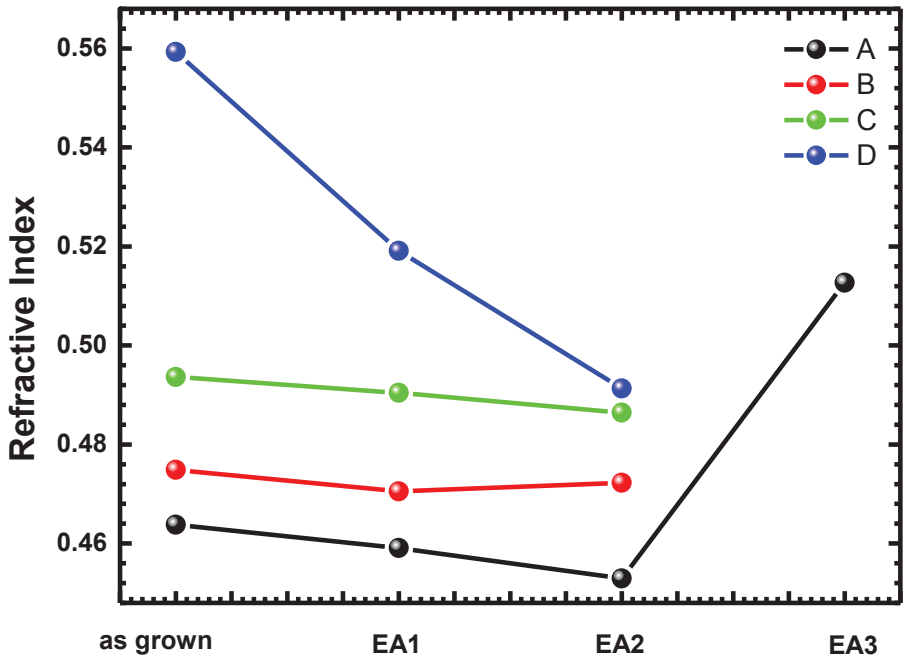

Figure 4.15. Variation of Refractive index vs EA processes of as grown and electro-annealed ITO thin films grown on the fused silica substrate.

4.2.2.4. THz Transmission Analysis

Figure 4.16. shows the THz transmission spectrum of air, Fused Silica (FS) substrate, metal and as grown and electro-annealed ITO thin films, in the frequency range of 0.500 - 0.750 THz. The absorption of air at around 0.560 THz can be seen in the THz transmission spectrum. Outside this region, the terahertz absorption effect of the air is not observed. Figure 4.12. a), c), e) and g) shows the raw data graph which is reading from Loc-in amplifier. Figure 4.12. b), d), f) and i) shows the THz transmittance (%) spectrum. For the normalized THz Transmittance (%) graphs, decreasing or increasing of the average THz Transmittance variations are strongly similar with the Rs variations of the thin films (Figure 4.17.). The observed spectrum is like a standing wave due to the interferences of the waves. Moreover, this shift in the spectrum observed due to the change in the refractive index of the thin films as a result of the change in the energy gap of the thin films. Moreover, the energy gap is also related with the Rs values and thicknesses of the thin films and it can be also related with the crystallinity of the thin films.

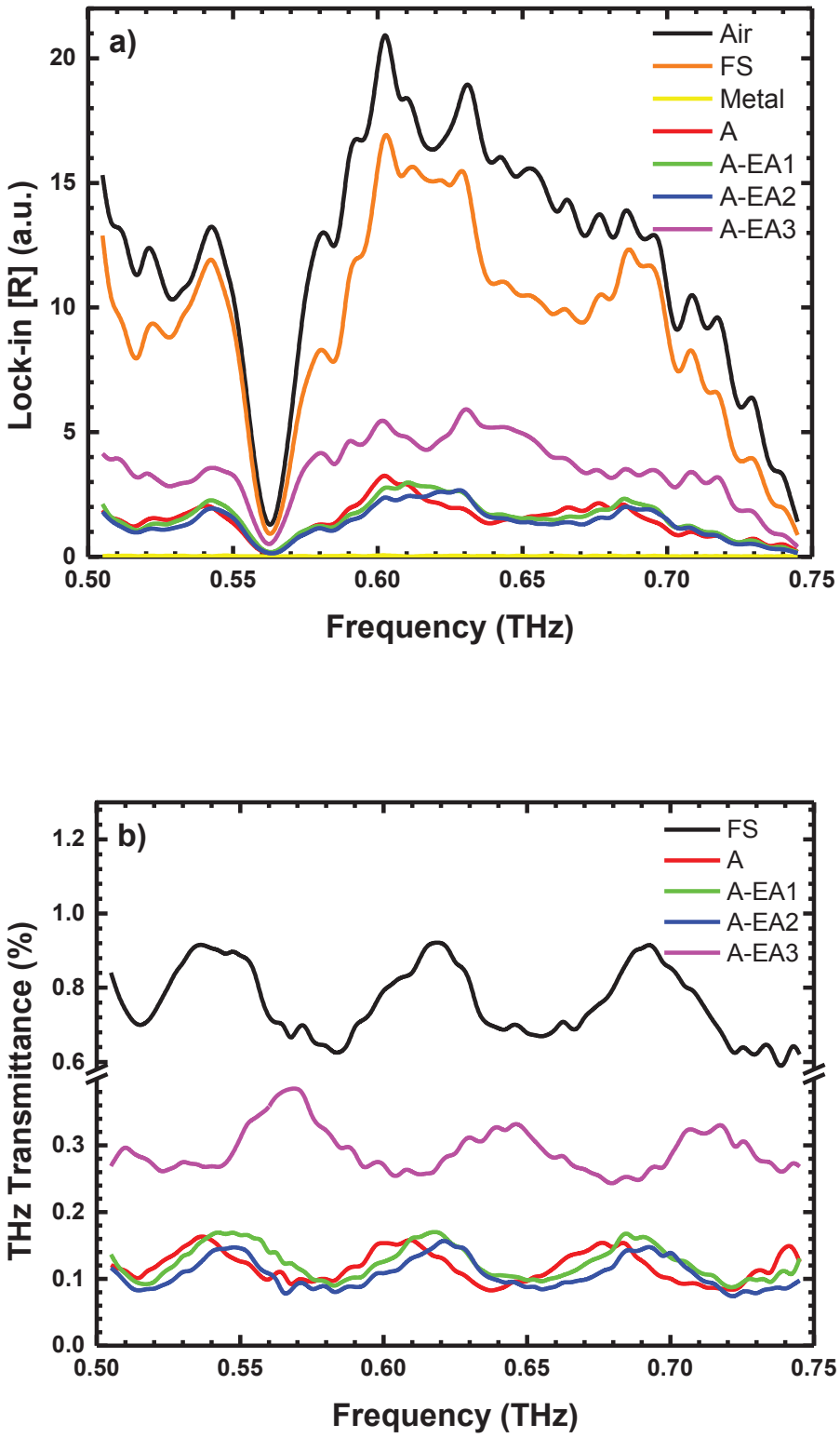

Figure 4.16. Raw data graph of a) ITO A, c) ITO B, e) ITO C and g) ITO D thin films reading from Loc-in amplifier and THz transmittance (%) spectrum of b) ITO A, d) ITO B, f) ITO C and i) ITO D thin films in the frequency range of 0.500 - 0.750 THz.

(cont. on next page)

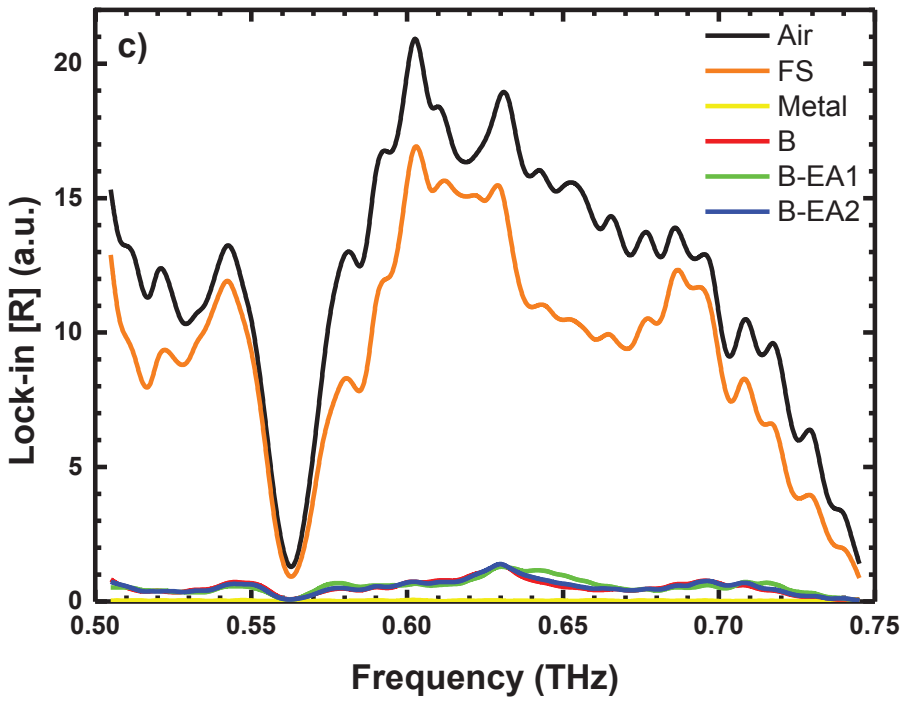

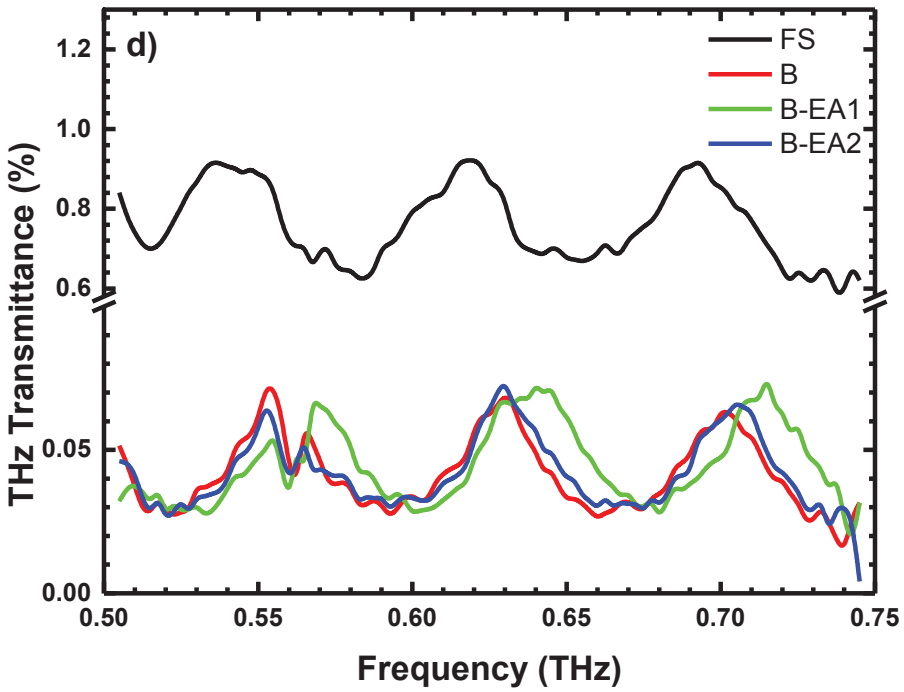

Figure 4.16. (cont.)

(cont. on next page)

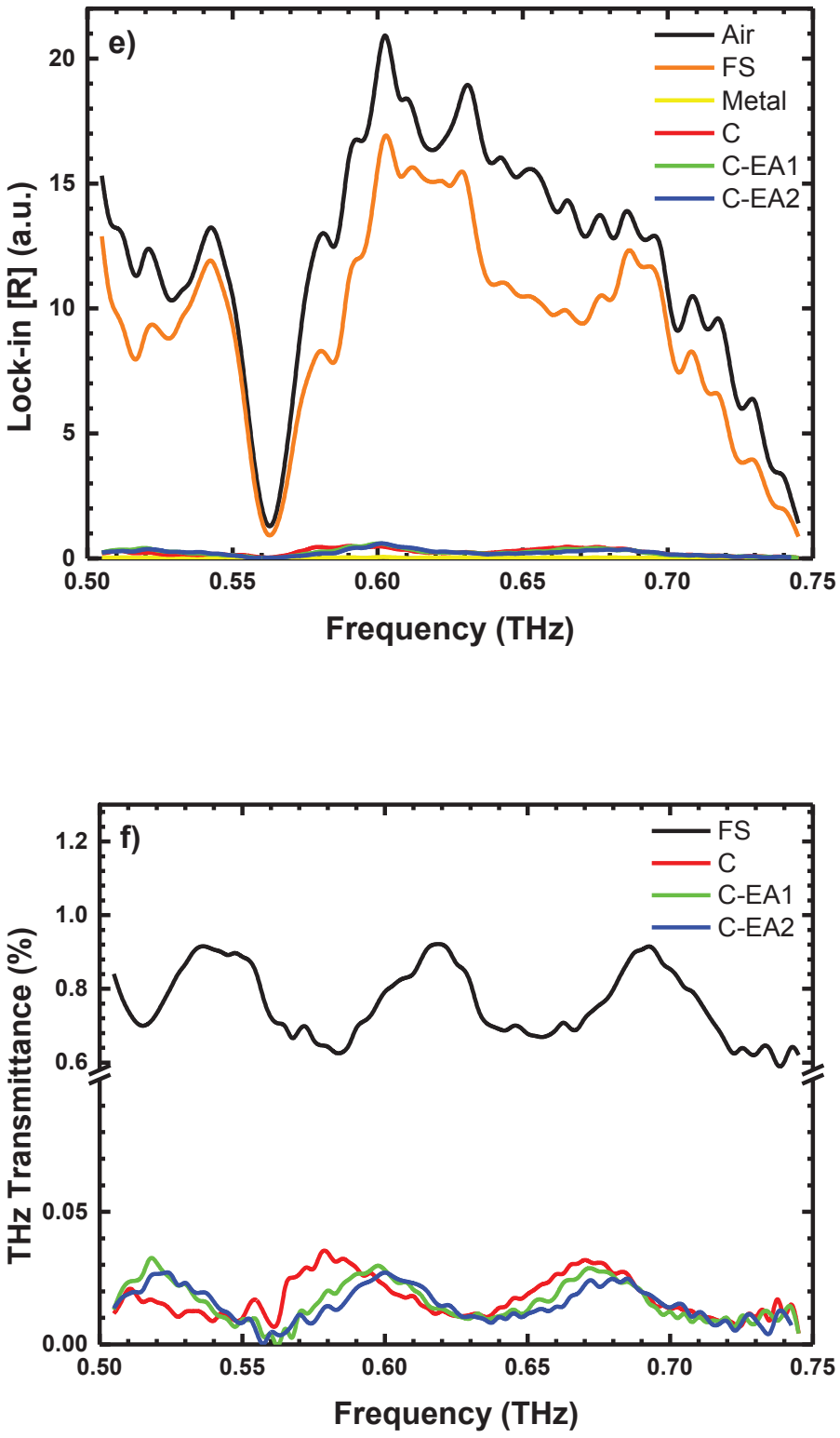

Figure 4.16. (cont.)

(cont. on next page)

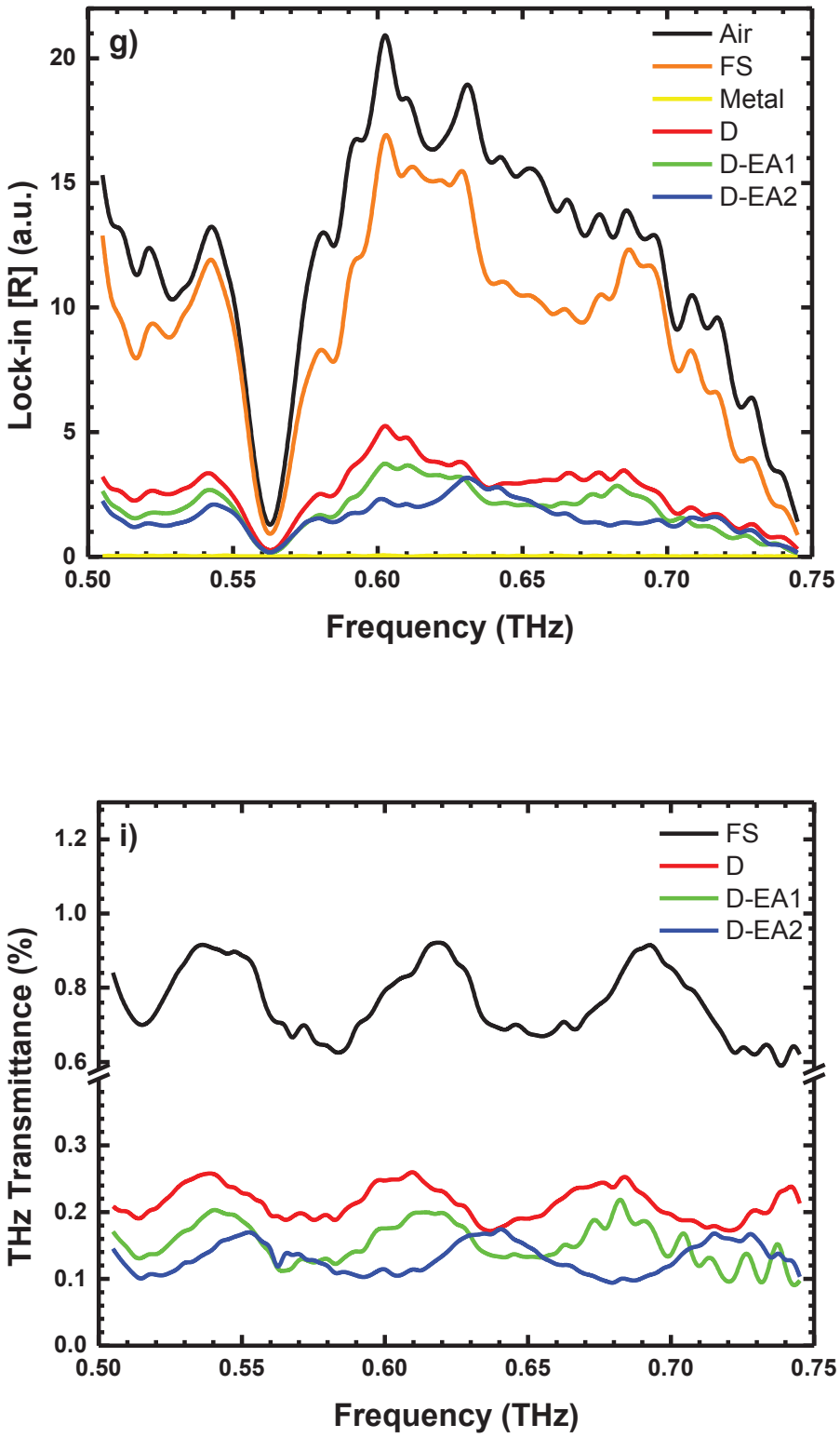

Figure 4.16. (cont.)

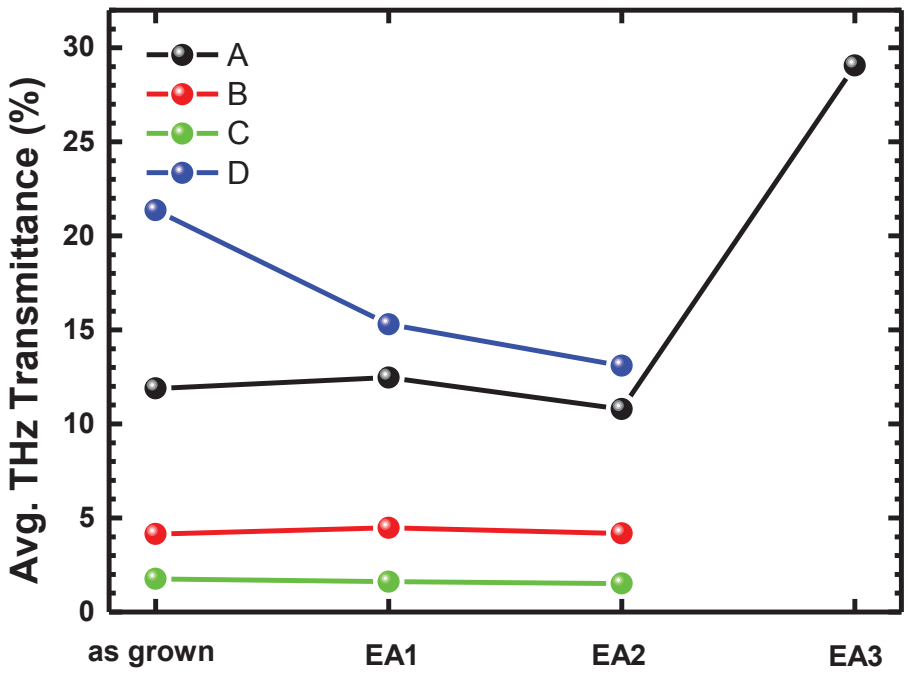

Figure 4.17. Variation of Average THz Transmittance (%) vs EA processes of as grown and electro-annealed ITO thin films grown on the fused silica substrate.

4.2.3. PET/ITO

Since Indium-tin oxide (ITO) has exceptional operational properties namely low electrical resistivity and high transparency with respect to other TCO materials (Stadler 2012), it has been extensively employed as transparent electrodes in many instruments. Due to their characteristic properties such as flexibility and lightweight, recently flexible electronic devices are appealing growing attention in the field of photovoltaics, thin-film transistors (TFTs) and integrated circuits (Choi et al. 2009, Cheng et al. 2010, Sierros et al. 2009, Dimes et al. 1994, Jingsheng, Chan-Park, and Li 2009). Moreover, this interest is in connection with the reality that when the flexible films are used as substrates the utilization of roll to roll processing is accomplished which initiate extremely significant gains in manufacturing productivity and economy (Cho et al. 2015). Thin metal foil, plastic materials or paper can be used in place of the flexible substrate as the support material in the flexible electronic devices. Plastic substrates in comparison with glass substrates, provide a good deal of superiority namely low weight, durability and an easy scale up to a large format. The flexibility property of these materials permits the modification of the device shape with the purpose of optimizing visibility and prohibit

reflections. On the other hand, since ITO is a natural fragile material, strength of ITO thin films is an important problem, which must be taken into account in the advancement of flexible optoelectronic technology. In DC magnetron sputtering method, it is feasible to control very strictly the thickness of the films which is an important advantage compared to other numerous deposition methods and consequently all the deposition parameters to accomplish required properties in ITO thin films could be taken under control consistently (Karasawa and Miyata 1993, Tuna et al. 2010, Yu et al. 2006, Kim et al. 2006, Meng and Placido 2003, Koseoglu et al. 2015). Hence, when the ITO films are produced by sputtering, they are extremely uniform and free from impurities, and also exhibit superior mechanical and adhesion characteristics. Nowadays, in order to achieve extremely conductive and transparent ITO film with outstanding uniformity and desirable adhesion to a flexible substrate by means of the sputtering technique, various efforts have been performed (Cho et al. 2015, Ko et al. 2016). Moreover, in the fabrication it is accessible to large-scale coating of high-quality ITO films on glass. In between the methods, since sputtering technique supplies high deposition rates where it is straightforward to control sputtering parameters and able to deposit on a large area of substrates with good thin films quality, this technique is mainly used to deposit the ITO thin films.

Remarkable results on roll-to-roll processed large area modules with high device efficiencies have been established in flexible substrates where ITO is introduced as transparent electrode (Park, Lee, Ko, et al. 2016, Kim et al. 2009, Park, Lee, Lee, et al. 2016). On the other hand, in specific ITO utilization namely for flexible optoelectronic devices, owing to the low thermal resistance of the polymer substrates, high substrate temperatures or high post-deposition annealing temperatures are unacceptable. After all, numerous works with a conventional sputtering chamber and small ITO target have been reported. It is believed that in the manufacturing, process circumstances are expected to be entirely distinct since the processing will be carried out on a large substrate where a relatively large cathode under a moving-state substrate is employed (the so-called in-line process). Aforesaid discrete processes will generate substantially different results on film properties for qualifications such as power, pressure, and gas ratio, etc.

4.2.3.1. Electrical Properties

In Table 4.6. and Figure 4.18. sheet resistances (R_s) of the ITO films on PET substrates are presented. There is a powerful relation between the amount of oxygen vacancies together with the microstructure and the sheet resistances of the ITO thin films (Baıa et al. 1999, Terzini, Thilakan, and Minarini 2000, Thilakan et al. 2001).

Due to the fact that the carriers in ITO films come to existence as a result of the creation of oxygen vacancies, the electrical properties are influenced by the oxygen partial pressure in the DC magnetron sputtering. A decrease in the electrical resistance in ITO coated PET samples is observed which is a consequence of the diminution of the oxygen amount in the sputter gas. As aforesaid, since one vacancy produces two electrons on the conduction band to assure the charge neutrality, it is known that the conductivity of ITO is related to the oxygen vacancies in the material. Oxygen vacancies in the deposited material is demanded to increase when the oxygen partial pressure decreases, accordingly accomplishing the films to be less stoichiometric or more metallic, which increases the conductivity and the number of charge carriers in the layers. Hence, deducing that a decrease in the oxygen flow rate leads to an enhanced conductivity and detecting a slight increase in the transmittance values is anticipated.

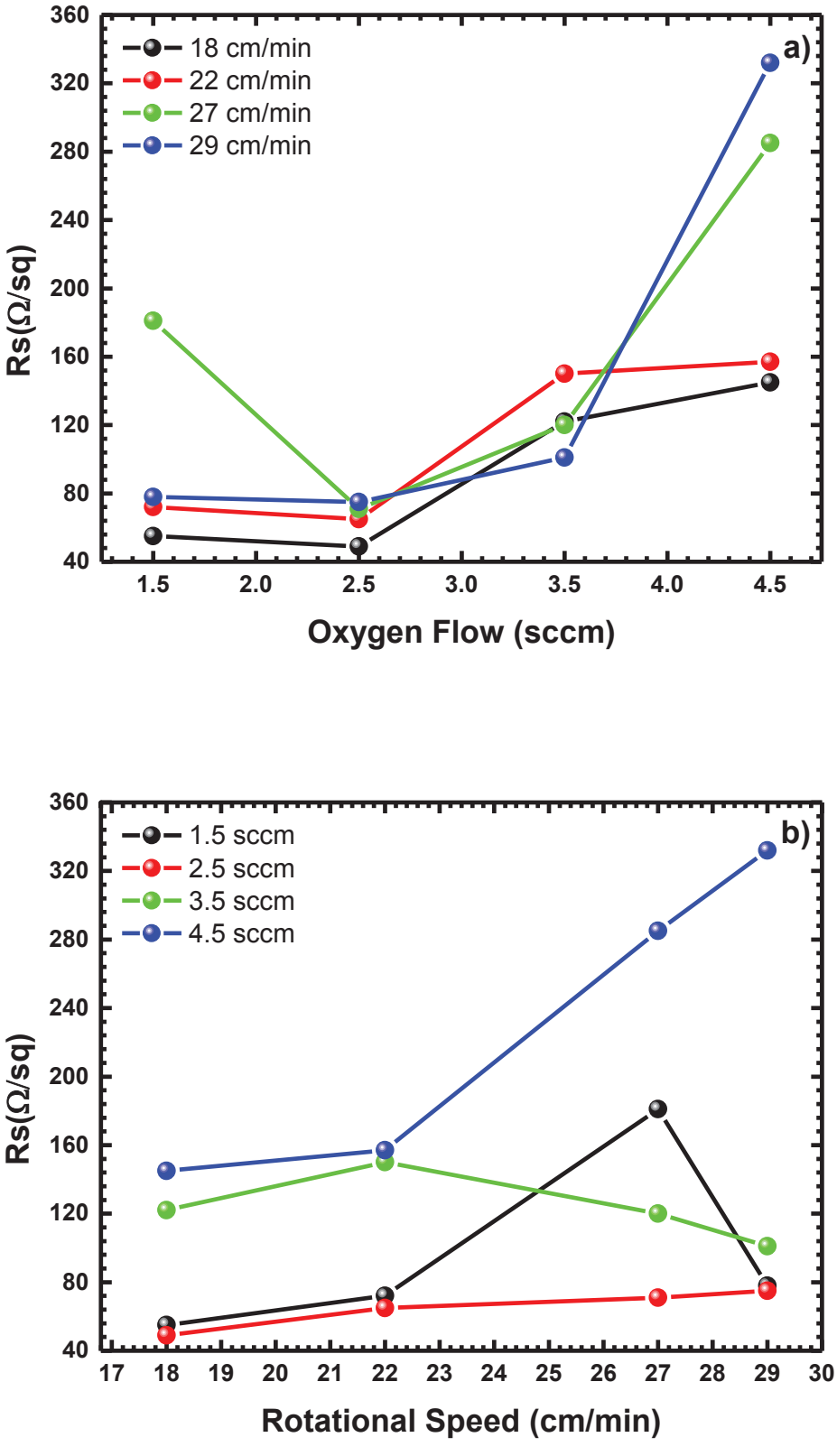

Figure 4.18. a) R_s vs. Oxygen flow and b) R_s vs. Rotational speed variation graph PET/ITO thin films.

Table 4.6. Thickness, Sheet resistance, Energy gap and FOM values of deposited ITO thin films with different roll-to-roll speed and O_2 flow rate.

Roll to roll speed (cm/min)	Ar flow rate (sccm)	Thickness (nm)	Sheet Resistance (Ω/□)	Eg (eV)	FoM ($x10^{-5}$ Ω^{-1})
18	1.5	190	55	3.44	13
18	2.5	190	49	3.42	6.1
18	3.5	190	122	3.38	2.4
18	4.5	190	145	3.35	1.4
22	1.5	150	72	3.46	5.0
22	2.5	150	65	3.42	3.2
22	3.5	150	150	3.40	1.6
22	4.5	150	157	3.39	1.0
27	1.5	120	181	3.76	1.3
27	2.5	120	71	3.73	1.2
27	3.5	120	120	3.72	1.2
27	4.5	120	185	3.70	8.8
29	1.5	90	78	3.86	1.8
29	2.5	90	75	3.86	2.3
29	3.5	90	101	3.85	1.9
29	4.5	90	332	3.84	13

4.2.3.2. Transmission Analysis

In Figure 4.19., optical transmittance at a visible wavelength from 200 to 2600 nm in the ITO films which are deposited with variable oxygen flow for each roll-to-roll speed is presented in order to compare with the associated PET substrate. In the visible range, the transmittance of the ITO films on PET substrates are observed to be lower than that of the PET substrate however the variation is not substantial. In spite of the fact that, in the growing process substrate heating or post-annealing was not adopted, a sharp absorption edge can be detected. In order to control the optical properties of ITO films, an important role was taken by oxygen gas flow. In Figure 4.19., the decrease of optical transmission while the oxygen gas flow rate increases from 1.5 to 4.5 sccm is presented whereas increasing film thickness also leads to a decrease of transmission. Thus, it is concluded that when excessive oxygen was included in the films the electrical conductivity together with the optical transmission of the films decreased. When oxygen flows are at higher rates, due to oxygen adsorption the excess oxygen is likely to accumulate on the grain boundary or surface which behaves as light scattering centers and this situation leads to the decrease in transmission of the films.

Once the optical characteristics of ITO deposited onto PET substrates at different oxygen partial pressure were compared, a substantial variation on infrared optical

transmittance was observed, however in the visible transmittance values an insignificant change was detected.

In the case of degenerate semiconductors namely ITO, when the near infrared region is considered the transmittance loss is associated to the plasma frequency where the transition between transparent to reflectance behavior takes place. The effective mass of the free electrons and the concentration of charge carriers in the film determine the plasma frequency.

In practice, TCO thin films involve maintaining high optical transmission and low sheet resistivity simultaneously but it is not always feasible. Consequently, the electrical and optical properties must be optimized to the excellent feasible limit. In order to compare the performance of different TCO thin films the figure of merit (FOM) for each thin film was adopted.

The transmission and electrical properties of the thin films are compared at the same time by the FOM values (Knickerbocker and Kulkarni 1995) where a better performance of the deposited material is indicated by a higher figure of merit.

$$\Phi T_C = T^{10}/R_s \tag{4.4}$$

where ΦT_C is FOM, T is the transmittance and R_s is the sheet resistance. The FOM values of our samples are calculated by the above given formula. Our calculations show that for the sample grown at 18 cm/min roll to roll speed and 1.5 sccm oxygen flow the highest value is attained. On the other hand, the least value is achieved for the films that was grown at 29 cm/min roll to roll speed and 4.5 sccm oxygen flow.

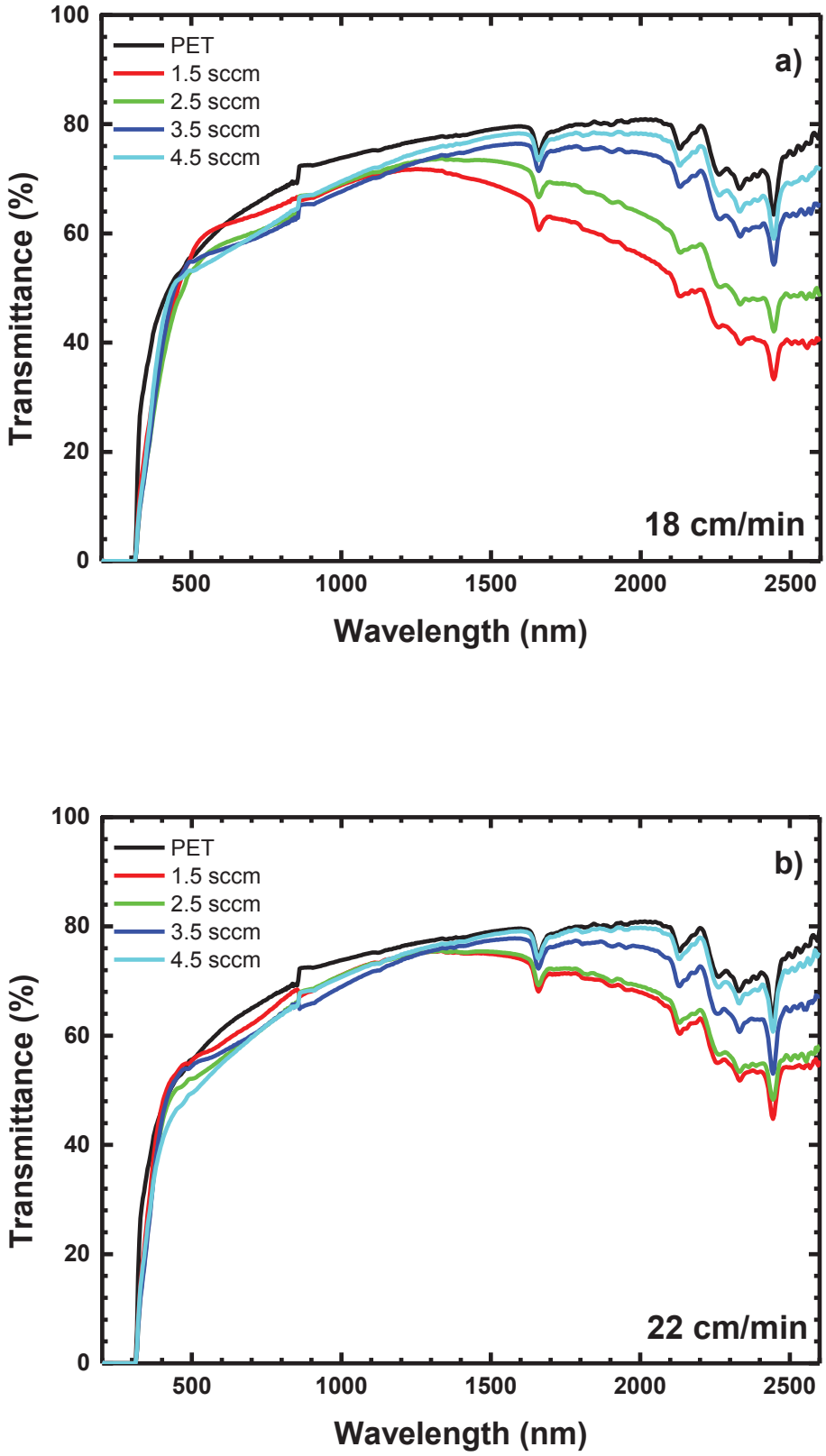

Figure 4.19. The optical transmittance analysis of the ITO films which are deposited with variable oxygen flow rates for (a) 18 cm/min, (b) 22 cm/min, (c) 27 cm/min and (d) 29 cm/min roll to roll speeds.

(cont. on next page)

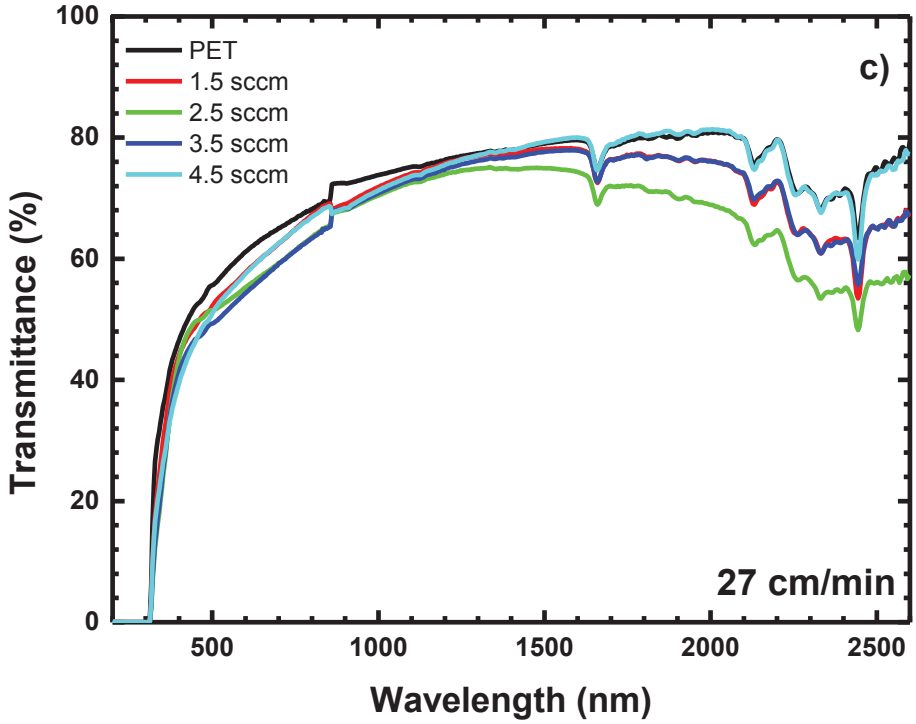

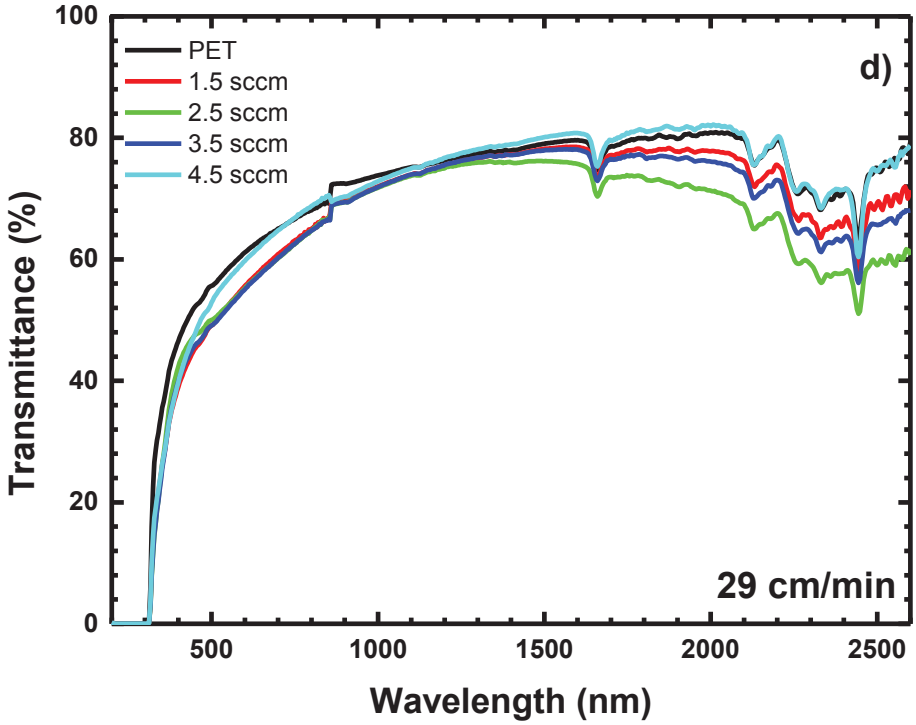

Figure 4.19. (cont.)

Once more proceeding with the trend in electrical and optical properties, the FOM gets better with the film thickness and reducing oxygen flow from 4.5 to 1.5 sccm, and this result is in agreement with our recent conclusions. The previous studies reported that the low transmittance value of the ITO thin films is a consequence of the low value of the Tauc gap. In the present study, we succeed to achieve transmittance values closer to bare PET substrates transmittivity. Since in the most of the optoelectronic applications' high energy gap value for ITO thin films is required, the Tauc method was adopted to calculate the energy gap of the samples. In the existing study, in order to estimate the band gap energy of the ITO thin films the absorption coefficient, α^2 versus photon energy ($h\nu$) plot was employed (Figure 4.20.).

In the calculation of absorption, the following equation is used;

$$T\text{-}R = e^{-\alpha t} \tag{4.5}$$

where T and R denote the transmittance and reflectance, respectively, and t is the thickness of the film. Since the reflectance of the films have a relatively low value it is ignored and then the absorption coefficient takes the simple form

$$\alpha^2 = \ln (T)^2/t^2. \tag{4.6}$$

Recalling that indium doped tin oxide has a direct transition, namely,

$$\alpha h\nu = A(h\nu - Eg) \tag{4.7}$$

the band gaps of the films are derived using the extrapolation of the linear plots of α2versus hν. In Figure 4.20., the direct optical band-gap values of large area ITO thin films for different roll to roll speeds and oxygen flow rates are given. When P_{O2} decreased, we notice that there is a small shift towards higher band gap energy values ranging from 3.32 to 3.44, 3.36 to 3.46, 3.60 to 3.76 and 3.78 to 3.86 eV for the roll-to-roll speeds of 18, 22, 27, 29 cm/min respectively (Table 4.6.). The above-mentioned difference may be attributed to the higher carrier concentrations in the samples with lower oxygen concentration. On the other hand, the above given values are in the range of other reported investigations (Kim et al. 2006, Kim et al. 2009, Koseoglu et al. 2015, Tuna et al. 2010).

A correlation between the band-gap and R_s values for all of the ITO thin films is obviously observed which implies that a decrease of resistivity leads to an increase in band-gap with respect to the increase in the carrier concentrations. In order to give an explanation to this band gap widening the Burstein-Moss effect is introduced where the lowest states in the conduction band are occupied and only transitions to higher states are allowed. Nevertheless, band gap narrowing may be observed at very high carrier concentrations as a result of the scattering at the electron-electron and electron-impurity level.

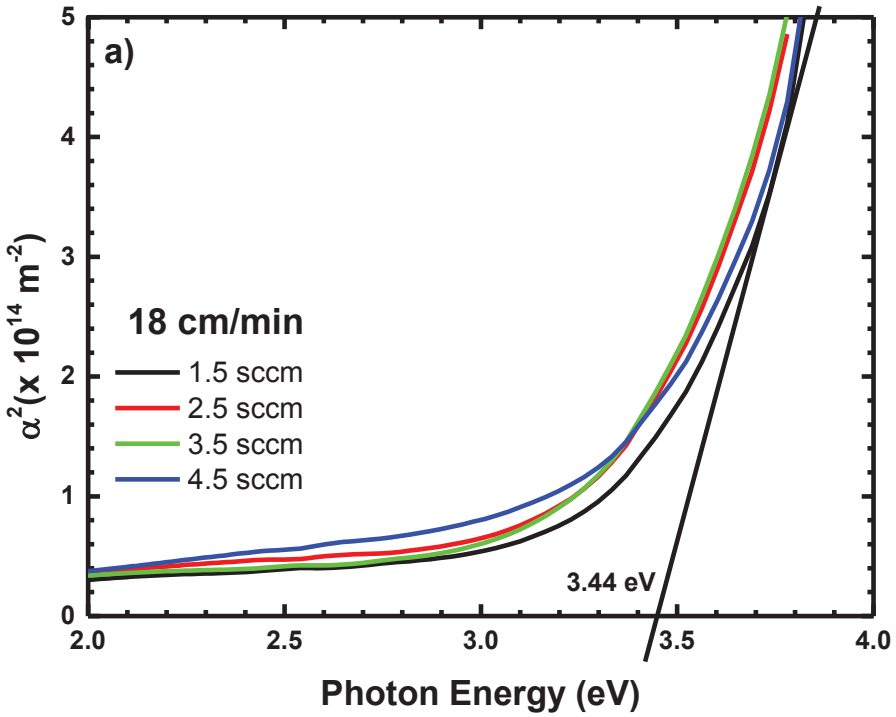

Figure 4.20. α^2 versus Photon Energy ($h\nu$) curves of the ITO films deposited with variable oxygen flow rates for a) 18 cm/min, b) 22 cm/min, c) 27 cm/min and d) 29 cm/min roll to roll speeds.

(cont. on next page)

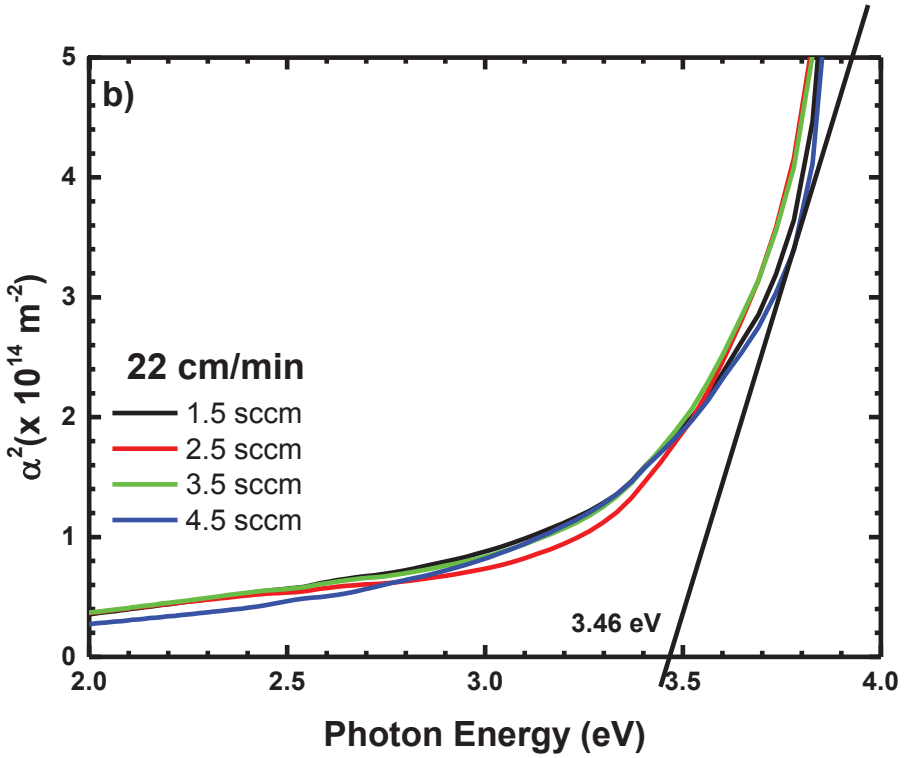

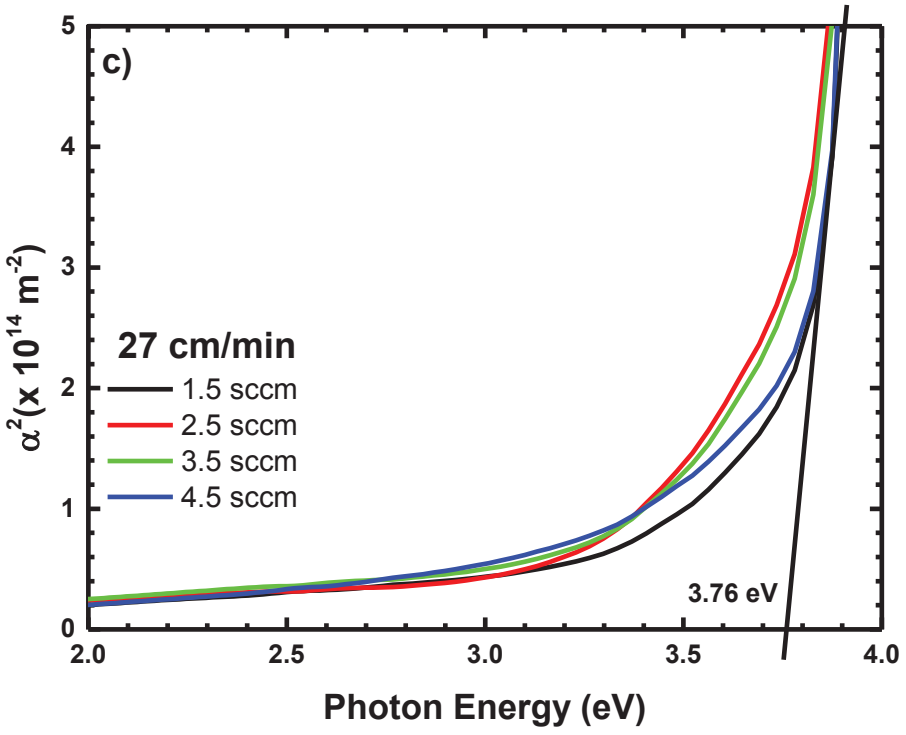

Figure 4.20. (cont.)

(cont. on next page)

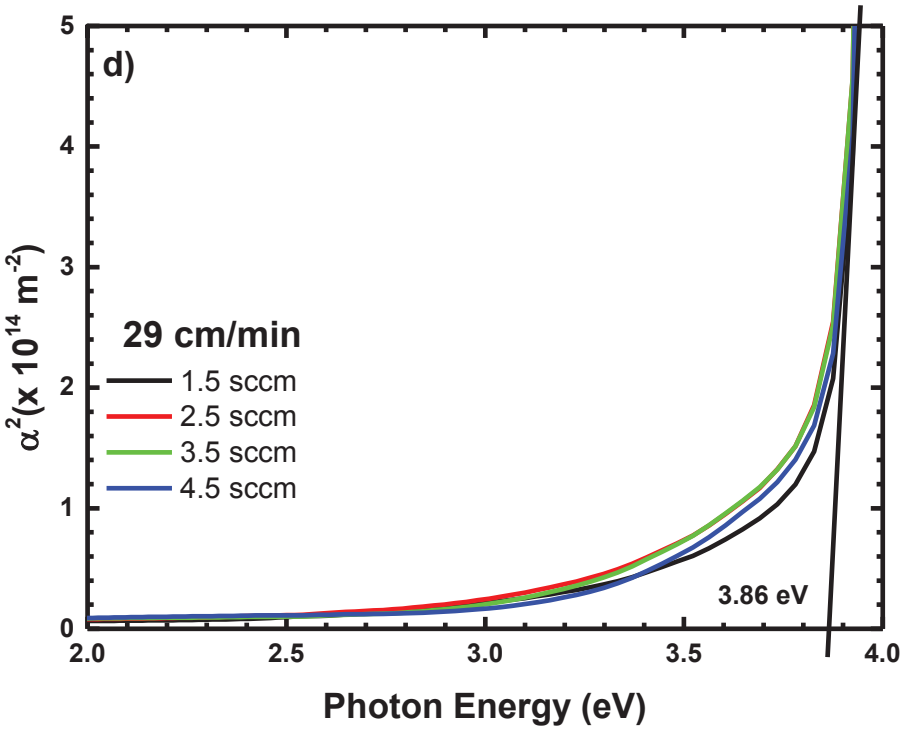

Figure 4.20. (cont.)

In Figure 4.21. a) and Figure 4.21. b), variation of optical band gap values of the ITO films deposited with respect to oxygen flows and roll-to-roll speed can be seen. The energy gap increase as the oxygen flows and roll-to-roll speed decrease. From Figure 4.21. c) and Figure 4.21. d), it is observed that the FOM values of the ITO films enhanced with both the film thickness and with reduction of oxygen flow from 4.5 to 1.5 sccm for the films with a roll-to-roll speeds of 18 and 22 cm/min (Table 4.6.).

In contesting ITO with sheet resistance, optical transparency and FOM values, large area ITO thin films have demonstrated a hopeful expectation.

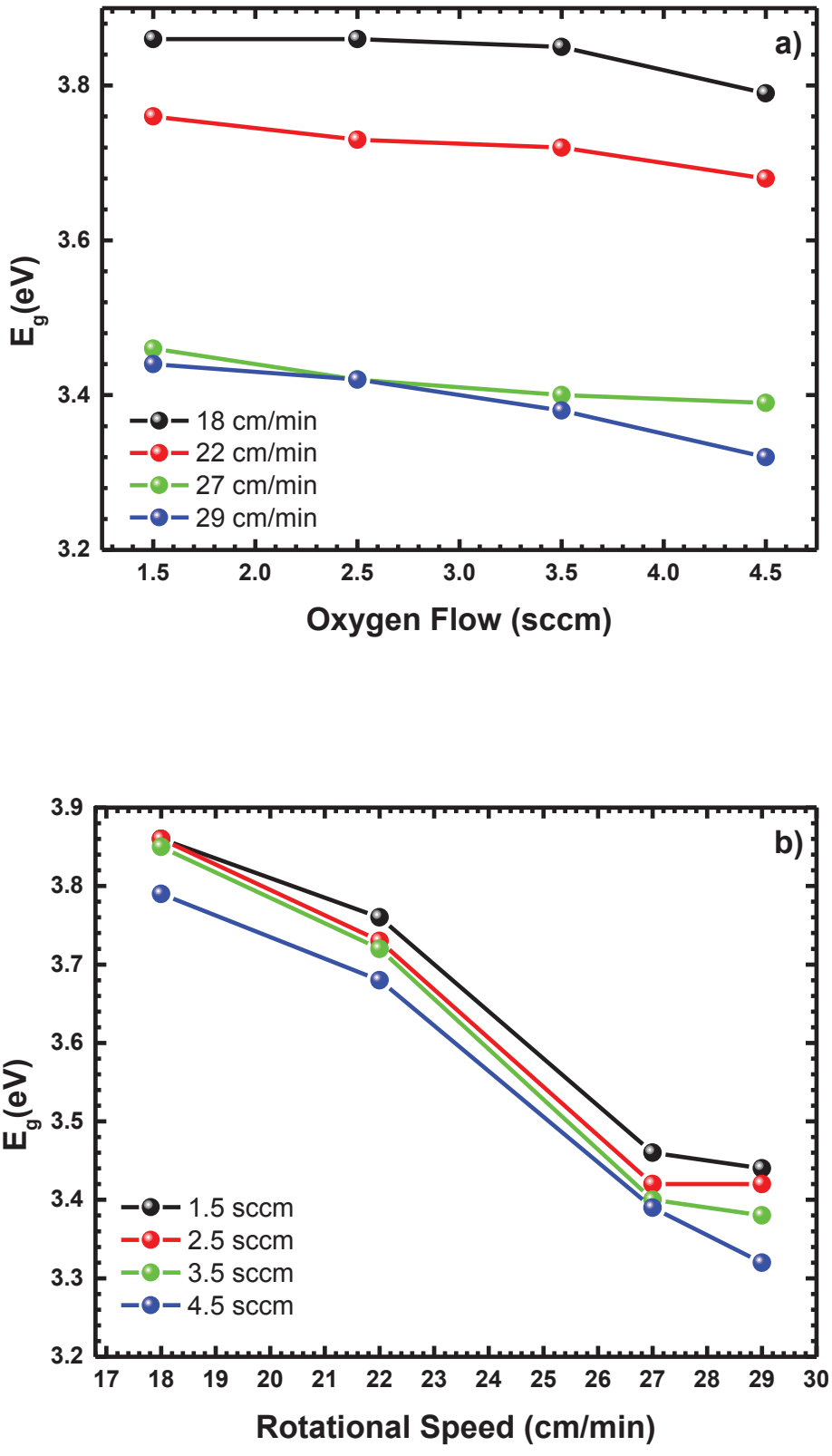

Figure 4.21. Variation of optical band gap values of the ITO films deposited with respect to a) oxygen flows and b) roll-to-roll speed. Variation of FOM values of the ITO films deposited with respect to a) oxygen flows and b) roll-to-roll speed.

(cont. on next page)

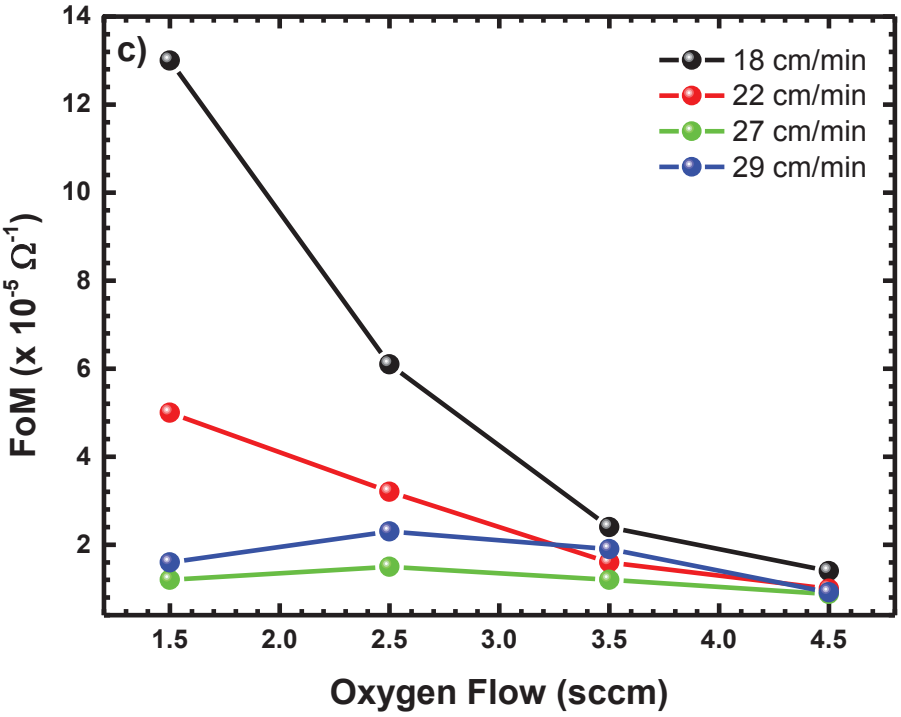

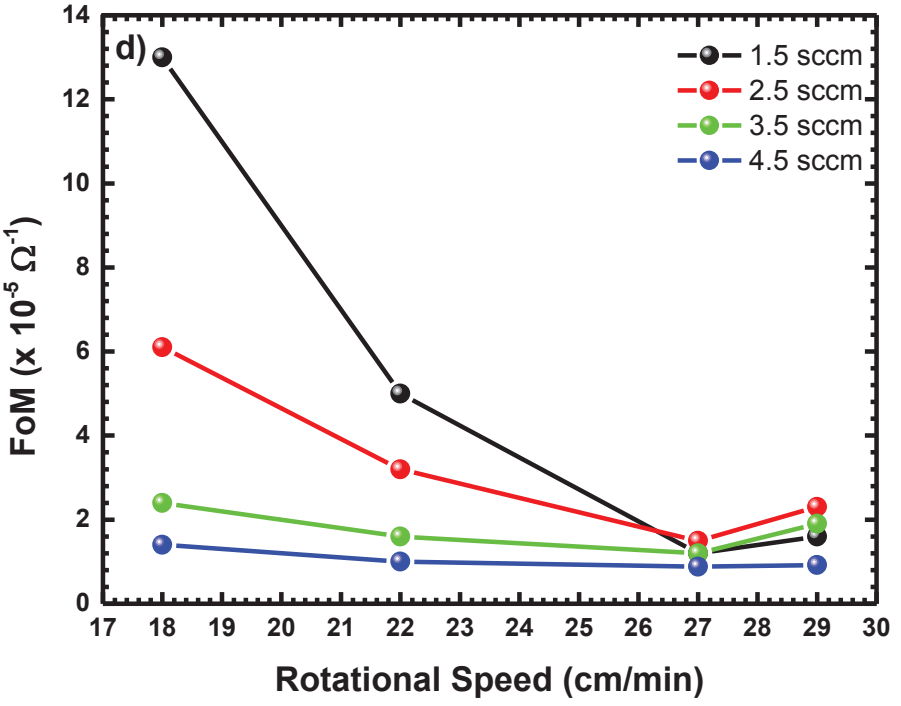

Figure 4.21. (cont.)

4.2.3.3. THz Transmission Analysis

Figure 4.22. shows the THz transmission spectrum of air, PET, metal and ITO thin films grown with different R2R speeds and oxygen flow rates, in the frequency range of 0.500-0.750 THz. The absorption of air at around 0.560 THz can be seen in the THz transmission spectrum. Outside this region, the terahertz absorption effect of the air is not observed. Figure 4.22. a), c), e) and g) shows the raw data graph which is reading from Loc-in amplifier. Figure 4.17. b), d), f) and i) shows the THz transmittance (%) spectrum. As it can be understood from Figure 4.22., THz transmittance of the ITO thin films is ranking from greater to smaller as "4.5-1.5-3.5-2.5 sccm" as increase the oxygen flow at each R2R velocity from 1.5 ‘to 4.5 sccm and the lowest THz transmittance was obtained with 2.5 sccm oxygen flow in the films at each R2R speed. Among the all data, the lowest THz transmittance was obtained with the parameters "18 cm/min + 2.5 sccm oxygen flow". When we compare the THz transmittance and R_s values, it is seen that they show parallelism. Since the O_2 concentration of the ITO thin film and oxygen voids affect the surface resistance, it affects the THz transmittance. As a result, it is understood that thin films with low R_s have low THz transmittance and hence high reflectivity.

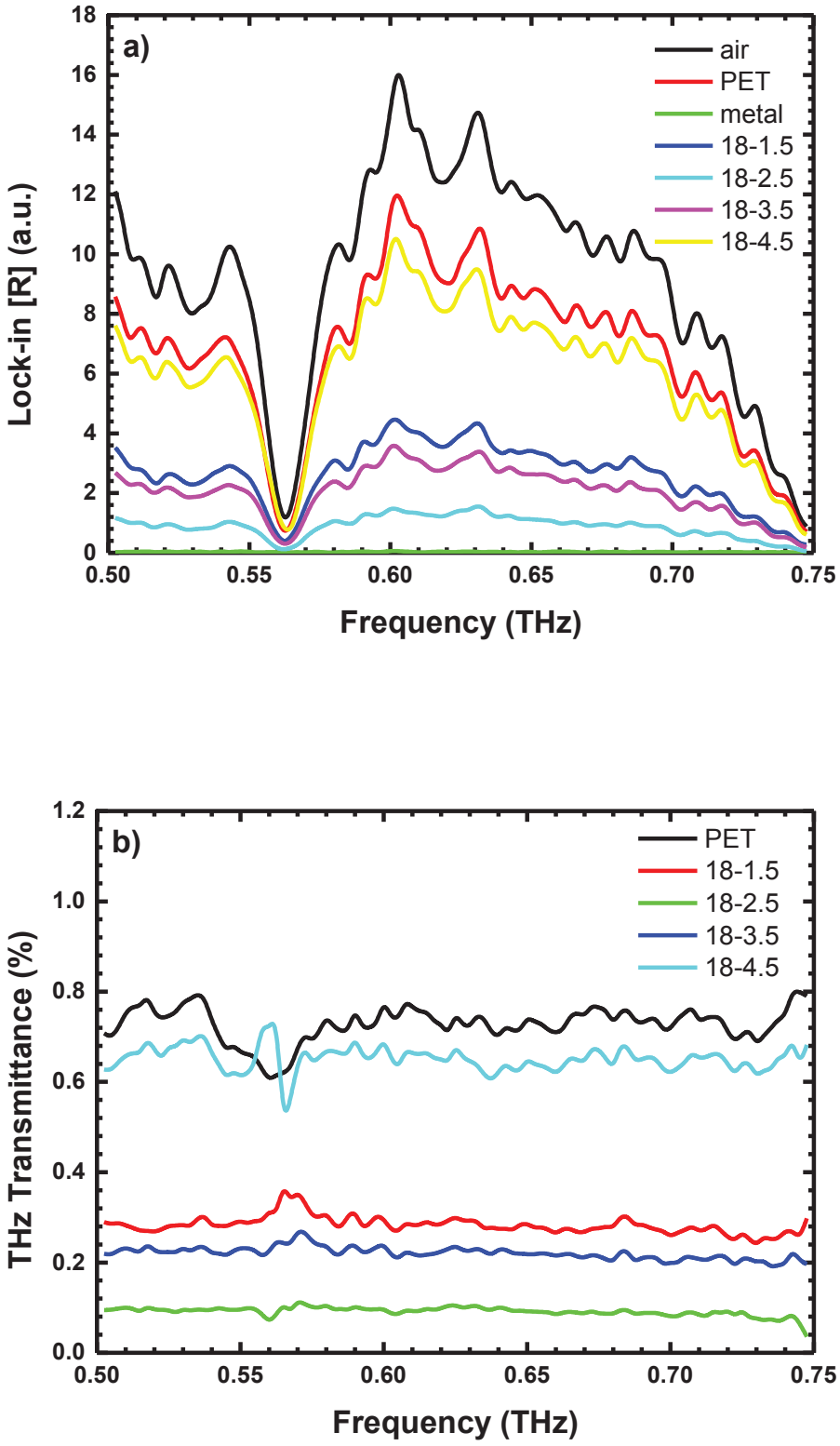

Figure 4.22. THz transmittance spectrum raw data graphs of ITO thin films coated on PET substrates with a) 18 cm/min, c) 22 cm/min, e) 27 cm/min, f) 29 cm/min and THz Transmittance (%) spectrum of ITO thin films coated on PET substrates with a) 18 cm/min, c) 22 cm/min, e) 27 cm/min, f) 29 cm/min.

(cont. on next page)

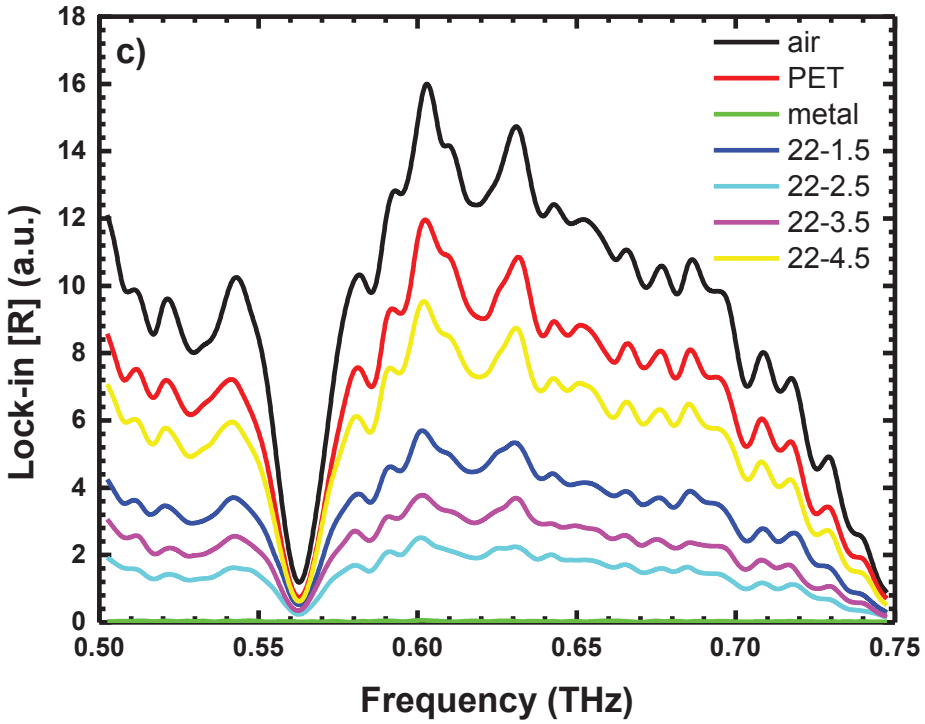

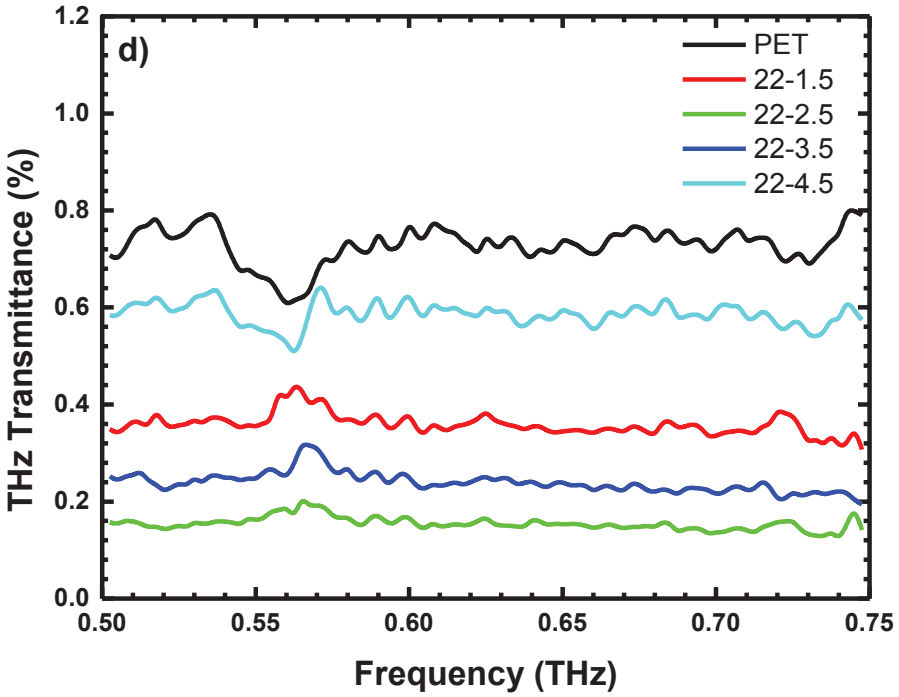

Figure 4.22 (cont.)

(cont. on next page)

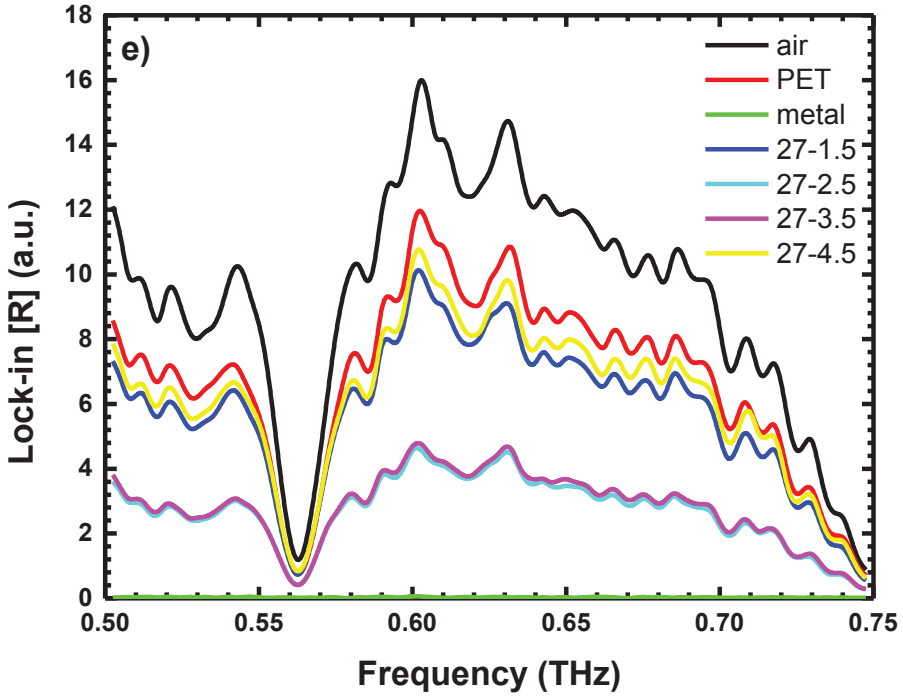

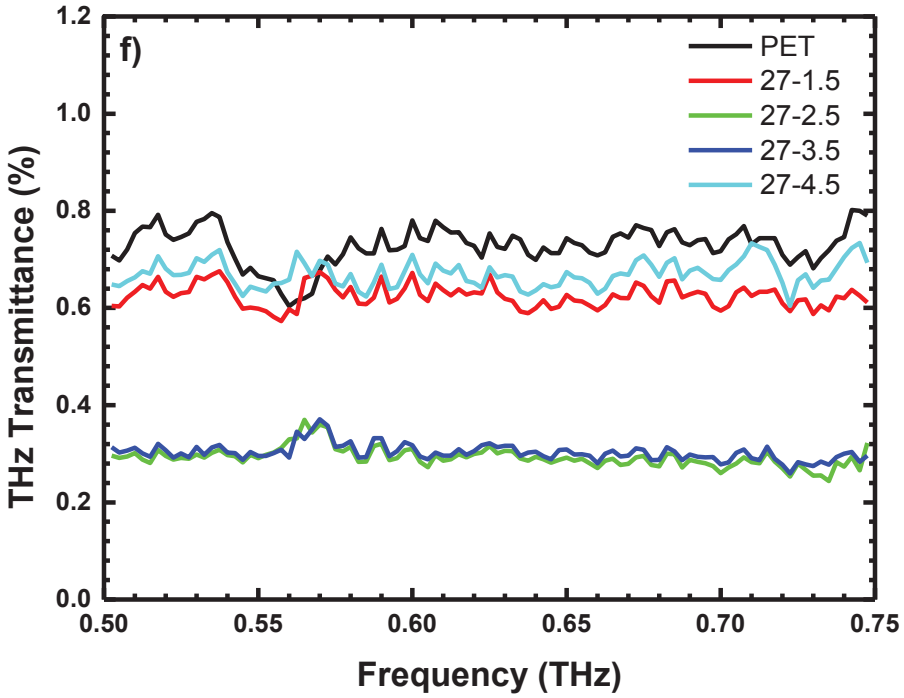

Figure 4.22 (cont.)

(cont. on next page)

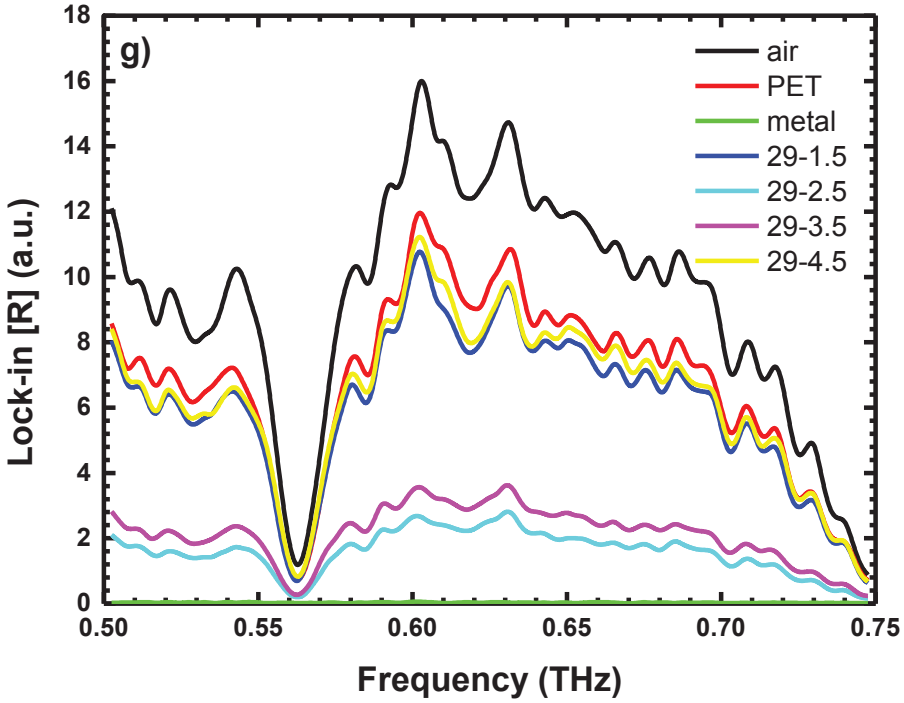

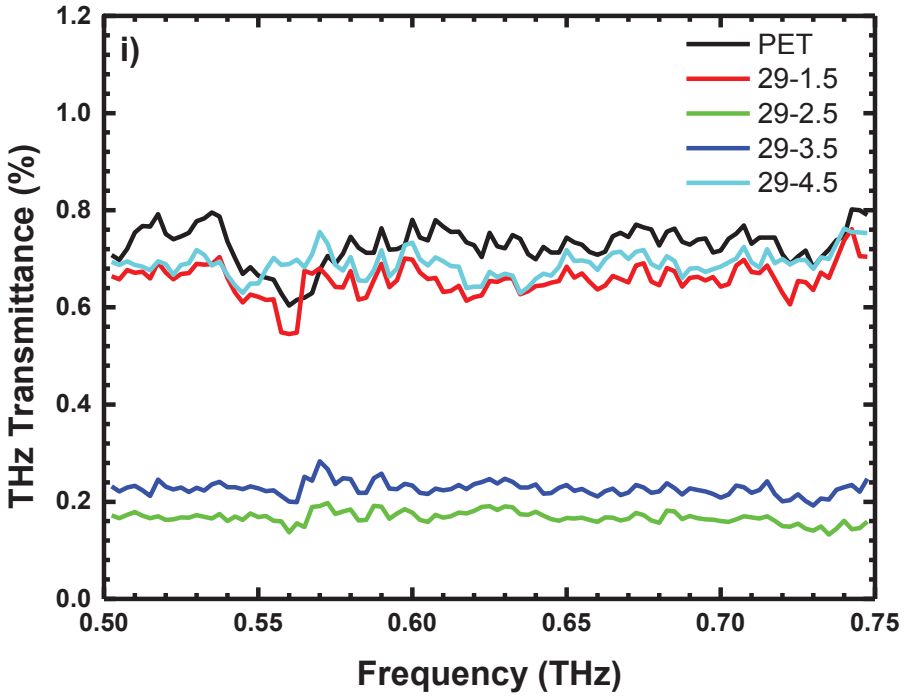

Figure 4.22 (cont.)

Figure 4.23. shows how the average THz transmittance of ITO thin films coated on PET substrate change with O_2 flow (Figure 4.23. a)) and R2R cycle rate (Figure 4.23. b)). In Figure 4.23. a), average THz transmittance decreases as the O_2 flow rate from 1.5 sccm to 2.5 sccm flow rate and increases as the O_2 flow rate from 2.5 sccm to 4.5 flow rate. In Figure 4.23. b), it is seen that the average THz transmittance increases up to 27 cm/min speed and then decreases at 29 cm/min speed.

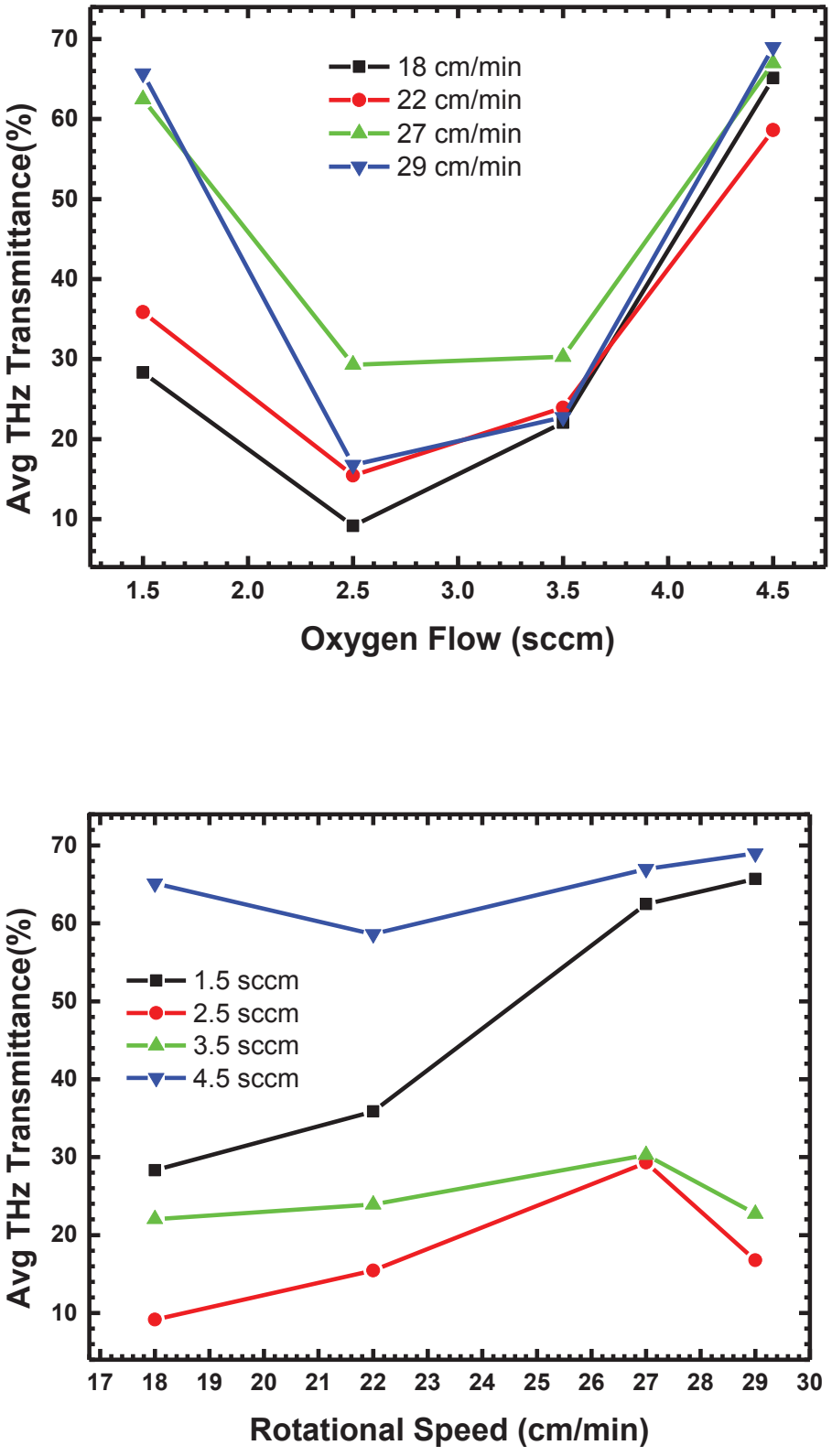

Figure 4.23. Average THz transmittance (%) values of ITO thin films coated on PET variation with respect to a) Oxygen Flow and b) rotational speed.

CHAPTER 5

CONCLUSION

CW THz imaging system, which consist of the THz Source operating in the frequency range of 0.500 - 0.750 THz which has a RF Generator, frequency counter and VDI WR1.5 AMC (Amplified / Multiplier Chain (Amplified / Multiplier Chain), 90° off axis parabolic mirror (4 pieces), x-y motion mechanism with sample holder and Golay Cell as a detector were designed and setup. THz image of the various samples such as leaf, metal and concealed objects were taken by direct 2D (x-y) scanning of the samples. 0.537 THz frequency were used in the THz imaging. The leaf image demonstrates one of the key THz features, its sensitivity to water, with higher water content leaf veins showing higher attenuation. For the metal-based object, THz waves does not penetrate and totally absorbed or reflected from the samples and signal read as 0 from the lock-in amplifier.

Understanding the effect of electric current on ITO thin films is essential to increase the life time of electronic devices. In this study, we analyzed the effect of electro-annealing by applying 0.75, 1.00, 1.25 and 1.50 A constant ac currents to the ITO thin films in air and vacuum for 10 minutes on the structural, optical and electrical properties of the crystalline ITO thin films grown by large area DC magnetron sputtering at the 250°C substrate temperature. Both for electro-annealing in air and vacuum, we observed improvement on structural, optical and electrical properties of the ITO thin films due to electro-annealing process. For the electro-annealing in vacuum, the R_s of the films decreased with increasing currents due to an increase of the temperature by electro-annealing. In comparison with the electro-annealed ITO films in vacuum, the sheet resistances of the electro-annealed ITO films in air are higher due to the reaction of free oxygen in ambient with the ITO films and less crystallization. For the electro-annealing in air, the R_s of the films decreased up to 1 A since the lower temperature of the film and for the higher current values than 1 A, high temperature results increase in the R_s of the thin films. The XRD patterns of all the films indicate a cubic In_2O_3 phase. It was observed that all ITO thin films are crystalline and have strong (222) and (400) peaks showing preferred orientations. For all of the electro-annealed ITO thin films, it can be clearly seen that the crystallinity of the films improves by increasing electro-annealing currents.

Moreover, for the ITO thin films electro-annealed in vacuum, the crystallinity of the thin films was more improved compared to the thin films electro-annealed in air and ITO thin films electro-annealed in vacuum are more oriented along (400) plane at the same current. The transmittance spectra as a function of wavelength in the range of 200-2600 nm for the as grown and the electro-annealed ITO thin films at different currents in air and vacuum were measured. The electro-annealing process enhances the average transmittance of thin films (including borosilicate substrate) in the visible region between 400 nm and 800 nm which is about 73% for the as grown ITO thin films and it increases up to 82% both for electro-annealing in vacuum and air. Moreover, average transmittance increases by increasing currents values. In the near infrared region, there exists a correlation between the NIR transmittance and R_s of the films for both electro-annealing in air and vacuum. Lower resistivity values have lower transmission of the infrared region. For the direct optical band gap of the as grown and electro-annealed ITO thin films in air and vacuum, which is deduced from the extrapolation of the linear plots of α^2 versus photon energy, there is a correlation between the bandgap and Rs for all of the electro-annealed thin films, i.e., while the resistivity decreases, the bandgap increases with respect to the increased annealing current. Our findings indicate that electro-annealing in vacuum is a more appropriate technique for the applications in the industry.

Large area magnetron sputtering system was used for the deposition of ITO thin films on the Fused Silica (FS) substrate. For the FS substrate, 4 different ITO thin films were deposited. Three of them have the same deposition parameters except sample holder speed (or thickness) and the other one was not heated during the deposition. Due to the decrease in the Rs at low temperature electro-annealing in the BS/ITO samples in the air (up to 1.00 A electro-annealing), we prefer to perform the electro-annealing of FS/ITO thin films at 100°C with 20 min duration at that temperature (except EA3, which performed at 200°C with 20 min duration for cooperation.). For the electro-annealing of FS/ITO samples we performed 3 types of process (detail can be seen in the experimental section); 1) EA1: 100°C-20 min - setting temperature using temperature controller, 2) EA2: 100°C-20 min - setting temperature manually, 3) EA2: 200°C-20 min - setting temperature manually. Improvement of optical, structural and electrical properties of the ITO thin films deposited on the Fused Silica substrate were achieved by electro-annealing processes. EA2 process is better than EA1 process due to the continuously applied voltage during electro-annealing. EA3 process is the worst one due to the high temperature electro-annealing. THz Transmittance of the ITO thin films are strongly related and

similar with the R_s of the thin films. The observed spectrum is like a standing wave due to the interferences of the waves. Moreover, this shift in the spectrum observed due to the change in the refracting index of the thin films as a result of the change in the energy gap of the thin films. Moreover, the energy gap is also related with the Rs values and thicknesses of the thin films and it can be also related with the crystallinity of the thin films.

The large area magnetron sputtering system modified with unwind and rewind rollers and a rotational feedthrough mechanism instead of linear movable sample holder with feedthrough system used to deposited the ITO large area films with different Ar/O_2 ratio and roll to roll speed (18, 22, 27, 29 cm/min) for every ten meters of the PET substrate. There is a powerful relation between the amount of oxygen vacancies together with the microstructure and the sheet resistances of the ITO thin films. Grown ITO thin films are amorphous structure due to the un-heated deposition. The sheet resistance (R_s), optical transmittance and energy gap of ITO thin film increase, while the oxygen gas flow rate decreases from 4.5 to 1.5 sccm. While the roll-to-roll rotation speed decreases, sheet resistances and optical transmission of ITO thin film decrease and energy gap of ITO thin film increase. The figure of merit (FOM) values of the ITO thin films gets better, as the thin film thicknesses (or decreasing in the roll-to-roll rotation speed) increases and oxygen gas flow rate decrease from 4.5 to 1.5 sccm. THz transmittance of the ITO thin films is ranking from greater to smaller as "4.5 - 1.5 - 3.5 - 2.5 sccm" and the lowest THz transmittance was obtained with 2.5 sccm oxygen flow rate at each roll-to-roll rotational speed. The lowest THz transmittance was obtained with the parameters "18 cm/min + 2.5 sccm O2 flow". Variation of the THz Transmittance of the ITO thin films with oxygen gas flow rate and roll-to-roll rotational speed are similar with the R_s of the ITO thin films.

We observed that the fabricated ITO thin films have potential applications in the field of THz systems such as a THz beam splitter, THz filter, modulator and reflector (without 1 μm film thickness). The transparent thin film devices have critical importance to enhance the performance of the THz systems. Due to the growing need for the high-speed data transmission, the working frequency of the wireless communication has been directed to the Terahertz frequency. Moreover, operating frequency needs higher frequencies, because commonly used GHz frequency has a low bandwidth. For the next 5 years, the working frequency of the communication in 8G could be in the THz region with high bandwidth.

REFERENCES

Ali, NI Mohd, N Misran, MF Mansor, and MF Jamlos. 2017. "Transparent solar antenna of 28 GHz using transparent conductive oxides (TCO) thin film." Journal of Physics: Conference Series.

Auston, DH, and PR Smith. 1983. "Generation and detection of millimeter waves by picosecond photoconductivity." *Applied Physics Letters* 43 (7):631-633.

Baıa, I, M Quintela, L Mendes, P Nunes, and R Martins. 1999. "Performances exhibited by large area ITO layers produced by rf magnetron sputtering." *Thin Solid Films* 337 (1-2):171-175.

Bárdoš, L, and M Libra. 1989. "Effect of the oxygen absorption on properties of ITO layers." *Vacuum* 39 (1):33-36.

Beerman, Henry P. 1969. "The pyroelectric detector of infrared radiation." *IEEE Transactions on Electron Devices* 16 (6):554-557.

Bellingham, JR, WA Phillips, and CJ Adkins. 1990. "Electrical and optical properties of amorphous indium oxide." *Journal of Physics: Condensed Matter* 2 (28):6207.

Bellingham, JR, WA Phillips, and CJ Adkins. 1991. "Amorphous indium oxide." *Thin Solid Films* 195 (1-2):23-32.

Bellingham, JR, WA Phillips, and CJ Adkins. 1992. "Intrinsic performance limits in transparent conducting oxides." *Journal of Materials Science Letters* 11 (5):263-265.

Brau, Charles A. 1988. "Free-electron lasers." *Science* 239 (4844):1115-1121.

Brown, Elliott R, WD Zhang, H Chen, and GT Mearini. 2015. "THz behavior of indium-tin-oxide films on p-Si substrates." *Applied Physics Letters* 107 (9):091102.

Burstein, Elias. 1954. "Anomalous optical absorption limit in InSb." *Physical Review B* 93 (3):632.

Cai, Fuhong, Yalun Wang, Min Gao, and Sailing He. 2018. "The design and implementation of a low-cost multispectral endoscopy through galvo scanning of a fiber bundle." *Optics Communications* 428:1-6.

Chan, Wai Lam, Jason Deibel, and Daniel M Mittleman. 2007. "Imaging with terahertz radiation." *Reports on progress in physics* 70 (8):1325.

Chauhan, Ram Narayan, RS Anand, and Jitendra Kumar. 2014. "Structural, electrical and optical properties of radio frequency sputtered indium tin oxide thin films modified by annealing in silicon oil and vacuum." *Thin Solid Films* 556:253-259.

Chen, Hou-Tong, Roland Kersting, and Gyu Cheon Cho. 2003. "Terahertz imaging with nanometer resolution." *Applied Physics Letters* 83 (15):3009-3011.

Chen, Q, and X-C Zhang. 2001. "Semiconductor dynamic aperture for near-field terahertz wave imaging." *IEEE Journal of Selected Topics in Quantum Electronics* 7 (4):608-614.

Cheng, Yuang-Tung, Jyh-Jier Ho, Chien-Kun Wang, William Lee, Chih-Chiang Lu, Bao-Shun Yau, Jhen-Liang Nain, Shun-Hsyung Chang, Chiu-Cheng Chang, and Kang L Wang. 2010. "Improvement of organic solar cells by flexible substrate and ITO surface treatments." *Applied surface science* 256 (24):7606-7611.

Cho, Da-Young, Yong-Hee Shin, Han-Ki Kim, Yong-Jin Noh, Seok-In Na, and Kwun-Bum Chung. 2015. "Roll-to-roll sputtered Si-doped In2O3/Ag/Si-doped In2O3 multilayer as flexible and transparent anodes for flexible organic solar cells." *Journal of Vacuum Science Technology A: Vacuum, Surfaces, Films* 33 (2):021501.

Choi, Kwang-Hyuk, Jin-A Jeong, Jae-Wook Kang, Do-Guen Kim, Jong Kuk Kim, Seok-In Na, Dong-Yu Kim, Seok-Soon Kim, and Han-Ki Kim. 2009. "Characteristics of flexible indium tin oxide electrode grown by continuous roll-to-roll sputtering process for flexible organic solar cells." *Solar Energy Materials Solar Cells* 93 (8):1248-1255.

Chopra, KL, S Major, and DK Pandya. 1983. "Transparent conductors—a status review." *Thin solid films* 102 (1):1-46.

Colombel, Franck, Xavier Castel, Mohamed Himdi, Gérard Legeay, Sonia Vigneron, and E Motta Cruz. 2009. "Ultrathin metal layer, ITO film and ITO/Cu/ITO multilayer towards transparent antenna." *IET science, measurement technology* 3 (3):229-234.

Conwell, E, and VF Weisskopf. 1950. "Theory of impurity scattering in semiconductors." *Physical Review B* 77 (3):388.

Darrow, JT, BB Hu, X-C Zhang, and DH Auston. 1990. "Subpicosecond electromagnetic pulses from large-aperture photoconducting antennas." *Optics letters* 15 (6):323-325.

De Wit, JHW. 1973. "Electrical properties of In2O3." *Journal of solid state chemistry* 8 (2):142-149.

De Wit, JHW. 1977. "Structural aspects and defect chemistry in In2O3." *Journal of Solid State Chemistry* 20 (2):143-148.

Demirhan, Yasemin, Hasan Koseoglu, Fulya Turkoglu, Zemzem Uyanik, Mehtap Ozdemir, Gulnur Aygun, and Lutfi Ozyuzer. 2020. "The controllable deposition of large area roll-to-roll sputtered ito thin films for photovoltaic applications." *Renewable Energy* 146:1549-1559.

Dhillon, SS, MS Vitiello, EH Linfield, AG Davies, Matthias C Hoffmann, John Booske, Claudio Paoloni, M Gensch, Peter Weightman, and GP Williams. 2017. "The 2017 terahertz science and technology roadmap." *Journal of Physics D: Applied Physics* 50 (4):043001.

Dimes, D, WL Warren, MB Sinclair, BA Tut-tie, and RW Schwartz. 1994. "Photoinduced hysteresis changes and optical storage in (Pb, La)(Zr, Ti) 03 thin films and ceramics." *Journal of Applied Physics* 76 (7):4305.

Dingle, RB. 1955. "XCIV. Scattering of electrons and holes by charged donors and acceptors in semiconductors." *The London, Edinburgh, Dublin Philosophical Magazine Journal of Science* 46 (379):831-840.

Erginsoy, Cavid. 1950. "Neutral impurity scattering in semiconductors." *Physical Review B* 79 (6):1013.

Fan, John CC, Frank J Bachner, and George H Foley. 1977. "Effect of O2 pressure during deposition on properties of rf-sputtered Sn-doped In2O3 films." *Applied Physics Letters* 31 (11):773-775.

Fan, John CC, and John B Goodenough. 1977. "X-ray photoemission spectroscopy studies of Sn-doped indium-oxide films." *Journal of Applied Physics* 48 (8):3524-3531.

Fattinger, Ch, and D Grischkowsky. 1988. "Point source terahertz optics." *Applied Physics Letters* 53 (16):1480-1482.

Federici, John, and Lothar Moeller. 2010. "Review of terahertz and subterahertz wireless communications." *Journal of Applied Physics* 107 (11):6.

Ferguson, Bradley, and Xi-Cheng Zhang. 2002. "Materials for terahertz science and technology." *Nature materials* 1 (1):26-33.

Fujiwara, Mikio, Takanori Hirao, Mitsunobu Kawada, Hiroshi Shibai, Shuji Matsuura, Hidehiro Kaneda, Mikhail Patrashin, and Takao Nakagawa. 2003. "Development of a gallium-doped germanium far-infrared photoconductor direct hybrid two-dimensional array." *Applied optics* 42 (12):2166-2173.

Ginley, David S, Hideo Hosono, and David C Paine. 2010. *Handbook of transparent conductors*: Springer Science & Business Media.

Golay, Marcel JE. 1949. "The Theoretical and Practical Sensitivity of the Pneumatic Infra-Red Detector." *Review of Scientific Instruments* 20 (11):816-820.

Hamberg, I, CG Granqvist, K-F Berggren, BE Sernelius, and L Engström. 1985. "Bandgap widening in heavily doped oxide semiconductors used as transparent heat-reflectors." *Solar Energy Materials* 12 (6):479-490.

Hamberg, Ivar, and Claes G Granqvist. 1986. "Evaporated Sn-doped In2O3 films: Basic optical properties and applications to energy-efficient windows." *Journal of Applied Physics* 60 (11):R123-R160.

Hamberg, Ivar, Claes Göran Granqvist, K-F Berggren, Bo E Sernelius, and L Engström. 1984. "Band-gap widening in heavily Sn-doped In 2 O 3." *Physical Review B* 30 (6):3240.

Hamdi, AH, RCO Laugal, AB Catalan, AL Micheli, and No W Schubring. 1991. "Doping, patterning and analysis of tin oxide films using ion beams." *Thin solid films* 198 (1-2):9-15.

Harding, 6_G L, and B Window. 1990. "DC magnetron reactively sputtered indium・ tin ・ oxide films produced using argon・ oxygen・ hydrogen mixtures." *Solar energy materials* 20 (5-6):367-379.

Hashimshony, D, I Geltner, G Cohen, Y Avitzour, A Zigler, and C Smith. 2001. "Characterization of the electrical properties and thickness of thin epitaxial semiconductor layers by THz reflection spectroscopy." *Journal of Applied Physics* 90 (11):5778-5781.

Hong, Seungman, Youngsung Kim, and Chang Won Jung. 2016. "Transparent microstrip patch antennas with multilayer and metal-mesh films." *IEEE antennas wireless propagation letters* 16:772-775.

Hsu, Wei-Lun, Yi-Hao Pai, Fan-Shuen Meng, Chee-Wee Liu, and Gong-Ru Lin. 2009. "Nanograin crystalline transformation enhanced UV transparency of annealing refined indium tin oxide film." *Applied Physics Letters* 94 (23):231906.

Hu, Binbin B, and Martin C Nuss. 1995. "Imaging with terahertz waves." *Optics letters* 20 (16):1716-1718.

Hu, Jianhua, and Roy G Gordon. 1992. "Atmospheric pressure chemical vapor deposition of gallium doped zinc oxide thin films from diethyl zinc, water, and triethyl gallium." *Journal of Applied Physics* 72 (11):5381-5392.

Hu, Yalan, Xungang Diao, Cong Wang, Weichang Hao, and Tianmin Wang. 2004. "Effects of heat treatment on properties of ITO films prepared by rf magnetron sputtering." *Vacuum* 75 (2):183-188.

Hunsche, Stefan, Daniel M Mittleman, Martin Koch, and Martin C Nuss. 1998. "New dimensions in T-ray imaging." *IEICE Transactions on Electronics* 81 (2):269-276.

Ishihara, Kunihiko, Keishi Ohashi, Tomofumi Ikari, Hiroaki Minamide, Hiroyuki Yokoyama, Jun-ichi Shikata, and Hiromasa Ito. 2006. "Terahertz-wave near-field imaging with subwavelength resolution using surface-wave-assisted bow-tie aperture." *Applied physics letters* 89 (20):201120.

Janowitz, Christoph, Valentina Scherer, Mansour Mohamed, Alica Krapf, Helmut Dwelk, Recardo Manzke, Zbigniew Galazka, Reinhard Uecker, Klaus Irmscher, and Roberto Fornari. 2011. "Experimental electronic structure of In2O3 and Ga2O3." *New Journal of Physics* 13 (8):085014.

JIANQIAO, HU. 2006. "Low temperature high performance indium tin oxide films and applications."

Jingsheng, Shi, Mary B Chan-Park, and Chang Ming Li. 2009. "Bottom gate organic thin-film transistors fabricated by ultraviolet transfer embossing with improved device performance." *Organic Electronics* 10 (3):396-401.

Johnson, Jon L, Timothy D Dorney, and Daniel M Mittleman. 2001. "Enhanced depth resolution in terahertz imaging using phase-shift interferometry." *Applied Physics Letters* 78 (6):835-837.

Kai-hong, Wang, and Li Jiu-sheng. 2019. "Muti-band terahertz modulator based on double metamaterial/perovskite hybrid structure." *Optics Communications* 447:1-5.

Karasawa, T, and Y Miyata. 1993. "Electrical and optical properties of indium tin oxide thin films deposited on unheated substrates by dc reactive sputtering." *Thin Solid Films* 223 (1):135-139.

Kawase, Kodo, Yuichi Ogawa, Yuuki Watanabe, and Hiroyuki Inoue. 2003. "Non-destructive terahertz imaging of illicit drugs using spectral fingerprints." *Optics express* 11 (20):2549-2554.

Kerkache, L, A Layadi, E Dogheche, and Denis Remiens. 2005. "Physical properties of RF sputtered ITO thin films and annealing effect." *Journal of Physics D: Applied Physics* 39 (1):184.

Kim, Dong-Ho, Mi-Rang Park, Hak-Jun Lee, and Gun-Hwan Lee. 2006. "Thickness dependence of electrical properties of ITO film deposited on a plastic substrate by RF magnetron sputtering." *Applied Surface Science* 253 (2):409-411.

Kim, Han-Ki, Jin-A Jeong, Kwang-Hyuk Choi, Soon-Wook Jeong, and Jae-Wook Kang. 2009. "Characteristics of flexible ito electrodes grown by continuous facing target roll-to-roll sputtering for flexible organic solar cells." *Electrochemical Solid State Letters* 12 (5):H169.

Kim, Ji-Seon, M Granström, Richard H Friend, N Johansson, WR Salaneck, Rusli Daik, W James Feast, and Franco Cacialli. 1998. "Indium–tin oxide treatments for single-and double-layer polymeric light-emitting diodes: The relation between the anode physical, chemical, and morphological properties and the device performance." *Journal of applied physics* 84 (12):6859-6870.

Kitahara, Hideaki, Masahiko Tani, and Masanori Hangyo. 2010. "Three-dimensional tomographic imaging in terahertz region." *Japanese journal of applied physics* 49 (2R):020207.

Knickerbocker, SA, and AK Kulkarni. 1995. "Calculation of the figure of merit for indium tin oxide films based on basic theory." *Journal of Vacuum Science Technology A: Vacuum, Surfaces, Films* 13 (3):1048-1052.

Ko, Eun-Hye, Hyo-Joong Kim, Sang-Jin Lee, Jae-Heung Lee, and Han-Ki Kim. 2016. "Nano-sized Ag inserted into ITO films prepared by continuous roll-to-roll sputtering for high-performance, flexible, transparent film heaters." *RSC advances* 6 (52):46634-46642.

Koenig, Swen, Daniel Lopez-Diaz, Jochen Antes, Florian Boes, Ralf Henneberger, Arnulf Leuther, Axel Tessmann, René Schmogrow, David Hillerkuss, and Robert Palmer. 2013. "Wireless sub-THz communication system with high data rate." *Nature photonics* 7 (12):977-981.

Koseoglu, Hasan, Fulya Turkoglu, Metin Kurt, Mutlu D Yaman, Fatime G Akca, Gulnur Aygun, and Lutfi Ozyuzer. 2015. "Improvement of optical and electrical properties of ITO thin films by electro-annealing." *Vacuum* 120:8-13.

Köhler, Rüdeger, Alessandro Tredicucci, Fabio Beltram, Harvey E Beere, Edmund H Linfield, A Giles Davies, David A Ritchie, Rita C Iotti, and Fausto Rossi. 2002. "Terahertz semiconductor-heterostructure laser." *Nature* 417 (6885):156-159.

Kwok, Hoi Sing, XW Sun, and DH Kim. 1998. "Pulsed laser deposited crystalline ultrathin indium tin oxide films and their conduction mechanisms." *Thin Solid Films* 335 (1-2):299-302.

Lai, Wei-En, Yao-Hua Zhu, Huai-Wu Zhang, and Qi-Ye Wen. 2013. "A novel reflector of AZO thin films applicable for terahertz devices." *Optical Materials* 35 (6):1218-1221.

Lee, Alan WM, Benjamin S Williams, Sushil Kumar, Qing Hu, and John L Reno. 2006. "Real-time imaging using a 4.3-THz quantum cascade laser and a 320/spl times/240 microbolometer focal-plane array." *IEEE Photonics Technology Letters* 18 (13):1415-1417.

Lee, Byung Hak, Iee Gon Kim, Sung Woo Cho, and Si-Hyun Lee. 1997. "Effect of process parameters on the characteristics of indium tin oxide thin film for flat panel display application." *Thin Solid Films* 302 (1-2):25-30.

Lee, Dong-ho, Shang-hun Shim, Jin-sik Choi, and Keun-byoung Yoon. 2008. "The effect of electro-annealing on the electrical properties of ITO film on colorless polyimide substrate." *Applied surface science* 254 (15):4650-4654.

Lee, Ho-Chul, and O Ok Park. 2004. "Electron scattering mechanisms in indium-tin-oxide thin films: grain boundary and ionized impurity scattering." *Vacuum* 75 (3):275-282.

Lewen, F, E Michael, R Gendriesch, J Stutzki, and G Winnewisser. 1997. "Terahertz laser sideband spectroscopy with backward wave oscillators." *Journal of Molecular Spectroscopy* 183 (1):207-209.

Li, Jiusheng. 2010. "Terahertz wave narrow bandpass filter based on photonic crystal." *Optics Communications* 283 (13):2647-2650.

Löffler, Torsten, Thilo May, Christian am Weg, Ali Alcin, Bernd Hils, and Hartmut G Roskos. 2007. "Continuous-wave terahertz imaging with a hybrid system." *Applied Physics Letters* 90 (9):091111.

Major, S, and KL Chopra. 1988. "Indium-doped zinc oxide films as transparent electrodes for solar cells." *Solar Energy Materials Solar Cells* 17 (5):319-327.

Mann, Chris. 2006. "A compact real time passive terahertz imager." Passive Millimeter-Wave Imaging Technology IX.

Marezio, M. 1966. "Refinement of the crystal structure of In2O3 at two wavelengths." *Acta Crystallographica* 20 (6):723-728.

Mason, Thomas O, GB Gonzalez, J-H Hwang, and DR Kammler. 2003. "Point defects and related properties of highly co-doped bixbyite In 2 O 3." *Physical Chemistry Chemical Physics* 5 (11):2183-2189.

Meng, Li-jian, A Macarico, and R Martins. 1995. "Study of annealed indium tin oxide films prepared by rf reactive magnetron sputtering." *Vacuum* 46 (7):673-680.

Meng, Li-Jian, and Frank Placido. 2003. "Annealing effect on ITO thin films prepared by microwave-enhanced dc reactive magnetron sputtering for telecommunication applications." *Surface Coatings Technology* 166 (1):44-50.

Mitrofanov, Oleg, Mark Lee, Julia WP Hsu, Igal Brener, Roey Harel, John F Federici, James D Wynn, Loren N Pfeiffer, and Ken W West. 2001. "Collection-mode near-field imaging with 0.5-THz pulses." *IEEE Journal of Selected Topics in Quantum Electronics* 7 (4):600-607.

Mittleman, DM, S Hunsche, L Boivin, and MC Nuss. 1997. "T-ray tomography." *Optics Letters* 22 (12):904-906. doi: 10.1364/OL.22.000904.

Moeller, Lothar, John Federici, and Ke Su. 2011. "THz wireless communications: 2.5 Gb/s error-free transmission at 625 GHz using a narrow-bandwidth 1 mW THz source." 2011 XXXth URSI General Assembly and Scientific Symposium.

Moore, EJ. 1967. "Quantum-transport theories and multiple scattering in doped semiconductors. II. Mobility of n-type gallium arsenide." *Physical Review B* 160 (3):618.

Mott, Nevill Francis. 1974. "Metal-insulator transitions."

Mueller, Eric R, Joel Fontanella, and RW Henschke. 2000. "Stabilized, integrated, far-infrared laser system for NASA/Goddard Space Flight Center." Proc. 10th Int. Symp. Space Terahertz Technol.

Nahata, Ajay, James T Yardley, and Tony F Heinz. 1999. "Free-space electro-optic detection of continuous-wave terahertz radiation." *Applied physics letters* 75 (17):2524-2526.

Nebioğlu, Mehmet Ali, Taylan Takan, Hakan Altan, Yasemin Demirhan, Hakan Alaboz, Lütfi Özyüzer, and Cumali Sabah. 2017. "An indium tin oxide metasurface filter for terahertz applications: Design, fabrication, and characterization." *Modern Physics Letters B* 31 (08):1750074.

Nishio, Keishi, Tadanori Sei, and Toshio Tsuchiya. 1996. "Preparation and electrical properties of ITO thin films by dip-coating process." *Journal of materials science* 31 (7):1761-1766.

Noguchi, S, and H Sakata. 1981. "Intrinsic limit of electrical properties of transparent conductive oxide films." *J. Phys. D: Appl. Phys.* 114:1523.

Ohhata, Yutaka, Fujitoshi Shinoki, and Sadafumi Yoshida. 1979. "Optical properties of rf reactive sputtered tin-doped In2O3 films." *Thin Solid Films* 59 (2):255-261.

Ohring, Milton. 2001. *Materials science of thin films*: Elsevier.

Okada, Koichi, Shigemi Kohiki, Suning Luo, Daiichiro Sekiba, Satoshi Ishii, Masanori Mitome, Atsushi Kohno, Takayuki Tajiri, and Fumiya Shoji. 2011. "Correlation between resistivity and oxygen vacancy of hydrogen-doped indium tin oxide thin films." *Thin Solid Films* 519 (11):3557-3561.

Ortolani, Michele, Alessandra Di Gaspare, and Roberto Casini. 2011. "Progress in producing terahertz detector arrays." SPIE Newsroom.

Ozyuzer, Lutfi, Alexei E Koshelev, Cihan Kurter, Nachappa Gopalsami, Qiang Li, Masashi Tachiki, Kazuo Kadowaki, Takashi Yamamoto, Hidetoshi Minami, and Hiroshi Yamaguchi. 2007. "Emission of coherent THz radiation from superconductors." *Science* 318 (5854):1291-1293.

Park, Sung-Hyun, Sang-Jin Lee, Jae Heung Lee, Jinha Kal, Jungseok Hahn, and Han-Ki Kim. 2016. "Large area roll-to-roll sputtering of transparent ITO/Ag/ITO cathodes for flexible inverted organic solar cell modules." *Organic Electronics* 30:112-121.

Park, Sung-Hyun, Sang-Mok Lee, Eun-Hye Ko, Tae-Ho Kim, Yoon-Chae Nah, Sang-Jin Lee, Jae Heung Lee, and Han-Ki Kim. 2016. "Roll-to-Roll sputtered ITO/Cu/ITO multilayer electrode for flexible, transparent thin film heaters and electrochromic applications." *Scientific reports* 6:33868.

Pei, Yu, Limei Lin, Weifeng Zheng, Yan Qu, Zhigao Huang, and Fachun Lai. 2009. "Effect of passing electric current on the electrical and optical properties of ITO films in air." *Surface Review Letters* 16 (06):887-893.

Quaas, M, C Eggs, and H Wulff. 1998. "Structural studies of ITO thin films with the Rietveld method." *Thin Solid Films* 332 (1-2):277-281.

Ray, Swati, Ratnabali Banerjee, Nandita Basu, AK Batabyal, and Asok K Barua. 1983. "Properties of tin doped indium oxide thin films prepared by magnetron sputtering." *Journal of Applied Physics* 54 (6):3497-3501.

Richards, PL. 1994. "Bolometers for infrared and millimeter waves." *Journal of Applied Physics* 76 (1):1-24.

Rodriguez-Morales, Fernando, K Sigfrid Yngvesson, Richard Zannoni, Eyal Gerecht, Dazhen Gu, Xin Zhao, Niklas Wadefalk, and John J Nicholson. 2006. "Development of integrated HEB/MMIC receivers for near-range terahertz imaging." *IEEE transactions on microwave theory techniques* 54 (6):2301-2311.

Rogozin, A, N Shevchenko, M Vinnichenko, M Seidel, A Kolitsch, and W Möller. 2006. "Annealing of indium tin oxide films by electric current: Properties and structure evolution." *Applied physics letters* 89 (6):061908.

Roth, Alain P, James B Webb, and Digby F Williams. 1982. "Band-gap narrowing in heavily defect-doped ZnO." *Physical Review B* 25 (12):7836.

Salehi, A. 1998. "The effects of deposition rate and substrate temperature of ITO thin films on electrical and optical properties." *Thin solid films* 324 (1-2):214-218.

Sanon, Geeta, Raj Rup, and Abhai Mansingh. 1991. "Band-gap narrowing and band structure in degenerate tin oxide (SnO 2) films." *Physical Review B* 44 (11):5672.

Sharma, Aditi, and Ghanshyam Singh. 2009. "Rectangular microstirp patch antenna design at THz frequency for short distance wireless communication systems." *Journal of Infrared, Millimeter, Terahertz Waves* 30 (1):1.

Shen, Xilin, Charles R Dietlein, Erich Grossman, Zoya Popovic, and François G Meyer. 2008. "Detection and segmentation of concealed objects in terahertz images." *IEEE transactions on Image Processing* 17 (12):2465-2475.

Sheu, JK, Yan-Kuin Su, GC Chi, MJ Jou, and CM Chang. 1998. "Effects of thermal annealing on the indium tin oxide Schottky contacts of n-GaN." *Applied physics letters* 72 (25):3317-3319.

Shi, Zaiying, Lixin Song, and Tao Zhang. 2018. "Terahertz reflection and visible light transmission of ITO films affected by annealing temperature and applied in metamaterial absorber." *Vacuum* 149:12-18.

Shi, Zhong-Wei, Xing-Xing Cao, Qi-Ye Wen, Tian-Long Wen, Qing-Hui Yang, Zhi Chen, Wen-Sheng Shi, and Huai-Wu Zhang. 2018. "Terahertz modulators based on silicon nanotip array." *Advanced Optical Materials* 6 (2):1700620.

Shigesato, Yuzo, Satoru Takaki, and Takeshi Haranoh. 1992. "Electrical and structural properties of low resistivity tin-doped indium oxide films." *Journal of Applied Physics* 71 (7):3356-3364.

Sierros, KA, NJ Morris, SN Kukureka, and DR Cairns. 2009. "Dry and wet sliding wear of ITO-coated PET components used in flexible optoelectronic applications." *Wear* 267 (1-4):625-631.

Sofi, AH, MA Shah, and K Asokan. 2018. "Structural, optical and electrical properties of ITO thin films." *Journal of Electronic Materials* 47 (2):1344-1352.

Stadler, Andreas. 2012. "Transparent conducting oxides—an up-to-date overview." *Materials* 5 (4):661-683.

Steckelmacher, W. 1991. Handbook of plasma processing technology: Fundamentals, etching, deposition and surface interactions: Edited by SM Rossnagel, JJ Cuomo and WD Westwood, Noyes Publications, NJ, USA, 1990. Pergamon.

Stern, Frank, and Robert M Talley. 1955. "Impurity band in semiconductors with small effective mass." *Physical Review B* 100 (6):1638.

Suzuki, Akio, Tatsuhiko Matsushita, Takanori Aoki, Yoshitaka Yoneyama, and Masahiro Okuda. 2001. "Pulsed laser deposition of transparent conducting indium tin oxide films in magnetic field perpendicular to plume." *Japanese Journal of Applied Physics* 40 (4B):L401.

Tang, Ching W, and Steven A VanSlyke. 1987. "Organic electroluminescent diodes." *J Applied physics letters* 51 (12):913-915.

Terzini, E, P Thilakan, and C Minarini. 2000. "Properties of ITO thin films deposited by RF magnetron sputtering at elevated substrate temperature." *Materials Science Engineering: B* 77 (1):110-114.

Thampy, Anand Sreekantan, Sriram Kumar %J Physica E: Low-dimensional Systems Dhamodharan, and Nanostructures. 2015. "Performance analysis and comparison of ITO-and FTO-based optically transparent terahertz U-shaped patch antennas." 66:52-58.

Thilakan, P, C Minarini, S Loreti, and E Terzini. 2001. "Investigations on the crystallisation properties of RF magnetron sputtered indium tin oxide thin films." *Thin Solid Films* 388 (1-2):34-40.

Tuna, Ocal, Yusuf Selamet, Gulnur Aygun, and Lutfi Ozyuzer. 2010. "High quality ITO thin films grown by dc and RF sputtering without oxygen." *Journal of Physics D: Applied Physics* 43 (5):055402.

Van der Valk, NCJ, and PCM Planken. 2002. "Electro-optic detection of subwavelength terahertz spot sizes in the near field of a metal tip." *Applied Physics Letters* 81 (9):1558-1560.

Wang, S, and XC Zhang. 2004. "Pulsed terahertz tomography." *Journal of Physics D: Applied Physics* 37 (4):R1.

Wasa, Kiyotaka, and Shigeru Hayakawa. 1992. "Handbook of sputter deposition technology."

Yang, Jun, Haibing Cao, Hongyun Fang, Weien Lai, Guanghua Shi, Guangsheng Deng, Zhiping Yin, Fei Cai, and Ying Li. 2020. "Reflectance-tunable terahertz polarization reflector using indium tin oxide." *Optics Communications* 460:125149.

Yang, Jun, Shuang-chen Ruan, Min Zhang, and Wei Zhang. 2008. "Real-time continuous-wave imaging with a 1.63 THz OPTL and a pyroelectric camera." *Optoelectronics Letters* 4 (4):295.

Younus, Ayesha. 2011. "Imagerie Térahertz 2D et 3D: Application pour l'étude des matériaux du patrimoine culturel." Bordeaux 1.

Yu, Hsin Her, Shug-June Hwang, Ming-Chun Tseng, and Chien-Chang Tseng. 2006. "The effect of ITO films thickness on the properties of flexible organic light emitting diode." *Optics communication* 259 (1):187-193.

Zhang, Keran, Furong Zhu, CHA Huan, and ATS Wee. 1999. "Effect of hydrogen partial pressure on optoelectronic properties of indium tin oxide thin films deposited by radio frequency magnetron sputtering method." *Journal of applied physics* 86 (2):974-980.

Zhang, Keran, Furong Zhu, CHA Huan, and ATS Wee. 2000. "Indium tin oxide films prepared by radio frequency magnetron sputtering method at a low processing temperature." *Thin Solid Films* 376 (1-2):255-263.

Zhao, Yu Tong, Bian Wu, Bei Ju Huang, and Qiang Cheng. 2017. "Switchable broadband terahertz absorber/reflector enabled by hybrid graphene-gold metasurface." *Optics express* 25 (7):7161-7169.

Zhu, Bo, Yijun Feng, Junming Zhao, Ci Huang, Zhengbin Wang, and Tian Jiang. 2010. "Polarization modulation by tunable electromagnetic metamaterial reflector/absorber." *Optics express* 18 (22):23196-23203.

VİTA

Hasan Köseoğlu was born in İzmir, Turkey, on Semptember 7, 1982. After graduating from Beştepeler High School, he registered to the İzmir Institute of Technology and he completed a Bachelor of Science in Physics in June of 2006 with the award of 2nd highest GPA among the graduated students. In September 2006, He entered the graduate school at İzmir Institute of Technology. He received an M.Sc. degree in June 2010 in Physics and Ph.D. degree in June 2020 in Materials Science and Engineering from İzmir Institute of Technology. He worked as a research assistant between 2013 and 2017 at İzmir Institute of Technology, Materials Science and Engineering Department. He has also experience on Terahertz Waves and various deposition techniques such as evaporation and magnetron sputtering technique, and characterization techniques such as electrical and optical characterization.

Some Publications:

- Y. Demirhan, **H. Koseoglu**, F. Turkoglu, Z. Uyanik, M. Ozdemir, G. Aygun, L. Ozyuzer, "The Controllable Deposition of Large Area Roll-to-Roll Sputtered ITO Thin Films for Photovoltaic Applications", Renewable Energy **146**, 1549-1559 (2020).
- F. Turkoglu, **H. Koseoglu**, A. Cantas, F. G. Akca, E. Meric, D. G. Buldu, M. Ozdemir, E. Tarhan, L. Ozyuzer and G. Aygun, "Effect of Sulfurization Duration and Cu-Sn Layer Adjacency in Metallic Precursor of Cu_2ZnSnS_4 Absorber Layer on the Performance of Zn(O,S) Buffered Cells", Thin Solid Films **670**, 6-16 (2019).
- F. Turkoglu, **H. Koseoglu**, S. Zeybek, M. Ozdemir, G. Aygun, and L. Ozyuzer, "Effect of Substrate Rotation Speed and Off-Center Deposition on the Structural, Optical and Electrical Properties of AZO Thin Films Fabricated by DC Magnetron Sputtering", Journal of Applied Physics **123 (16)**, 165104 (2018).
- **Hasan Koseoglu**, Fulya Turkoglu, Mutlu D. Yaman, Metin Kurt, Fatime G. Akça, Gülnur Aygün, Lütfi Özyüzer, "Improvement of optical and electrical properties of ITO thin films by electro-annealing", *Vacuum* **120**, 8-13 (2015)
- F. Turkoglu, L. Ozyuzer, **H. Koseoglu**, Y. Demirhan, S. Preu, S. Malzer, Y. Simsek, H.B. Wang, P. Muller, "Emission of the THz waves from large area mesas of superconducting $Bi_2Sr_2CaCu_2O_{8+\delta}$ by the injection of spin polarized current", *Physica C: Superconductivity* **491**, 7-10 (2013)
- F. Turkoglu, **H. Koseoglu**, Y. Demirhan, L Ozyuzer, S Preu, S Malzer, Y Simsek, P Müller, T Yamamoto and K Kadowaki, "Interferometer measurements of terahertz waves from $Bi_2Sr_2CaCu_2O_{8+\delta}$ mesas", *Superconductor Science and Technology* **25**, 125004 (2012)
- **H. Koseoglu**, F. Turkoglu, Y. Simsek, L. Ozyuzer, "The Fabrication of THz Emitting Mesas by Reactive Ion-Beam Etching of Superconducting Bi2212 with Multilayer Masks", *Journal of Superconductivity and Novel Magnetism* **24**, 1083-1086 (2011)
- L. Ozyuzer, Y. Simsek, **H. Koseoglu**, F. Turkoglu, C Kurter, U Welp, AE Koshelev, KE Gray, WK Kwok, T Yamamoto, K Kadowaki, Y Koval, HB Wang and P Müller, "Terahertz wave emission from intrinsic Josephson junctions in high-Tc superconductors", *Superconductor Science and Technology* **22**, 114009 (2009).
- Y. Demirhan, F. Turkoglu, **H. Koseoglu**, H. Saglam, N. Miyakawa K. Kadowaki and L. Ozyuzer, "Inhomogeneity of Micron-Sized Triple Terahertz Emitters Fabricated from Intrinsic Josephson Junctions in Single Crystal $Bi_2Sr_2CaCu_2O_{8+\delta}$ ", Springer: NATO Science for Peace and Security Series B: Physics and Biophysics, Terahertz and Mid Infrared Radiation: Detection of Explosives and CBRN Edited by Mauro F. Pereira and Oleksiy Shulika Book Chapter, pp 95-102 (2014)